The present work was submitted to the Institute of solar research

Techno-economic comparison of different paths for solar generation of process heat at a temperature level of 130 °C

Master thesis

presented by

Oltmann, Tim

377322

Name of 1st examiner: Univ.-Prof. Dr.-Ing. Dipl.-Ing Robert Pitz-Paal

Name of 2nd examiner: Univ.-Prof. Dr.-Ing. Bernhard Hoffschmidt

Internal supervisor: Javier Inigo Labairu M. Sc.

Aachen, 21.03.2022

Abstract

One approach to solving the climate crisis is to transition to the clean production of energy. Renewable energies are already present in Germany in the electricity sector, but provide negligibly little heat in the industrial sector. Therefore, the focus of this thesis is the techno-economic evaluation of solar-powered heat generation systems on an industrial scale. More specifically, the evaluation of systems with 5 MW of process steam production at 130 °C.

Evaluated are four energy generating systems. The first system has a parabolic trough collector field to generate heat and a pressurized thermal energy storage, with water as the medium, to increase the capacity factor of the system.

The second system has a compound parabolic concentrator collector as a thermal collector to produce heat of up to 95 °C. Therefore, a compression heat pump is integrated to elevate the heat to a temperature level of 130 °C. The electricity is provided by the grid or a combination of the grid and a photovoltaic field. A thermal energy storage is integrated to store the excess heat of the collector field.

The third system has a photovoltaic field and an electric heater to convert the electricity into heat. As storage, a battery is integrated.

The fourth system also has a photovoltaic field with an electric heater. The difference is that a pressurized thermal energy storage is used.

The systems are simulated in Würzburg in Germany and Almeria in Spain to analyze the impact of the irradiation levels. The results are compared through economic and technical key figures.

In Würzburg, the photovoltaic system with thermal storage reaches the highest capacity factors with the lowest levelized cost of heat, because photovoltaic modules can use diffuse irradiation. In Almeria, the direct irradiation is higher, and the parabolic trough system achieves the lowest levelized cost of heat for a capacity factor of up to 89 %.

A brief economic comparison for both locations with the gas prices of the second half of 2022 and the beginning of 2023 shows that the systems can compete with fossil-fueled technologies up to certain capacity factors. However, it showed that the economic benefit strongly depends on the location and gas price.

Table of contents

List of figures

List of tables

List of symbols and abbreviations

Symbols	Unit	Designation
a_1	1/rad	IAM coefficient for PTC in greenius
a_2	$1/rad^2$	IAM coefficient for PTC in greenius
a_3	$1/rad^3$	IAM coefficient for PTC in greenius
A_c	m^2	Collector area
A_{PV}	m^2	PV module area
b_0	1/K	PTC efficiency coefficient in greenius
b_1	W/m^2K	PTC efficiency coefficient in greenius
b_2	W/m^2K^2	PTC efficiency coefficient in greenius
b_3	W/m^2K^3	PTC efficiency coefficient in greenius
b_4	W/m^2K^4	PTC efficiency coefficient in greenius
c_1	1/rad	IAM coefficient for PTC
c_2	$1/rad^2$	IAM coefficient for PTC
c_p	J/kgK	Specific heat capacity
$c_{p,solid}$	J/kgK	Solid specific heat capacity
$c_{p,liquid}$	J/kgK	Liquid specific heat capacity
d_1	W/m^2K	CPC heat loss coefficient
d_2	W/m^2K^2	CPC heat loss coefficient
e^+	-	Positron
e_1	-	PV efficiency coefficient
e_2	-	PV efficiency coefficient
e_3	-	PV efficiency coefficient
E	W/m^2	Irradiation intensity
E_0	W/m^2	Reference Irradiation intensity
E_{dir}	W/m^2	Diffuse irradiation intensity
E_{diff}	W/m^2	Direct irradiation intensity
f	m	Focal length
F'	-	Collector efficiency factor
F	-	Fill factor
Δh	J/kg	Evaporation enthalpy

h_{in}	J/kg	Specific enthalpy in
h_{out}	J/kg	Specific enthalpy out
H_{u}	J/kg	Lower heating value
He	-	Helium
I	-	Total current
I_{i}	-	Individual current
I_{mpp}	-	Nominal maximum power point current
I_{sc}	-	Short-circuit current
$\mathrm{m_0}$	1/K	PTC heat loss coefficient
$\mathrm{m_1}$	$\mathrm{W/m^2K}$	PTC heat loss coefficient
$\mathrm{m_2}$	$\mathrm{W/m^2}$	PTC heat loss coefficient
$\dot{m}_{\mathrm{fuel}}$	kg/s	Fuel mass flow
m_{storage}	kg	Mass storage material
$\dot{m}_{\mathrm{w}}$	kg/s	Water mass flow
n	-	Neutron
p	-	Hydrogen atom
P_{el}	-	Electric Power
P_{mpp}	-	Maximum Power
$\dot{Q}_{\mathrm{conv}}$	W	Convective heat flow
$\dot{Q}_{\mathrm{h}}$	W	Condenser heat flow
$\dot{Q}_{\mathrm{l}}$	W	Evaporator heat flow
$\dot{Q}_{\mathrm{l,PTC}}$	W	Heat flow losses from PTC
$\dot{Q}_{\mathrm{l,CPC}}$	W	Heat flow losses from CPC
$\dot{Q}_{\mathrm{out,PTC}}$	W	Usable heat flow from PTC
$\dot{Q}_{\mathrm{out,CPC}}$	W	Usable heat flow from CPC
$\dot{Q}_{\mathrm{out,EH}}$	W	Usable heat flow from CPC
$\dot{Q}_{\mathrm{rad}}$	W	Radiation heat flow
Q_{storage}	J	Storage energy
$Q_{\mathrm{s,tot}}$	J	Total used heat of solar heat generating system
r	%	discount rate
ΔT	K	Temperature difference between collector and environment

ΔT_{g}	K	Temperature difference between collector and environment in greenius
ΔT_{lift}	K	Temperature lift heat pump
t	s	Time
t_{end}	s	End time
T_{1}	K	Temperature state 1
T_{2}	K	Temperature state 2
T_{3}	K	Temperature state 3
T_{amb}	K	Ambient temperature
T_{c}	K	Collector temperature
T_{dr}	K	Correction temperature coefficient
T_{h}	K	High temperature heat pump
T_{l}	K	Low temperature heat pump
$T_{SF,in}$	K	Solar field inlet temperature
$T_{SF,out}$	K	Solar field outlet temperature
u_{1}	-	Semi empirical COP coefficient
u_{2}	-	Semi empirical COP coefficient
u_{3}	-	Semi empirical COP coefficient
u_{4}	-	Empirical COP coefficient
u_{5}	-	Empirical COP coefficient
u_{6}	-	Empirical COP coefficient
u_{7}	-	Empirical COP coefficient
u_{8}	-	Empirical COP coefficient
u_{9}	-	Empirical COP coefficient
u_{10}	-	Empirical COP coefficient
u_{11}	-	Empirical COP coefficient
U	-	Total voltage
U_{i}	-	Individual voltage
U_{mpp}	-	Nominal maximum power point voltage
U_{oc}	-	Open-circuit voltage
$W_{s,tot}$	J	Total used electricity of a solar heat generating system
x	m	Abscissa

y	m	Ordinate

Greek symbols

α_E	°	Elevated surface Azimuth angle
α_{OC}	% / °C	PV heat loss coefficient open-circuit
α_P	% / °C	PV heat loss coefficient, power
α_{SC}	% / °C	PV heat loss coefficient, short-circuit
α_S	°	Sun azimuth angle
γ_S	°	Sun elevation angle
γ_E	°	Elevated surface elevation angle
δ_M	-	Material cost factor, heat exchanger
δ_P	-	Pressure cost factor, heat exchanger
δ_T	-	Temperature cost factor, heat exchanger
ζ	-	Intercept factor
η_{2nd}	-	Second law efficiency
$\eta_{0,PTC}$	-	Nominal optical efficiency for PTC
$\eta_{0i, CPC}$	-	Ideal optical efficiency for CPC
η_{boiler}	-	Boiler efficiency
η_{clean}	-	Cleanliness efficiency
$\eta_{con,CPC}$	-	Conversion factor CPC
η_{EH}	-	Efficiency of electric heater
$\eta_{opt,PTC}$	-	Optical efficiency for parabolic trough collector
η_{PTC}	-	Parabolic trough collector efficiency
$\eta_{PTC,g}$	-	Parabolic trough collector efficiency in greenius
η_{PV}	-	PV cell efficiency
η_{se}	-	Efficiency for semi empirical equation
κ_{diff}	-	Diffuse Incidence angle modifier
κ_{dir}	-	Direct incidence angle modifier
$\kappa_{dir,l}$	-	Longitudinal direct incidence angle modifier
$\kappa_{dir,t}$	-	Transversal direct incidence angle modifier
κ_{PTC}	-	Incidence angle modifier PTC

$\kappa_{PTC,g}$	-	Incidence angle modifier PTC in greenius
λ	m	Wave length
ϑ	°	Incidence angle
ϑ_{l}	°	Longitudinal incidence angle for CPC
ϑ_{PTC}	°	Incidence angle for PTC
ϑ_{t}	°	Transversal incidence angle for CPC
μ	-	Absorptance
ν	-	Neutrino
ρ	-	Reflectance
τ	-	Transmittance
Φ	-	Gamma quant
γ_{E}	°	Elevated surface Elevation angle

<u>Abbreviations</u>

AC	Alternating current
BESS	Battery energy storage system
COP	Coefficient of performance
CCOP	Carnot coefficient of performance
CPC	Compound parabolic concentrator
CSP	Concentrating solar power
EH	Electric heater
DC	Direct current
DNI	Direct normal irradiance
GHI	Global horizontal irradiance
IAM	Incidence angle modifier
LCOE	Levelized cost of electricity
LCOH	Levelized cost of heat
PTC	Parabolic trough collector
PTES	Pressurized thermal energy storage system

PV	Photovoltaic
TES	Thermal energy storage system
PTC_PTES	Heat generating system with a parabolic trough collector and pressurized thermal energy storage
CPC_HP_TES	Heat generating system with a compound parabolic concentrator collector, a heat pump and thermal energy storage
CPC_HP_TES_PV	Heat generating system with a compound parabolic concentrator collector, a heat pump, a thermal energy storage and a PV field
PV_EH_BESS	Heat generating system with a photovoltaic field, an electric heater and battery energy storage system
PV_EH_BESS	Heat generating system with a photovoltaic field, an electric heater and pressurized thermal energy storage

1 Introduction

In this chapter, the motivation and task of this thesis are explained.

1.1 Motivation

With the current climate change affecting the ecosystems of our planet, it is our duty and responsibility to avert or reduce the resulting negative impacts. Some of those negative effects are caused by CO_2 emissions. For example, rising CO_2 levels in the atmosphere impact the climate and can lead to extreme weather conditions like heat waves, which often contribute to wildfires. Furthermore, the CO_2 levels in the atmosphere impact air quality, which impacts our health and, among other things, causes lung diseases.
There are several approaches to reducing the current CO_2 emissions, for example, reducing air travel, stopping deforestation, planting more trees or increasing the efficiency of existing processes. Besides the latter, one main approach is switching to clean energy production and reducing the energy supplied by fossil-fueled technologies. (MasterClass 2021)

Renewable technologies can generate heat and electricity. In Germany, generating electricity with renewable energies, such as photovoltaic fields or wind turbines, is already established (Appunn 2022).

However, in the German heat sector, especially the industrial sector, the supplied heat is dominantly provided by fossil fuels. The German industry has an annual heat demand of 512 TWh, of which 87 TWh is needed at a temperature level of 100-200 °C. At that temperature level, close to no heat is supplied from solar thermal technologies or other renewable technologies. (cf. Mathiesen 2015, pp. 4–7)

On an industrial scale and at this temperature level, heat can be provided by a solar thermal collector field, for example (cf. Stieglitz and Heinzel 2012, pp. 85–86). Photovoltaic fields can be used in combination with an electric heater. (cf. Krüger 2021, p. 8)

A company leading by example is Heineken. Heineken is currently building two solar thermal collector plants to generate heat for their breweries and reduce fossil fuel consumption. In Spain, the company plans to achieve net-zero emissions by 2025. (List solar 2022)

In the past, solar thermal power plants had a cost disadvantage compared to fossil-fueled competing technologies. In recent years, however, concentrating solar power plants and photovoltaic systems have undergone a significant cost reduction. In combination with the current political situation in Europe, in connection with natural gas and climate change, this relation could positively shift towards renewable technologies. (cf. Iñigo-Labairu et al. 2022, 1–2; Kraemer 2022)

Due to the last reasons, there is an interest in researching the current technical and economic performance of renewable heat generating systems.

1.2 Task

Firstly, a literature search for relevant industries has to be made. Based on the latter literature search, a reference case for an industry with heat demand has to be defined. Subsequently, generator systems have to be chosen. In order to increase the capacity factor, a storage has to be integrated. For each collector technology, the optimal storage has to be researched.
Literature and market research have to be done to define techno-economic data for the reference case and the relevant technologies. Additionally, for the heat pump, thermodynamic principles and models have to be researched.
Prior to the simulations, target values have to be defined. The generator systems then have to be modeled and simulated in greenius and excel tables. Afterward, a sensitivity analysis of the results, regarding the model and costs is carried out. The results have to be critically evaluated and compared to existing literature.

2 Theory

In this chapter, the German industrial heat demand is shown first. Subsequently, suitable industries for this thesis with process heat demand under 200 °C are presented. Then the basic theory of solar radiation is explained to give a brief understanding of the energy which fuels solar collectors. Afterward, the theoretical background and the modeling for the relevant technologies in this thesis are presented. Finally, the calculation of the levelized cost of heat is explained, which will be an important economic key figure in this thesis.

2.1 Industrial heat demand

The final energy demand for Germany is 2467 TWh, of which 1384 TWh are needed for heating and cooling, as shown in Figure 2-1. The industrial sector accounts for 512 TWh of heating and cooling demand, of which 87 TWh are needed for process heating at 100-200 °C.

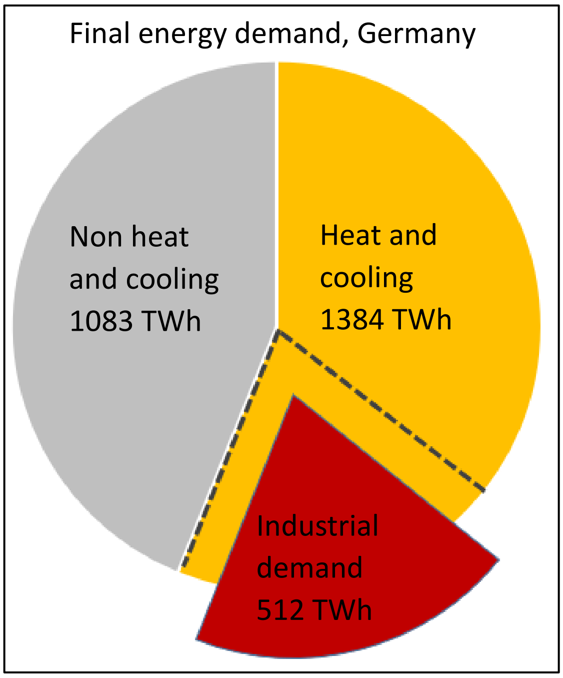

Figure 2-1: Final energy demand Germany (cf. Mathiesen 2015, p. 4)

Heat at 100-200 °C is mostly used by the paper, pulp, and printing industry with 25 TWh, the food, beverages, and tobacco industry with 10 TWh, the machinery and transport with 10 TWh and the chemical industry with 10 TWh. Figure 2-2 shows the heat demand of the latter industries, divided by temperature level.

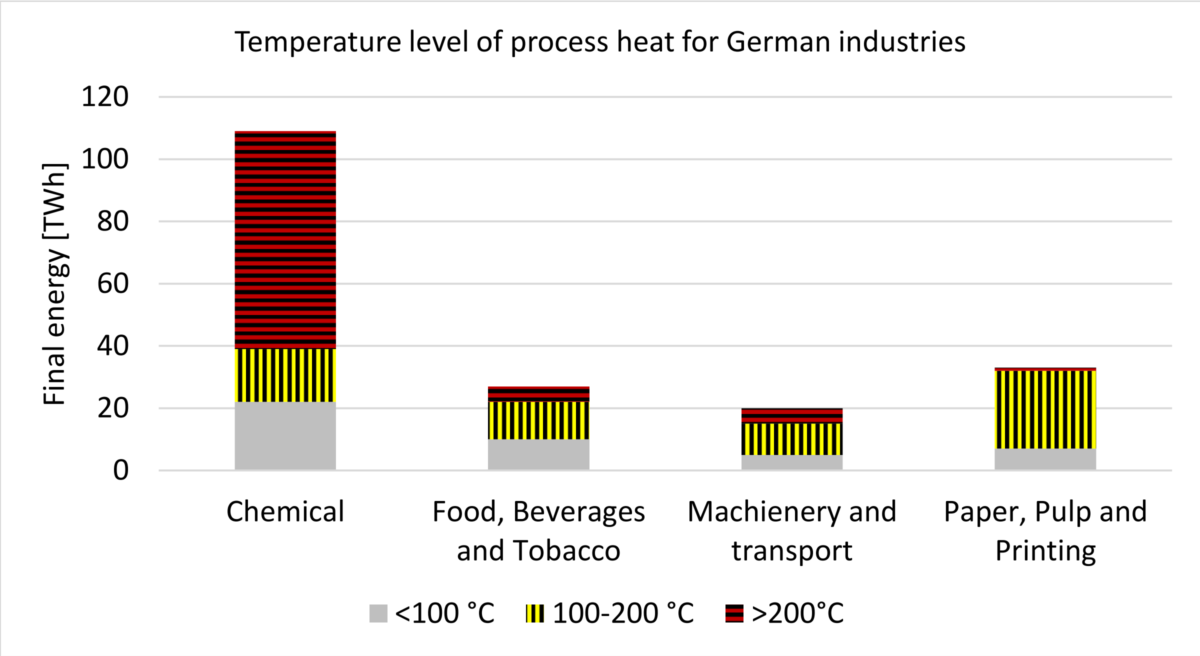

Figure 2-2: Process heat for German industries, divided by temperature level (cf. Mathiesen 2015, p. 6)

The heat is mostly supplied by fossil fuels, such as gas, with a 42 % share and coal, with a 19 % share. The rest is supplied by district heating, electricity, biomass, oil, and other fossil fuels. Currently, in Germany, heat supplied by solar technology is negligible compared to other technologies. (cf. Mathiesen 2015, pp. 4–6)

With the current energy transition taking place, this thesis researches the current potential of low temperature process heat supplied by solar technologies, mainly considering the food, beverages, and tobacco and the paper, pulp and printing industry.

For example, in the paper industry, solar technologies can be integrated in drying (95-160 °C), cooking (105-160 °C) and bleaching (40-160 °C) (cf. Arpagaus 2017, p. 13).

In the food industry, dairy has the largest energy usage (cf. Schmitt et al. 2015, p. 13). One advantage is the constant production over the week of dairy industries, which would lead to a higher utilization of solar energy (cf. Kalogirou 2003, p. 342).
Heat in the relevant temperature spectrum is needed for pasteurization (85-150 °C), the sterilization of packed dairy products (110-120 °C) and the flash pasteurization (130 °C) for the production of ESL-milk. For example, the flash pasteurization is usually built with multiple heat exchangers, in which an additional heat exchanger with a solar cycle can be integrated. The

lowest process heat is needed for tempering and homogenization at a maximum temperature of 70 °C. (cf. Schmitt et al. 2015, pp. 21–23)

The second-largest industry of the food branch, regarding energy usage, is the sugar industry. Although this industry has a large energy usage, the economic potential for solar applications is negligible. This is due to the usage of cogeneration technologies and short production times throughout the year. Other industries that are unfit for solar applications are starch and the oil industry. Those are uninteresting because of complex facilities, missing integration points and already existing heat recovery. (cf. Schmitt et al. 2015, p. 13)

The meat industry has the third-largest energy consumption. Much of it is used for heat of up to 100 °C, such as brewing, cooking, smoking, and cleaning. High temperature applications are backing, frying, grilling, sterilization and singeing. Solar technologies can be used to supply hot water for low temperature applications, or steam for the sterilization. (cf. Schmitt et al. 2015, pp. 23–26)

Industries with lower energy consumption are the fruit and the confectionery industry. The fruit industry needs heat of up to 140 °C for example, for sterilization. A disadvantage is the seasonal dependency of the processing. One interesting example in the confectionery industry is the roasting of cacao beans, which requires Steam up to 130 °C. (cf. Schmitt et al. 2015, pp. 26–34)

A specific example of the beverage industry is the construction of a concentrated solar power (CSP) plant in Seville, Spain. The Energy solutions provider Engie Espana builds a 30 MW CSP plant for a beer factory from Heineken. The 20-million-euro project will produce thermal energy for the beer factory, reducing the fossil gas consumption by over 60 %. The complete solar field occupies 80000 m^2, equivalent to eight soccer fields. In addition, a six-hour storage is integrated, to allow production at times without solar radiation. The plant is used to produce superheated water for the brewing process. The annual generated heat is 28700 MWh. The construction will be finalized in June 2023. (Djunisic 2022)

To achieve net-zero emissions, Heineken is building a second CSP plant at the same brewery. The second CSP plant will occupy 6000 square meters and supplies 200 °C water. The plant has an annual heat output of 3504 MWh, which is used for developing and product packaging processes. (List solar 2022)

2.2 Solar radiation

The Sun, located in the center of our solar system, is the energy source of our planet. It is estimated to be 5 billion years old, and the temperature reaches 5776 K at the surface and up to $1.6*10^7$ K in the core. The mass is currently made up of 92 % hydrogen and 8 % helium.

The sun generates energy through a multistep fusion reaction of hydrogen. The hydrogen in the core of the sun is in a plasma state. Through enormous pressure and gravitational force, a fusion reaction from hydrogen to helium takes place. Beginning with the time-determining proton collision process, two hydrogen atoms p collide and react to a deuteron, made of a proton p and one neutron n. Thereby, a positron e^+ and an electron neutrino v are released. The positron reacts with an electron into pure energy. The deuteron reacts with another proton to a helium isotope ^3He, while releasing a gamma quant Φ. Finally, two of the ^3He react to a helium atom and two protons, which are again able to initiate a fusion reaction. Figure 2-3 shows the fusion reaction taking place in the sun. The released energy of the overall fusion reaction is 26.204 MeV = 4.198 10^{-12} J. (cf. Stieglitz and Heinzel 2012, pp. 24–26)

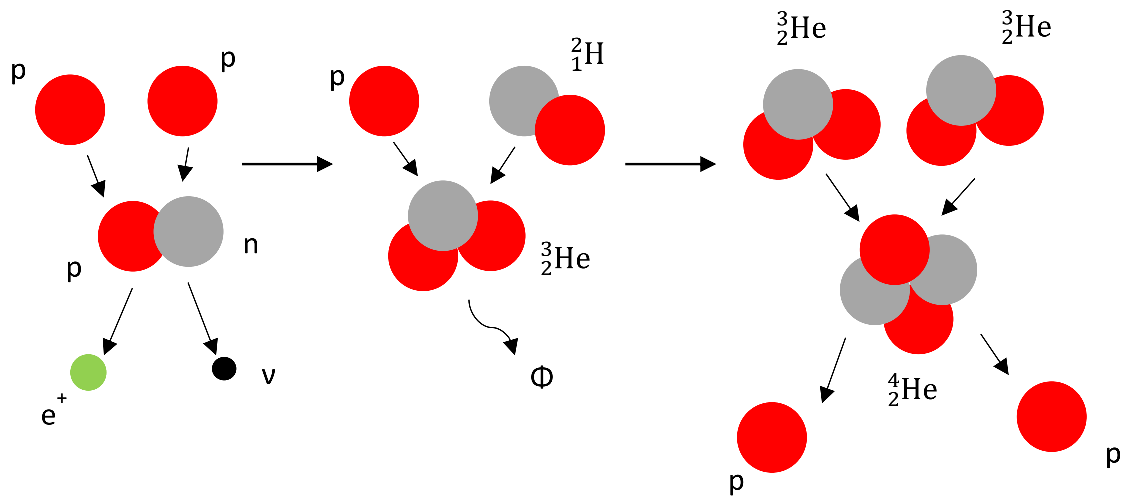

Figure 2-3: Hydrogen fusion reaction (cf. Stieglitz and Heinzel 2012, p. 26)

The generated energy of the sun reaches the earth as electromagnetic waves at a mean distance of $1.496*10^{11}$ m. The intensity of the extraterrestrial solar radiation reaching the Earth is at about 1367 W/m^2, varying through the year due to the elliptic orbit of the earth.
It consists of a spectrum of different wavelengths. The Energy among the wavelengths is distributed with shares of (cf. Stieglitz and Heinzel 2012, pp. 27–29):

- 6.4 % for ultraviolet radiation $\lambda < 380$ nm,

- 48 % for visible radiation 380 nm < λ < 3780 nm and
- 45.6% for infrared λ > 780 nm.

The electromagnetic radiation of the sun can be assumed as parallel waves due to the long distance to earth. Reaching the surface, the radiation weakens due to scattering and absorption because of molecules and ions of the earth's atmosphere. The magnitude of attenuation of the radiation depends on the distance traveled through the atmosphere. Radiation directly from the sun without being absorbed or scattered is called direct radiation. (cf. Pavlovic 2020, pp. 11–14)

When solar radiation reaches molecules and particles, it excites them. When the exited matter falls back into its normal state, it emits its own individual radiation. The emitted radiation is transmitted unequally in all directions. This radiation is called diffuse radiation, which contains more short-wave radiation.

This effect is the explanation for the color of the sky. The short-wave radiation is stronger scattered. Thus, at a high sun elevation, the sky appears blue. At a low sun incidence angle, the light has to travel a further distance through the sky, which reduces the intensity of the incoming blue light. Therefore, the intensity of the red light dominates, thus letting the sky appear in a red tone. (cf. Pavlovic 2020, pp. 14–17)

Radiation can be reflected if it hits on surfaces. The kind of reflection depends on the surface. Mirror-like reflection takes place when the surface roughness is smaller than the wavelength. It is called scattered reflection when the wavelength is the same size as the surface roughness. The albedo coefficient describes the reflection from zero to one, with one describing complete reflection and zero describing no reflection. (cf. Pavlovic 2020, pp. 17–19)

Due to the described intensity-reducing effect of the earth's atmosphere, the position of the sun needs to be known for the calculation of solar applications.

In Figure 2-4 the needed angles are shown. The current position of the sun at a specific place on earth can be defined by the sun azimuth angle α_S and sun elevation angle γ_S. DIN 5034 defines the sun elevation angle as the angle between the center of the sun and the horizon. The sun azimuth angle is defined as the angle between the north direction and the horizontal line of irradiance.

Another important angle is the incidence angle ϑ. It is the angle between the direction of irradiance and the normal vector of a surface. The surface is described by the angle α_E, the angle between the north and the surface and γ_E angle between the horizontal surface and the absorber surface.

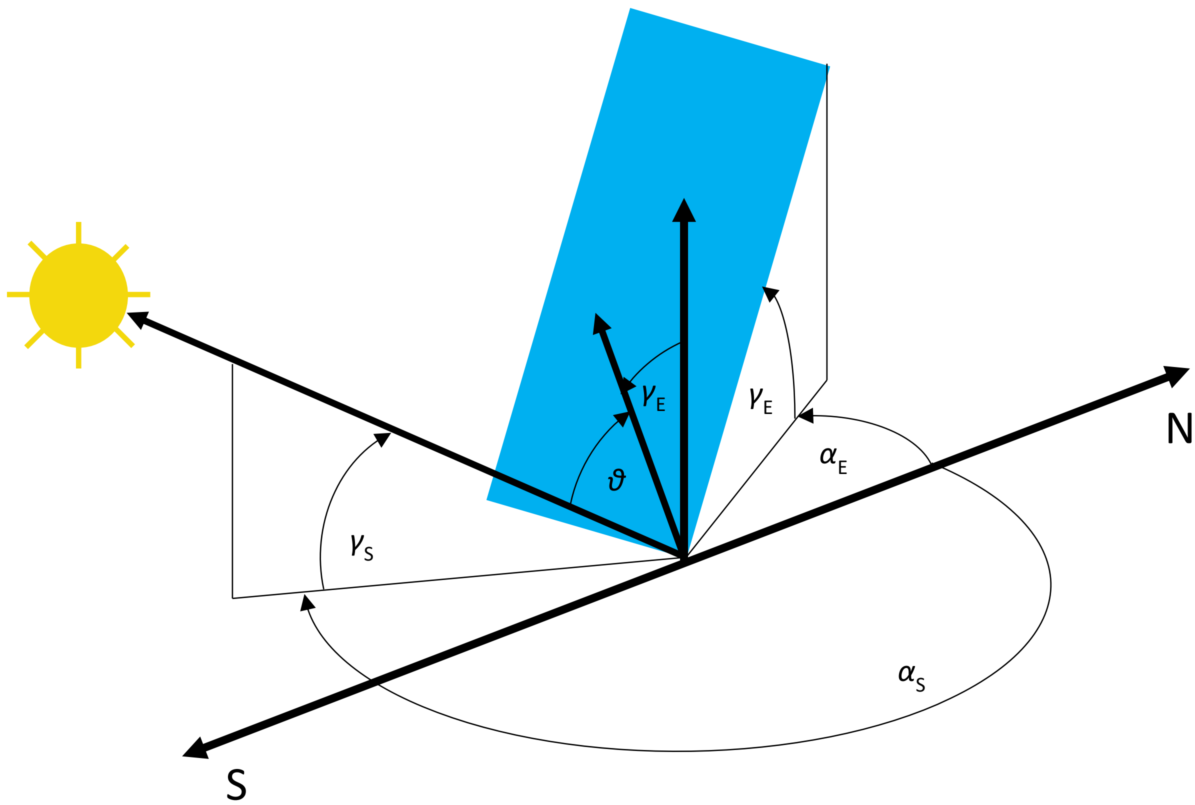

Figure 2-4: Calculation of the incidence angle (cf. Quaschning 2015, p. 75)

The incidence angle on a flat surface can be calculated with (cf. Quaschning 2015, pp. 75–76):

$$\vartheta = \arccos(-\cos\gamma_S \sin\gamma_E \cos(\alpha_S - \alpha_E) + \sin\gamma_s \cos\gamma_E). \qquad (2.1)$$

2.3 Solar thermal technologies

Solar thermal collectors convert the radiation of the sun into process heat, usable for industrial processes or heating applications. The technologies can be divided into concentrating and non-concentrating systems. The difference is that concentrating systems concentrate the solar radiation using lenses or mirrors. The simplest non-concentrating design is a tube mat absorber. Fluid flows through the tubes, which absorb the radiation. The fluid heats up and circulates because of density differences. This design can reach temperatures of 30-70 °C. (cf. Stieglitz and Heinzel 2012, pp. 85–89)

Flat collectors reach the highest temperatures as a non-concentrating technology. The absorber tube is covered by a glass vitrine, which prevents the surrounding air from circulating and reduces the heat losses. To further reduce the heat losses, the collector is isolated on the back. These collectors can be used for applications from 30-120 °C. (cf. Stieglitz and Heinzel 2012, pp. 85–89)

Concentrating systems reach higher temperatures. For example, in a solar tower application, process heat with high temperatures of up to 1400 °C can be achieved. Many mirrors, called heliostats, are installed around a solar tower. The heliostats reflect the solar radiation onto the absorber located at the top of the tower. (cf. Stieglitz and Heinzel 2012, pp. 85–89)

One concentrating collector for lower temperatures from 120 °C up to 400 °C, relevant for this thesis, is the parabolic trough collector (PTC). These collectors use a parabolic shaped mirror to concentrate the radiation onto an absorber tube.
(cf. Stieglitz and Heinzel 2012, pp. 85–89)

Figure 2-5 shows the concept of a parabolic trough collector. The design of the mirror focuses the irradiance on a focal point. The focal length is f.

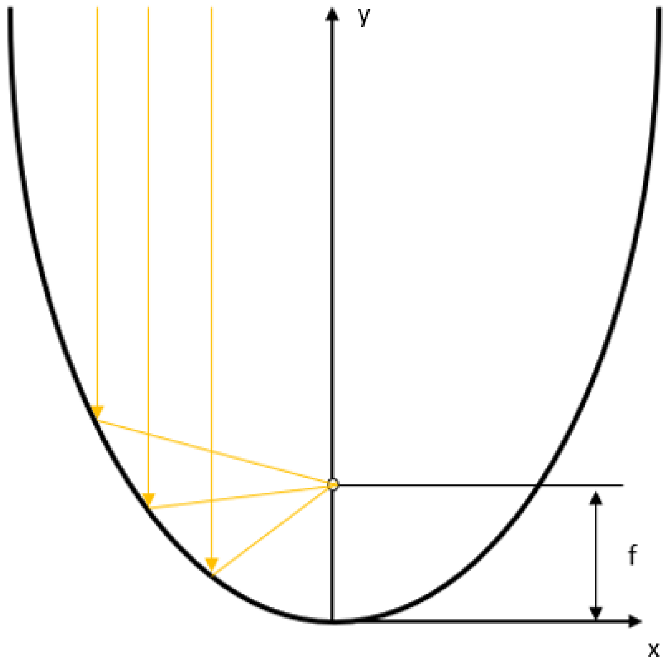

Figure 2-5: Parabolic trough collector shape (cf. Stieglitz and Heinzel 2012, p. 101)

The parabolic concentrator has a shape, which can be described by the following equation (cf. Stieglitz and Heinzel 2012, p. 101):

$y=\frac{1}{4f}x^2.$	(2.2)

Figure 2-6 shows the energy balance at the absorber tube. The direct radiation E_{dir} is reflected and concentrated by the parabolic collector. The absorber tube is covered by a glass tube to minimize heat losses.

The PTC collector can be tracked from north to south and east to west. For economic reasons, mostly only one tracking system is used. Most often, the collectors are installed from north to south and track the sun from east to west. (cf. Stieglitz and Heinzel 2012, p. 88)

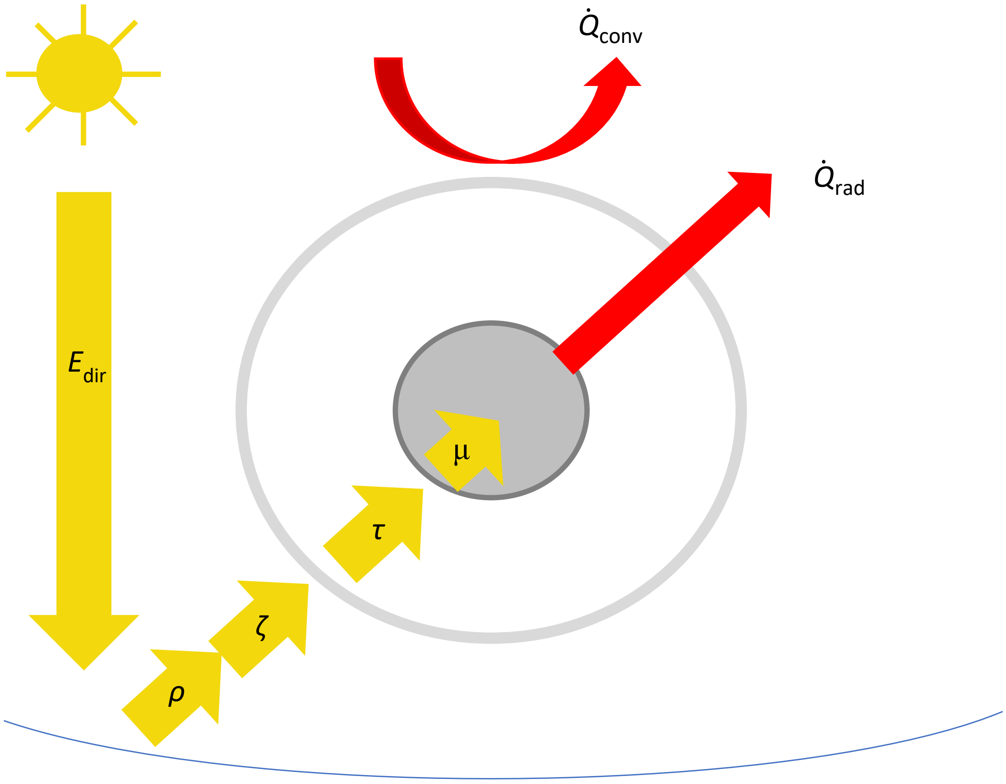

Figure 2-6: Energy balance for a parabolic trough collector (cf. Stieglitz and Heinzel 2012, p. 103)

The reflectance ρ of a clean parabolic trough mirror goes from zero to one, with one meaning a 100 % reflection. The Intercept factor ζ is the ratio of the reflected irradiance of the collector to the total reflected radiation reaching the absorber tube. The transmittance τ of the absorber glass cover describes the transmission radiation through the cover. Lastly, the absorptance μ of the absorber tube describes how much radiation is absorbed.

Due to the building temperature and the temperature difference to the environment, there are thermal losses to be considered. The most relevant heat losses are the radiation losses $\dot{Q}_{rad}$ and the convection losses at the cover $\dot{Q}_{conv}$. (cf. Stieglitz and Heinzel 2012, pp. 103–104).

The heat output that can be used is calculated with an energy balance. The incoming direct irradiance on the collector Area A_c is multiplied with an optical efficiency, and finally, the thermal losses $\dot{Q}_{l,PTC}$ are subtracted (cf. Quaschning 2015, p. 153):

$$\dot{Q}_{out,PTC}=E_{dir}A_c\eta_{opt,PTC}-\dot{Q}_{l,PTC}. \tag{2.3}$$

The optical efficiency for parabolic trough collectors $\eta_{opt,PTC}$ is the product of the optical factors shown in Figure 2-6, which result in the nominal optical efficiency $\eta_{0,PTC}$, an incidence angle modifier (IAM) κ_{PTC} and a cleanliness efficiency η_{clean}:

$\eta_{\mathrm{opt,\ PTC}} = \tau\mu\zeta\rho\kappa_{\mathrm{PTC}}\eta_{\mathrm{clean}} = \eta_{0,\mathrm{PTC}}\kappa_{\mathrm{PTC}}\eta_{\mathrm{clean}}.$	(2.4)

Most of the time, the nominal optical efficiency $\eta_{0,\mathrm{PTC}}$ is experimentally estimated.

The thermal losses sum up the radiation, convection and, if relevant, conduction thermal losses. In reality, the thermal losses are hard to calculate theoretically. Therefore, an empirical equation is mostly used. This is more accurate. The empirical function has three m_0, m_1, m_2 coefficients and is dependent on the temperature difference ΔT between the collector and the environment (cf.Quaschning 2015, pp. 153–156):

$\dot{Q}_{\mathrm{l,PTC}} = (m_0\kappa_{PTC}E_{\mathrm{dir}}+m_1+m_2\Delta T)A_{\mathrm{c}}\Delta T.$	(2.5)

The already mentioned incident angle modifier κ includes additional losses when the incidence angle is greater than 0°. It is calculated with the empirical coefficients c_1 and c_2:

$\kappa_{PTC}=\max(1-c_1\frac{\vartheta}{\cos\vartheta}-c_2\frac{\vartheta^2}{\cos\vartheta};\ 0).$	(2.6)

The incidence angle for a parabolic trough collector differs from a plane field due to the shape. With a north-south installation and no inclination, the equation is:

$\vartheta_{PTC}= \arccos(\sqrt{1-\cos^2\gamma_{\mathrm{s}}\cos^2\alpha_{\mathrm{s}}}).$	(2.7)

With the energy balance the overall efficiency can calculated as (cf. Quaschning 2015, 153–154):

$\eta_{\mathrm{PTC}} = \frac{\dot{Q}_{\mathrm{out,PTC}}}{E_{\mathrm{dir}}A_{\mathrm{c}}} = \eta_{\mathrm{opt,PTC}}-\frac{\dot{Q}_{\mathrm{l,PTC}}}{E_{\mathrm{dir}}A_{\mathrm{c}}}.$	(2.8)

The software greenius, described in chapter 3.1.1, calculates the efficiency and the output with the same approach as equation (2.8). However, the empirical equations for the thermal losses and the IAM differ from the quoted literature. It relies on the temperature difference as well but has four empirical coefficients b_0-b_4 and relies on the direct normal irradiance DNI:

$\eta_{\mathrm{PTC,g}} = \kappa_{\mathrm{PTC,g}}\cos(\vartheta)\eta_{0,\mathrm{PTC}}\eta_{\mathrm{clean}}-(\kappa_{\mathrm{PTC,g}}\cos(\vartheta)b_0\Delta T_{\mathrm{g}}+\frac{b_1\Delta T_{\mathrm{g}}+b_2\Delta T_{\mathrm{g}}^2+b_3\Delta T_{\mathrm{g}}^3+b_4\Delta T_{\mathrm{g}}^4}{DNI}).$	(2.9)

The IAM is calculated with an empirical equation:

$$\kappa_{PTC,g}=1-\frac{a_1\vartheta+a_2\vartheta^2+a_3\vartheta^3}{\cos\vartheta}.$$	(2.10)

The temperature difference ΔT_g is calculated with the mean temperature of the inlet $T_{SF,in}$ and oulet $T_{SF,out}$ temperature of the solar field and the ambient temperature T_{amb}:

$$\Delta T_g=\frac{T_{SF,in}+T_{SF,out}}{2}-T_{amb}.$$	(2.11)

The second relevant thermal collector for this thesis is the compound parabolic concentrator (CPC) collector.

Figure 2-7 shows the principle of a CPC collector with a tube absorber. On both sides above the absorber tube, the mirror has a parabolic shape. The focal point of each parabola lies on the end of the other parabola. Beneath the focal points, the mirror is shaped like an involute. Through the concentration onto the focal point, the solar radiation is deflected onto the absorber. (cf. Stieglitz and Heinzel 2012, pp. 112–114)

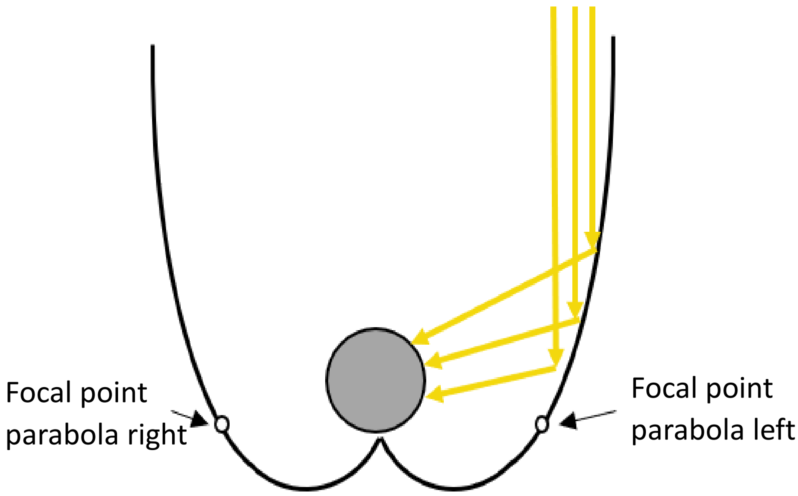

Figure 2-7: Compound parabolic concentrator with tube absorber
(cf. Stieglitz and Heinzel 2012, p. 113)

The generated heat $\dot{Q}_{use,CPC}$ of a CPC collector is the result of the product of irradiation E, collector area A_c and the conversion factor $\eta_{con,CPC}$ subtracted by the thermal losses $\dot{Q}_{l,CPC}$:

$\dot{Q}_{use,\mathrm{CPC}}=\eta_{\mathrm{con,CPC}}EA_{\mathrm{c}}-\dot{Q}_{\mathrm{l,CPC}}.$	(2.12)

In reality, the losses of this collector are calculated with an empirical equation. $\dot{Q}_{l,\,CPC}$ can be calculated with the mean collector temperature T_c, ambient temperature T_{amb}, the collector Area and coefficients d_1 and d_2 (cf. Quaschning 2015, pp. 121–125):

$\dot{Q}_{\mathrm{l,CPC}}= d_1A_{\mathrm{c}}(T_{\mathrm{c}}-T_{\mathrm{amb}})+d_2A_{\mathrm{c}}(T_{\mathrm{c}}-T_{\mathrm{amb}})^2.$	(2.13)

The conversion factor resembles the nominal optical efficiency of a CPC collector.
It is influenced by the incidence angle and the collector efficiency factor F'. For a CPC collector, the incidence angle modifier is distinguished for the direct radiation E_{dir} and diffuse radiation E_{diff}. With the ideal optical efficiency $\eta_{0i,\,CPC}$ the calculation is:

$\eta_{\mathrm{con,\,CPC}}=\eta_{\mathrm{0i,CPC}}\dfrac{F'\kappa_{\mathrm{dir}}E_{\mathrm{dir}}+F'\kappa_{\mathrm{diff}}E_{\mathrm{diff}}}{E_{\mathrm{dir}}+E_{\mathrm{diff}}}.$	(2.14)

The diffuse incidence angle modifier κ_{diff} is a given value.
The direct incidence angle modifier for tube absorbers is further divided into a longitudinal and a transversal share. Each is calculated as:

κ_{dir}=1-$\frac{1\text{-}\kappa_{\mathrm{dir}}(50°)}{0.5557}\left(\frac{1}{\cos\vartheta}\text{-}1\right)$.	(2.15)

$\kappa_{dir}(50°)$ is given value. The longitudinal incidence angle ϑ_{l} is calculated as

$\vartheta_{\mathrm{l}}=\lvert\gamma_{\mathrm{E}}+\arctan(\tan(90°\text{-}\gamma_{\mathrm{S}})\cos(\alpha_{\mathrm{S}}\text{-}\alpha_{\mathrm{E}}))\rvert$,	(2.16)

and the transversal incidence angle ϑ_{t} as

$\vartheta_{\mathrm{t}}=\lvert\frac{\arctan(\cos\gamma_{\mathrm{S}}\sin(\alpha_{\mathrm{S}}\text{-}\alpha_{\mathrm{E}})}{\cos\vartheta}\rvert$.	(2.17)

The direct angle modifier is the product of the longitudinal $\kappa_{\mathrm{dir,\,l}}$ and transversal $\kappa_{\mathrm{dir,\,t}}$share.

$\kappa_{\mathrm{dir}}=\kappa_{\mathrm{dir,l}}\kappa_{\mathrm{dir,t}}$	(2.18)

Finally, the collector efficiency results in (cf. Quaschning 2015, pp. 124–126):

$\eta_{\mathrm{CPC}}=\eta_{\mathrm{con,CPC}}\text{-}\frac{\dot{Q}_{\mathrm{l,\,CPC}}}{EA_{\mathrm{c}}}=\frac{\dot{Q}_{\mathrm{use,CPC}}}{EA_{\mathrm{c}}}$.	(2.19)

In 2020 71 solar heat plants, with a capacity of 91 MW_{th}, were commissioned. In 2019 86 solar heat plants were commissioned, and 86 plants in 2018.

The biggest parabolic trough plant commissioned in 2020 is in Ganzhou Tibet, China, with a capacity of 3.9 MW and with a solar field size of 5500 m^2. It is used for agricultural preheating. The second-largest parabolic trough plant was commissioned in Izmir, Turkey, with a capacity of 3 MW and with a solar field size of 5000 m^2. The process heat is used for a packaging company.

The largest vacuum type collector field commissioned in 2020 is in Sanya Hainan, China, with a capacity of 4.6 MW and a solar field size of 6645 m^2. (cf. Krüger et al. 2021a, pp. 1–2)

2.4 Photovoltaic module

Photovoltaic (PV) cells convert solar radiation energy into electrical energy. They use the inner photo effect. According to the band model, semiconductors have a band gap between the conduction band and the valence band. The gap is small enough so that the energy from the radiation of the sun can lift the valence electrons into the conduction band. For semiconductors, this energy gap is below 5 eV. For example, for silicon, it is 1.107 eV. (cf. Quaschning 2015, pp. 181–183)

Photovoltaic cells are made of semiconductors (for example silicon), with foreign atoms in the crystalline structure. For example, using silicon, a n-layer injected with phosphorus, and a p-layer injected with boron, are paired together. Phosphorus has five valence electrons, therefore one spare valence electron. Boron has three valence electrons, therefore a hole. At the junction, free electrons from the n-layer roam to the p-layer to fill the holes. Directly at the junction, most electrons from the n-layer have filled holes at the p-layer forming the depletion zone. A positive charge at the n-layer is created and a negative charge is created at the p-layer, thus an electric field is formed. (cf. Quaschning 2015, pp. 183–190)

Figure 2-8 shows a photovoltaic cell with solar radiation. Solar energy penetrates into the depletion layer and separates holes and electrons. Through the electric field, a current is created (photo effect). (cf. Quaschning 2015, pp. 183–190)

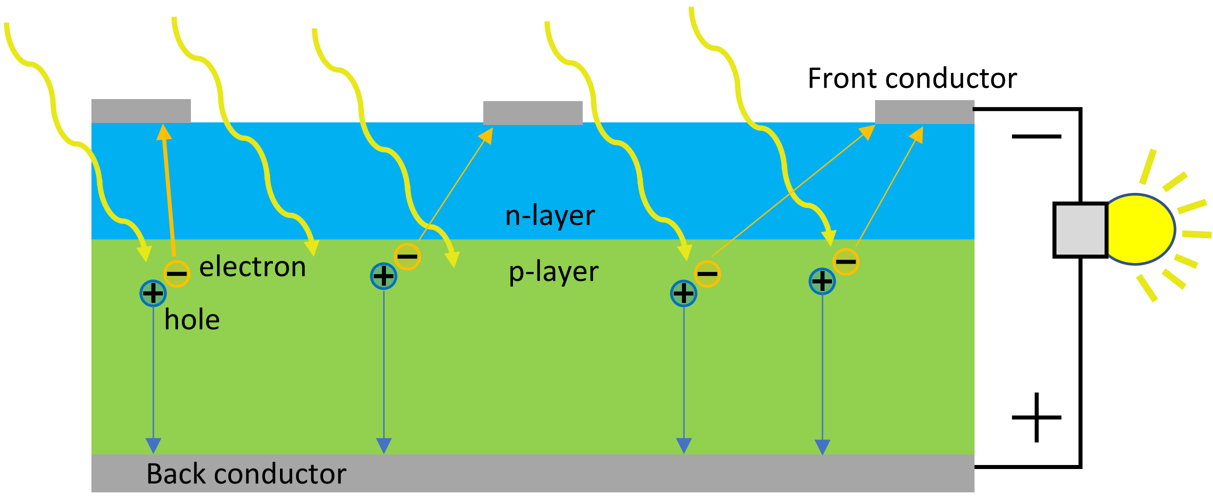

Figure 2-8: Principle of a photovoltaic cell (cf. Quaschning 2015, p. 188)

In an electrical circuit, PV cells generate a direct current. The general variables of PV cells are shown in Figure 2-9 and are: nominal maximum power point current I_{mpp}, nominal maximum power point voltage U_{mpp}, maximum power P_{mpp}, short-circuit current I_{sc}, open-circuit voltage U_{oc}, fill factor F and efficiency η_{PV}. (cf. Pavlovic 2020, pp. 47–48)

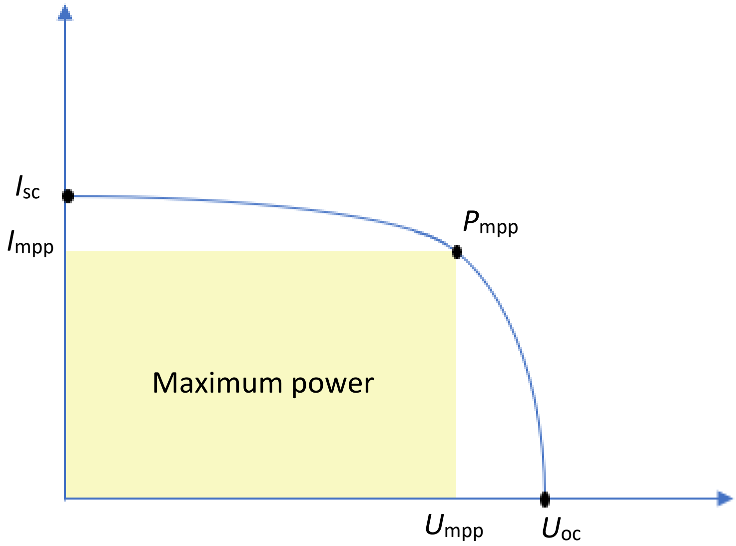

Figure 2-9: Power characteristics of a PV cell (cf. Pavlovic 2020, p. 48)

The relation between the variables is explained by equations (2.20),

$$P_{mpp}=U_{mpp}I_{mpp}=FU_{oc}I_{sc}, \tag{2.20}$$

And (2.21):

$$\eta_{PV}=\frac{FU_{oc}I_{sc}}{EA_{PV}}. \tag{2.21}$$

E is the intensity of the solar radiation, and A_{PV} is the surface of the solar cell. (cf. Pavlovic 2020, pp. 47–49)

In greenius the partial efficiency is calculated with an empirical equation:

$$\eta_{PV}=e_1+e_2 \ln\left(\frac{E}{E_0}\right)+e_3\left(\frac{E}{E_0}-1\right). \tag{2.22}$$

To increase the power of a solar field, solar modules can be connected in parallel or serial circuit. For the serial connection applies:

$$U=\sum_{i}^{n} U_{\mathrm{i}}\ , I=I_{\mathrm{i}}, \tag{2.23}$$

And for parallel connection (cf. Pavlovic 2020, pp. 82–83):

$$I=\sum_{i}^{n} I_i \ ,U=U_\mathrm{i}.$$	(2.24)

In real applications, the power depends on the temperature. With rising temperature, the band gap of the semiconductor shrinks. The current increases. However, the voltage decreases stronger. Therefore, the power decreases.

The change of short circuit current I_{sc}, open-circuit voltage U_{oc}, and power is often simplified and assumed as linear with coefficients. The usual value range of the coefficients for monocrystalline silicon is α_{SC} = 0.02-0.08 % / °C, α_{OC} = -0.21-0.48 % / °C and α_P = -0.32-0.51 % / °C. (cf. Quaschning 2015, pp. 208–211)

Photovoltaic modules generate direct current (DC). In the electricity grid, mostly alternating current (AC) current is used. Thus, an inverter is necessary. (cf. Quaschning 2015, p. 239)

An Inverter converts DC voltage into AC voltage. The simplest concept of a one phase inverter has four switches, for example, the H-wiring. The H-wiring is shown in Figure 2-10.

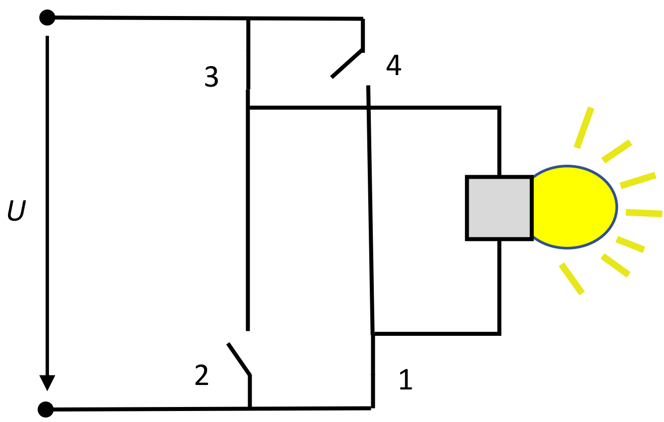

Figure 2-10: Inverter, H-wiring (cf. Quaschning 2015, p. 243)

The switches, one to four, are opened and closed pair wise so that the consumer sees an alternating voltage. This results in a rectangular signal. To generate a 3-phase ac current, a six-pulse bridge circuit wiring is used. Through controlled switching, a sinus-like signal can be achieved. Modern inverters reach efficiencies of up to 98 %. (cf. Quaschning 2015, pp. 239–250)

2.5 Heat pump

A heat pump is a machine that elevates heat from a low temperature to a high temperature (cf. Wolf 2017, p. 7). Currently, the market available heat pumps with a closed cycle are compression, adsorption, and absorption heat pumps. The compression heat pump is the only one available in the MW range (cf. Wolf 2017, p. 49).

The Most common for a compression heat pump is the cold vapor process (cf. Dohmann 2016, 61). The cold vapor process is shown in Figure 2-11.

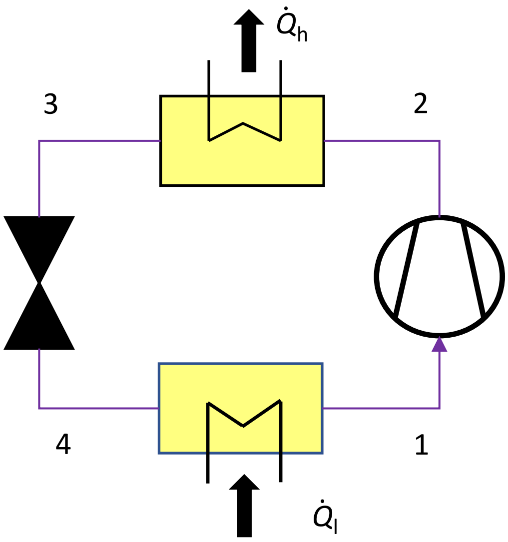

Figure 2-11: Compression heat pump (cf. Dohmann 2016, pp. 61–62)

In state one, the refrigerant is a slightly superheated vapor and the system presents its lowest pressure. From state one to two, the refrigerant is compressed. Through the compression, the temperature is increased from T_l to T_h. The heated high-pressure refrigerant then enters the condenser. In the condenser, the refrigerant desuperheats, condensates and subcools. Meanwhile, the heat flow Q_l is transferred to the heat sink. After the condenser, in state three, the refrigerant is liquid. The refrigerant is then throttled. After the throttle, in state four, the refrigerant is in the wet steam area. From state four to one, the liquid share of the refrigerant is vaporized in the evaporator. The heat Q_l supplied to the evaporator comes from an external heat source. (cf. Dohmann 2016, 61–62)

For an ideal system, the thermodynamic cycle can be described by four thermodynamic change of states (cf. Dohmann 2016, 62):

- 1 - 2 Isentropic compression,

- 2 - 3 Isobar heat dissipation,
- 3 - 4 Isenthalpic throttling,
- 4 - 1 Isobar heat supply.

The coefficient of performance (*COP*) is the efficiency of the heat pump. It is calculated as the ratio of generated heat flow $\dot{Q}_h$ to the electric power of the compressor P_{el}. With the isentropic thermodynamic change of states, the carnot (*CCOP*) follows as (cf. Wolf 2017, pp. 8–10):

$CCOP = \frac{\dot{Q}_h}{P} = \frac{\dot{Q}_h}{\dot{Q}_h - \dot{Q}_l} = \frac{T_h}{T_h - T_l}..$	(2.25)

To calculate the real *COP*, there are theoretical, semi-empirical, and empirical approaches. For the theoretical approach, the second law efficiency η_{2nd} is introduced. It relates the carnot *COP* with the real *COP*:

$COP = \eta_{2nd} COP_{carnot}.$	(2.26)

The value for η_{2nd} can be found in literature, with typical values around 0.45. The COP_{carnot} is calculated through the temperature levels, as described by equation (2.25). (cf. Jesper et al. 2021, p. 16)

The semi empirical approach considers more losses. The theoretical equation is extended as described by equation (2.27):

$COP = \eta_{se} \frac{T_h + T_{dr}}{\Delta T_{lift} + 2T_{dr}}.$	(2.27)

Due to the needed temperature pinch in the condenser and evaporator, the temperature lift for the refrigerant is higher than the temperature lift ΔT_{lift} from heat sink to heat source. Therefore, T_{dr} is introduced to compensate for this inaccuracy. To compensate temperature independent losses η_{se} is introduced.

The semi-empirical equation can be improved through different weighing of ΔT_{lift} & T_h (cf. Jesper et al. 2021, pp. 17–19):

$COP = u_1 (\Delta T_{lift} + 2T_{dr})^{u_2} (T_h + T_{dr})^{u_3}$	(2.28)

In the semi-empirical approach, the coefficients u_1, u_2, u_3 have physical boundaries.

In contrast, in the empirical approach, the coefficients have no physical boundaries, and no physical interpretation is possible. Jesper et al. list three different empirical equations (cf. Jesper et al. 2021, pp. 20–21):

$$COP = u_4\,(\Delta T_{\mathrm{lift}}+2T_{\mathrm{dr}})^{u_5}(T_{\mathrm{h}}+T_{\mathrm{dr}})^{u_6}, \qquad (2.29)$$

$$COP = u_7\,\exp(u_8 \Delta T_{\mathrm{lift}}), \qquad (2.30)$$

and

$$COP = u_9\,\Delta T_{\mathrm{lift}}^{2} + u_{10}\,\Delta T_{\mathrm{lift}} + u_{11}. \qquad (2.31)$$

For different temperatures, different approaches achieve better results. For example, the semi empirical approach achieves the highest accuracy for heat pumps with heat sink temperatures of up to 160 °C. (cf. Jesper et al. 2021, p. 24)

The coefficients for the efficiency equations are dependent on the refrigerant. Example refrigerant types are hydrocarbons HC, hydrofluorooelfins HFO and hydrochlorofluorooelfins HCFO.

The refrigerants differ, among other characteristics, in critical temperature T_c, critical pressure p_c, normal boiling point NBP, molar mass M, ecological factor and handling. For a refrigerant to be suitable for a heat pump, it has to fulfill several constraints. Asparagus et al. describe a list of conditions, for example (cf. Arpagaus et al. 2018, p. 19):

- Critical temperature has to be sufficiently higher than T_h,
- Low critical pressure,
- Environmental compatibility and
- Safety.

Current heat pumps available on the market reach temperatures up to 165 °C with a temperature lift of 130 K. The Kobe Steel Kobelco SGH 120/165 can generate steam at 165 °C from a heat source of 35-70 °C. A COP, depending on the source temperature, of 1.6-2.5 is reached.

The Viking HeatBooster S4 can lift heat from 60-100 °C to 110-150 °C. A temperature lift from 90-140 °C achieves a *COP* of four, and a temperature lift from 70-120 °C achieves a COP of 3.6. (cf. Arpagaus et al. 2018, p. 11)

Figure 2-12 shows the laboratory construction and 3D model of a high temperature heat pump. The heat pump consists of the standard component and has an additional internal heat exchanger (IHX). The sufficient degrees in superheating differ between the refrigerants. With an IHX the needed degrees of superheating can be reached. Additionally, an auxiliary heater is installed to ensure the superheating. A lubricant separator is integrated after the compressor. The Condenser and IHX are designed as plate heat exchangers. The compressor is a reciprocating piston compressor. The heat pump can generate 12 kW of heat, can use heat source temperatures of up to 110 °C and can generate heat of up to 150 °C. (cf. Arpagaus 2017, pp. 67–68)

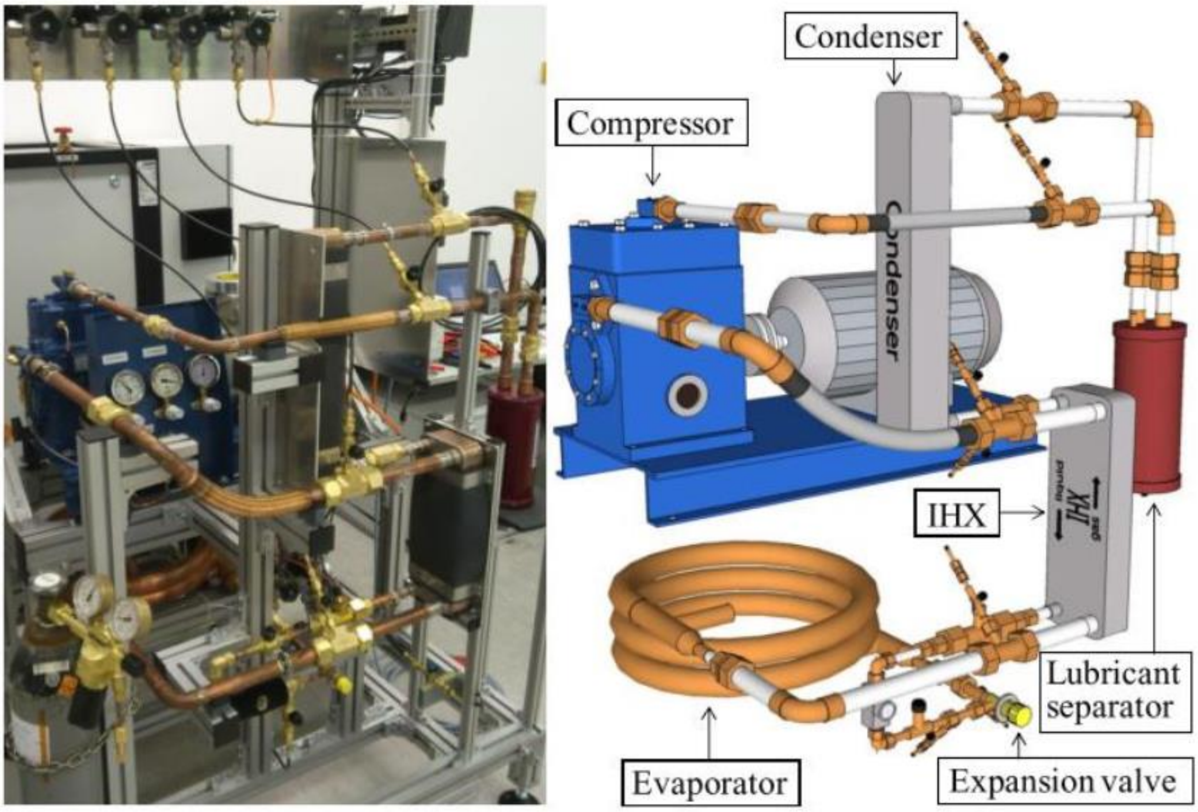

Figure 2-12: Picture, 3D-model and scheme of high temperature heat pump (cf. Arpagaus 2017, pp. 67–68)

2.6 Boiler and electrical heater

The Boiler is a vessel in which feed water is vaporized and can be superheated. Heat can be supplied by combustion, electricity or nuclear energy.

In a fire tube boiler, the water is contained in a shell. Pipes run through the shell, in which hot fluid flows. The heat is transferred to the water in the shell. Consequently, the water vaporizes and rises above the water level and leaves through an outlet at the top.

In a water tube boiler, water flows through tubes from the bottom to the top. The hot fluid flows around the tubes, thus vaporizing the water in the tubes.
The efficiency of a boiler η_{boiler}, with hot fluid created through combustion, is calculated with the ratio of the enthalpy difference between the inlet h_{in} and outlet h_{out} of the water mass flow $\dot{m}_{\text{w}}$ and the mass flow $\dot{m}_{\text{fuel}}$ of the fuel multiplied by the lower heating value H_{u} (cf. Washim Akram and Hasanuzzaman 2022, pp. 9–13):

$$\eta_{\text{boiler}}=\frac{\dot{m}_{\text{w}}(h_{\text{out}}-h_{\text{in}})}{\dot{m}_{\text{fuel}}H_{\text{u}}} \tag{2.32}$$

Electric heaters (EH) are devices that use electricity for the production of hot water or steam, for example, for industrial processes.

The heat can be generated in an element through ohmic resistance.
The efficiency η_{EH} is calculated as the ratio of the generated heat $\dot{Q}_{\text{out,EH}}$ to the used electric power P_{el} (cf. Danish Energy Agency 2016, pp. 314–321):

$$\eta_{EH}=\frac{\dot{Q}_{\text{out,EH}}}{P_{\text{el}}}. \tag{2.33}$$

Modern electric heaters reach efficiencies of up to 98 %. The power can be varied between 0-100 %. Typical start up times are between 1-5 min.

Since 2012 two 40 MW electric boilers have been installed at a combined heat and power plant in Aarhus. Another electric heater was installed at Asnæsværket in Kalundborg with a total capacity of 93 MW. Furthermore, a 30 MW electric boiler was installed at a combined heat and power plan of Silkeborg Forsyning. (cf. Danish Energy Agency 2016, pp. 314–321)

2.7 Thermal energy storage

With regenerative technologies, a vast amount of energy for many applications can be produced. Most technologies rely on the fluctuating weather. The problem is the synchronization between the energy generation and the demand. One solution for heating applications is a thermal energy storage system (TES). In times of oversupply of energy, the heat is stored and can be utilized at a needed time. To do that, the nominal power of the solar plan must be greater than the energy demand. (cf. Washim Akram and Hasanuzzaman 2022, pp. 215–216)

Two main types of TES are sensible and latent thermal energy storages.
A sensible storage stores energy through a temperature difference between a low and high temperature. (cf. Stieglitz and Heinzel 2012, pp. 595–597)
Figure 2-13 shows the relation between the stored heat and the temperature difference.

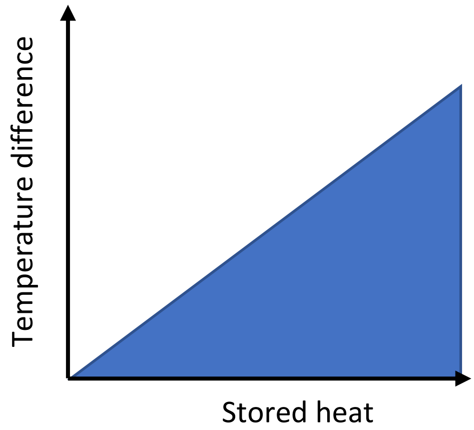

Figure 2-13: Sensible heat storage (cf. Washim Akram and Hasanuzzaman 2022, p. 217)

The stored energy can be calculated with the mass of the storage medium $m_{storage}$, the specific heat capacity c_p, and the temperature difference T_1-T_2 (cf. Stieglitz and Heinzel 2012, pp. 601–602):

$$Q_{storage}=\int_{t_1}^{t_2} m_{storage} c_p dt = mc_p(T_2-T_1). \tag{2.34}$$

The medium can be gaseous, liquid, or solid. Liquid storage systems can be subdivided into two tank and one tank thermocline systems, and further into indirect and direct systems.

Two tank systems have a hot and a cold tank separating the medium. The hot medium is used and pumped into the cold tank, and vice versa.
A one tank system has only one tank, with the cold and hot fluid in the same tank. The tank has temperature layers between the cold and hot fluid, increasing from bottom to top. When loading the storage, the fluid from the bottom is removed, heated and fed back in at the top. When using the stored energy, the hot medium has to be taken from the top, used and then

is fed back in at the bottom. As a variant, the storage can be filled with a cheap filler material with a higher heat capacity than the fluid. The one tank system is usually cheaper than the two-tank system. (cf. Stieglitz and Heinzel 2012, pp. 596–609)

Direct systems are loaded directly with the fluid from, for example, the solar field. Indirect systems have a heat exchanger separating the storage material and the fluid of the systems. (cf. Stieglitz and Heinzel 2012, pp. 596–609)
Figure 2-14 shows an indirect two tank system and a direct one tank system.

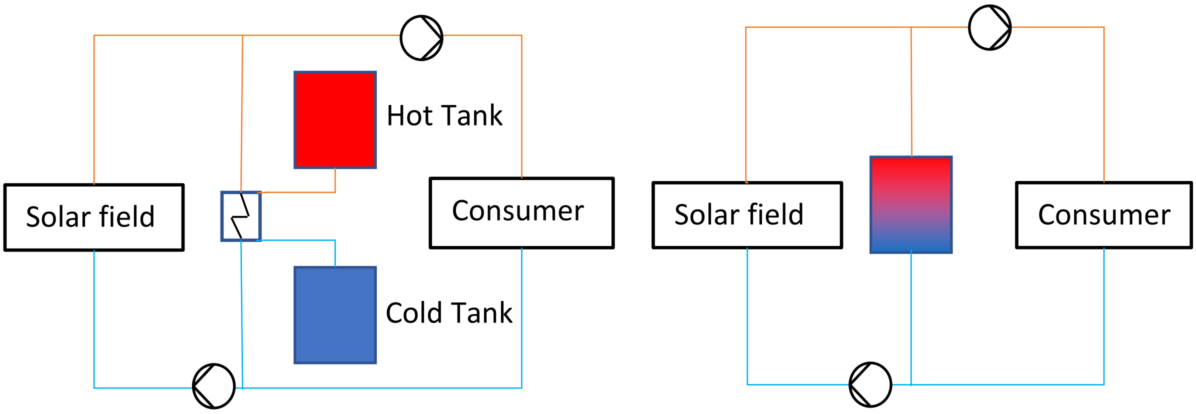

Figure 2-14: Indirect two tank system (left), direct one tank system (right) (cf. Stieglitz and Heinzel 2012, p. 605)

Exemplary liquid storage mediums are water, oil, salts, and natrium.
Water is the cheapest medium with 10^{-4} \$/kg and has the highest heating capacity. However, it is not suitable for very high temperatures because of its low normal boiling point. Above certain pressures, pressurized thermal energy storages (PTES) can become uncompetitively expensive. Oils can reach temperatures of up to 400 °C, but disintegrate irreversible at too high temperatures. They cost about 0.3-5 \$/kg. For higher temperatures, salts can be used. Carbonate salts can be operated up to 850 °C. The cost range is 0.5-2.4 \$/kg. One negative characteristic is the high boiling point of salts. To prevent freezing, auxiliary heaters have to be installed within the tank and piping system. (cf. Stieglitz and Heinzel 2012, pp. 596–609)

A latent heat storage stores the most heat through melting or fusion enthalpy, depending on the change of state. Figure 2-15 shows the temperature over stored heat.

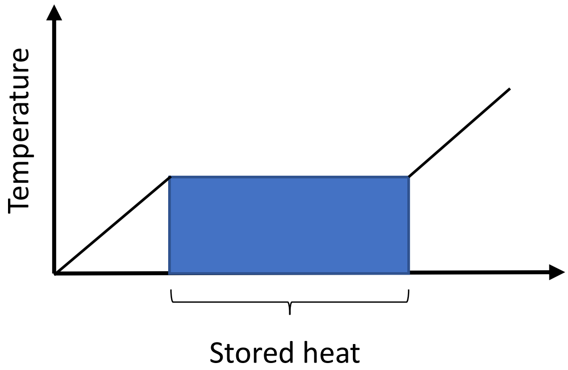

Figure 2-15: Stored energy, latent storage
(cf. Washim Akram and Hasanuzzaman 2022, p. 218)

The stored energy can be calculated with the evaporation enthalpy Δh and sensible heat of the mass (cf. Washim Akram and Hasanuzzaman 2022, pp. 217–218):

$Q = m_{\mathrm{storage}}(c_{\mathrm{p,solid}}(T_2 - T_1) + \Delta h + c_{\mathrm{p,liquid}}(T_3 - T_2))$.	(2.35)

Compared to a sensible storage, a latent storage has a higher storage density, lower temperature gradients and reduced losses. Downsides are corrosive effects and or supercooling. (cf. Washim Akram and Hasanuzzaman 2022, p. 218)
For low temperature applications, a sensible storage has lower investment costs (cf. Stieglitz and Heinzel 2012, p. 610).

A sensible storage with water as storage material, a temperature up to 150 °C, and a specific energy storage density between 60-100 kWh/m^3 costs between 0.4-10 €/kWh (Energy storage 2023).
For temperatures under 200 °C, with a specific energy storage density between 30-60 kWh/m^3, the costs are estimated to be under 20 €/kWh. In higher temperature ranges above 250 °C, salt storages are common with energy densities of 150 kWh/m^3 and cost around 60 €/kWh. (Bielsa 2022)

2.8 Battery energy storage system

The battery energy storage system (BESS) is an electrochemical device that converts electrical energy into chemical energy and stores it. The stored energy can be converted back into electrical energy. The capacity refers to the charge a battery can deliver at a set voltage. The battery efficiency is the ratio of the extracted charge to the charge put into the battery. Over time, a battery ages and loses capacity due to losing its active material mass. The active material reacts to unusable material, which cannot be charged in the battery. (cf. Pavlovic 2020, pp. 88–92):

Examples are lead-acid batteries and lithium-ion batteries. The charging of a lead–acid battery is described by the following chemical reaction:

$2 \cdot PbSO4 + 2 \cdot H2O \rightarrow PbO2 + 2H2SO4 + Pb$.

The following chemical reaction occurs, when the battery is discharged (cf. Pavlovic 2020, pp. 91–92):

$PbO2 + 2H2SO4 + PbSO \rightarrow 2 \cdot PbSO4 + 2H2O$ (11).

Some characteristics of a lead-acid battery are:

- Low cost,
- Strongly built,
- Capable of high currents,
- good life span,
- Fast aging, when discharged over long period,
- recyclability and
- low energy density.

Lithium-ion batteries have a high energy density and low self-discharge. However, they can pose a safety hazard, as they are highly flammable. When charged too quickly, a short-circuit could be caused, leading to an explosion. With no sufficient overcharge protection, they can explode due to external short circuits.

For PV applications, the biggest drawback of a lead-acid battery is the fast aging when discharged over a long period. The biggest drawback of a lithium-ion battery is its flammability. (cf. Pavlovic 2020, pp. 91–95)

2.9 Economic calculations

For industrial processes, the price of the supplied energy is important. To compare energy plant systems, the levelized cost of energy is a good cost key figure. They are specific costs for the energy in €/kWh. The levelized cost of electricity (LCOE) represents the cost for electricity power plants and the levelized cost of heat (LCOH) represents the heat cost for thermal plants. They are calculated with the investment cost, the annual running costs, the annual heat output and the discount rate r. The annual cost and heat are discounted with the discount rate *r* over the lifespan from year *t*=1 to the last year t_{end}. Consequently, the LCOH is calculated as (cf. Krüger et al. 2021b, pp. 11–12):

$$LCOH=\frac{Investment\ cost+\sum_{t=1}^{t_{\mathrm{end}}}\frac{Annual\ cost_t}{(1+r)^t}}{\sum_{t=1}^{t_{\mathrm{end}}}\frac{Annual\ heat_t}{(1+r)^t}}. \qquad (2.36)$$

3 Methodology

In this chapter, first, the used simulation tools are described. Then the techno-economic assumptions are listed. Finally, the heat generating systems are presented, and their modeling is explained.

3.1 Tools

3.1.1 Greenius

The software tool greenius is a DLR intern simulation environment (DLR 2022a). The tool is designed to calculate performance and economic figures of merit for several renewable energy systems, such as solar thermal parabolic trough plants, compound parabolic collectors, solar tower systems and photovoltaic systems. The technical simulation of the energy system is calculated hourly for one representative year, which can be used for a multi-year simulation. If necessary, the time resolution of the year can be refined to 30-min, 20-min, 15-min and 10-min. The technical calculations are based on energy balances. The user input of the simulation environment consists of information about the project site, the used technologies and economics. The project site information is made of the information of the nation, the location, the weather data, the load curve, and the operation strategy. For the technologies, the technical, operating and economic data must be given, such as efficiency, operating temperature and specific costs. Additional costs and financing data can be specified, such as cost for engineering, procurement and construction or financing sources and debt financing.

Greenius follows a guideline published by Solar PACES to a large extent, but not completely, due to the earlier development year of greenius. (cf. Dersch et al. 2021, pp. 16–17)
There have been several validation tests. In 2010 and 2011 a model comparison of 10 annual performance models for parabolic trough plants from various research organizations and companies was performed under the auspices of SolarPACES. The results were undisclosed due to some involved companies. In guiSmo two benchmarking rounds have been carried out with greenius involved in both rounds. The first round revealed that in order to get comparable results, the boundary conditions and input data must be defined precisely. In the second round, the annual gross and net output of seven models were calculated with a range of ±6.5 %. Since the simulation was not based on real operation conditions, no actual measurements were available. In the final comparison, the results of greenius were about

2 % lower than of the mean results of the seven considered models. Due to a comparison with the data of an undisclosed supplier, the DLR assumes that the results for a solar tower lie within the same accuracy range as the parabolic trough plants (cf. Dersch et al. 2021, pp. 16–17)

3.1.2 EBSILON Professional

EBSILON Professional from STEAG Energy Services is a simulation tool for thermodynamic cycles. The first version was released in 1990 and has been updated and improved since. The tool has integrated components and a material data library. The operation is based on a Windows based graphical user interface. Models are built with a Drag-and-drop-principle, connected with logic- and material lines. (STEAG Energy Services 2022)
In this thesis, EBSILON Professional is used to create a heat pump model.

3.1.3 Microsoft Excel

Microsoft Excel is a spreadsheet program. It can be used for organizing, manipulating, and storing data. The data are stored in tables, which are organized into rows and columns and are made of rectangular cells. A cell can store number, text, date and time, boolean values and formula data. Formulas can be simply used to calculate with data from other cells or for more complex operations such as locating data from large tables. (French 2020)
In this thesis, Excel is used for storing data and calculating with functions. In this thesis, Excel is used to model the heat generation system which includes the heat pump. Furthermore, the calculated data from greenius are transferred into Excel for post processing.

3.2 Assumptions

3.2.1 General assumptions

The thesis is made for an industry with:

- Heat demand: 5 MW,
- Heat supplied as process steam at 130 °C,
- Condensate return temperature consumer side: 80 °C,
- Constant heat demand (8760 h/year),
- Unlimited land for construction and
- Current heat supplied by gas boiler.

3.2.2 Examined locations

The performance of solar technologies depends on the incoming radiation of the sun. In order to consider different boundary conditions, such as the global horizontal irradiation (GHI) and the direct normal irradiation (DNI), the simulations are carried out for two different locations. Firstly, Würzburg in Germany was chosen, as Germany is the origin country of this thesis, and Würzburg has comparatively high irradiation levels within Germany. Secondly, Almeria in Spain was selected. It has higher irradiation levels and a lower latitude, changing the course of the sun. Table 3-1 lists key data of the latter locations.

Table 3-1: Location data (DLR 2022b)

Site	Würzburg, Germany	Almeria, Spain
Annual GHI	1138 kWh/m^2	1812 kWh/m^2
Annual DNI	1135 kWh/m^2	1918 kWh/m^2
Average temperature	10.1 °C	17.6 °C
Latitude	49.77 °N	36.83 °N
Longitude	9.97 °E	-2.45 °E
Altitude	275 m	5 m

3.2.3 Technical assumptions

- Parabolic trough (DLR 2022b):
    - Collector type: SL4600+ Huiyin70 2015 (Aperture width: 4.6 m, Collector length: 95 m, effective mirror area: 418 m^2, HCE diameter: 6.5 cm, Nominal optical efficiency: 77.1 %). This collector has been used as a typical large aperture trough collector.
    - Six collectors per row
    - Land use factor: 3.73
    - Reference Irradiation: 1000 W/m^2
    - Distance between rows: 13.8 m; Distance between collectors: 0.5 m
    - Tracking axis tilt angle: 0 °
    - Tracking axis azimuth: 0 °
    - Header length: 50 m + (rows-1) *30 m

- Length fraction cold header: 0.5
- Pipe diameter in loops: 0.0525 m
- Specific pipe weight: 5.44 kg/m
- Mean header diameter: MAXIMUM (0.065 m; $\sqrt{rows*0.0525^2}$)*0.66), (Factor 0.66 to compensate for thinning header)
- Header weight from greenius documentation. Specific weight from higher discrete value:

Table 3-2: Specific header weight for mean header diameter, seamless steel pipe

Mean header diameter [m]	Specific weight [kg/m]
0.2	42.55
0.15	28.26
0.125	21.77
0.1	16.08
0.08	11.29
0.065	8.63

- HTF: Pressurized water
- Nominal field outlet temperature: 210 °C
- Nominal field inlet temperature: 130 °C
- Mean mirror cleanliness: 97%
- Degradation: 0.0 % per year
- Auxiliary demand: Constant need: 1 W/m^2 SF aperture
- Power of field pump: 8.3 W/m^2 SF aperture

* Thermal energy storage system:
    - Storage Medium: Water
    - Nominal Hot Temperature: 95°C
    - Nominal Cold Temperature: 75°C
    - Exponential loss function, 50% loss in 693 h

- Pumping parasitics: 0.003 W_{el}/W_{th}

- Pressurized thermal energy storage system:
  - Storage Medium: Pressurized water
  - Nominal Hot Temperature: 210°C
  - Nominal Cold Temperature: 130°C
  - Exponential loss function, 50% loss in 693 h
  - Pumping parasitics: 0.003 W_{el}/W_{th}

- Heat exchanger:
  - Degradation: 0.0 %
  - Efficiency 100 %
  - Pinch temperature 5 K

- CPC field (DLR 2022b):
  - Collector type: Ritter XL 19/49 P (Aperture width: 2.432 m, Collector length: 2.432 m, effective mirror area: 4.94 m^2, Empty weight 72.4 kg, Vacuum tube, Collector pipe diameter: 8 cm, Conversion factor: 0.627).
  - Nominal field outlet temperature: 95 °C
  - Nominal field inlet temperature: 75 °C
  - Elevation 34 °
  - Azimuth 0 °
  - HTF: Water
  - HTF Specific heat capacity: 1.16 Wh/kgK
  - HTF density: 1kg/l
  - Pipe length: 1000 m
  - Pipe diameter: 0.08 m
  - Pipe specific mass: 10 kg/m
  - Pipe specific heat capacity: 0.109 W/mk
  - Pipe isolation thickness 0.03 m
  - Pipe specific heat conductivity 0.109 W/mK
  - Specific parasitics 0.047 W_{el}/W_{th}

- Heat pump:
    - COP 4.2
    - Full start up after 12 h of idle time, start-up time 32 min
    - Only operated at nominal power
    - Heat source: Cool Water from 95 °C to 75 °C
    - Heat sink: Evaporate water from 80 °C to 130 °C
    - Pinch temperature Heat exchangers: 5 K
    - Instant shutdown
    - Degradation: 0.0 %

- PV (DLR 2022b):
    - Bifacial-monocrystalline PV modules (best suited for sandy ground = high albedo)
        - Name: Longi LR4-72-HBD425M
        - Nominal MPP power: 425 W_p
        - Dimensions: Length: 2.131 m, width: 1.052 m, weight: 29.5 kg
    - Single-Axis Tracking Systems (best economics in sunny regions)
    - Inverter
        - FIMER PVS-100-TL
        - Nominal DC power: 102 kW
        - Nominal AC power: 105 kVA
    - DC/AC ratio: 1.29
    - Degradation: 0.0 % per year
    - DC cable length per string: 500 m
    - Diameter DC cable: 10 mm^2
    - Specific resistance 0.0175 ohm mm^2/m
    - Availability: 98%
    - Cleanliness module: 97%
    - Shadowing factor module: 91%
    - Assumption: flat, homogenous site, rectangular area

- Battery energy storage system (DLR 2022b):
    - Round-trip efficiency: 85% related to heating, ventilation and air conditioning (HVAC), self-discharge, battery management system (BMS), power conversion system (PCS) efficiency, etc.
    - Definition of Net capacity: available Energy when discharging from maximum state of charge to minimum state of charge at beginning of life.
    - Lifetime: 25 a
    - Degradation: 0 %
    - O&M cost: 4.5% (0.5% of capital expenditure (CAPEX) for general annual O&M activities + 2% for degradation compensation + 2% for Battery replacement after 15 years).

- Electric resistance heater:
    - Efficiency 95 %
    - HFT: water
    - Instant start up
    - Instant shut down
    - Degradation: 0.0 %

3.2.4 Cost assumptions

The PTC and pressurized thermal energy storage system costs (PTES), with water as a storage medium, are estimated for January 2023 and are provided by an employee of Solarlite CSP Technology GmbH. (Solarlite CSP Technology GmbH 2023)
Additionally, a personal conversation with the Solarlite CSP Technology GmbH led to the assumption of a surcharge of 30 % on prices before 2019 for technologies with steel, reasoned with the rising steel prices. (Solarlite CSP Technology GmbH 2023)

The costs for the shell and tube heat exchanger were calculated with the paper from Wildi-Tremblay et al., with a heat transfer area of 136 m^2, δ_M = 2.9, δ_P = 1.2 and δ_T = 1.3. (Wildi-Tremblay and Gosselin 2007). A 30 % surcharge is added due to the increasing steel prices since the publication date. The EPC surcharge are assumed with 20 %.

The prices for the CPC collector are provided by an undisclosed industry.
The TES costs from the literature are in €/m^2. They are converted into €/kWh with the specific volume per energy of the storage. In the literature, the TES cost sink with increasing capacities. Therefore, the price scales from 9 €/kWh with a 24-hour capacity up to 20 €/kWh for a three-hour capacity. (Celsius 2020) The price has a surcharge of 30 % due to the publication date before 2019 and is assumed with an EPC-surcharge of 20 %.

The heat pump price is oriented on the paper of Jesper et al. and the price range given by Wolf. (cf. Wolf 2017, p. 25; cf. Jesper et al. 2021, p. 7)

The PV module and inverter price are taken from the Irena study. The EPC-surcharge in the Irena study includes inspection, margin, financing costs, system design, permitting, incentive application and customer acquisition. The installation prices are proportionally added to the PV module and inverter investment prices. The study has different prices for Germany and Spain listed and therefore used in this thesis. (IRENA 2022, p. 89)

The BESS has costs per capacity and per power (NREL 2022).

The electric resistance heater cost is taken from the IntegSolar project. (cf. Dersch and Schonmaker 2021, 23). The cost for the electric resistance heater that evaporates the water to 130 °C has an additional 50 % price surcharge. (DLR 2022b)

The investment costs of every system contain the balance of plant costs.

The land costs are assumed for agricultural land. For Germany, the land costs are assumed for Würzburg (Proplanta 2019). For Spain, the land costs are assumed for Andalusia (Eurostat 2021).

The electricity cost for Germany is assumed for a company with an annual electricity demand of 2000-20000 MWh from 2021 (Blümm 2022). The Gas price was assumed in the middle of October 2022 (Bundesnetzagentur 2022).

The gas and electricity prices for Spain are assumed from June 2022 (GlobalPetrolPrices.com 2022).
Table 3-3 lists the enumerated costs.

Table 3-3: Cost assumptions

Technology	Investment	EPC Surcharge [% Investment]	O&M cost [%Investment]
Parabolic trough collector	250 [€/m^2]	20	1
Pressurized thermal energy storage	50 [€/kWh]	20	1.5
Shell and tube evaporator	275000 [€]	20	0
CPC collector	350 [€/$m^{2]}$	20	1
Thermal energy storage	11.7-26.0 [€/kWh]	20	1.5
Heat pump	400 [€/kW]	20	1
PV modules, Germany	555.58 [€/kW_{dc}]	8	0,5
Inverter, Germany	62.32 [€kW_{ac}]	8	0.5
PV modules, Spain	602.95 [€/kW_{dc}]	17	0.5
Inverter, Spain	70.14 [€kW_{ac}]	17	0.5
Battery Cost per power	174.32 [€/kW]	22	4.5
Battery Cost per energy capacity	226.33 [€/kWh]	22	4.5
Electric resistance heater, 210 °C	105.26 [€/kW_{th}]	20	1
Electric resistance boiler, 130 °C	157.89 [€/kWth]	20	1
Land cost Germany	5 [€/m2]	-	-
Land cost Spain	2.5 [€/m2]	-	-
Gas cost Germany	0.106 [€/kWh]	-	-
Gas cost Spain	0.13 [€/kWh]	-	-
Electricity cost Germany	0.20 [€/kWh]	-	-
Electricity cost Spain	0.14 [€/kWh]	-	-

3.3 Procedure for the heat generation systems

3.3.1 PTC field with PTES

As described in chapter 2.3, parabolic trough collectors can supply heat at 130 °C, and therefore a system with these collectors is chosen in this thesis. Figure 3-1 portrays the schematic of a system with this type of collector.

The parabolic trough field generates heat during the day, if the irradiation is sufficient. Although the collector could directly supply steam at 130 °C, in order to integrate a cost-efficient storage, the collector is operated with pressurized water as a heat transfer fluid (HTF). The HTF is heated from an inlet temperature of 130 °C to an outlet temperature of 210 °C. The temperature is limited to 210 °C because at higher temperatures and pressures, the PTES would become too heavy and expensive (Solarlite CSP Technology GmbH 2023). A heat exchanger is integrated between the solar field and the consumer steam system. The HTF is used in the heat exchanger to evaporate water from 80 °C to 130 °C on the consumer site. To increase the capacity factor of the solar field, a PTES is integrated. The capacity factor is defined as the ratio of the total used energy of a system to the energy demand of the consumer. The total used energy of a solar energy generating system can be heat $Q_{s,tot}$ and electricity $W_{s,tot}$. The most cost-efficient solution for this temperature level is a sensible thermal energy storage. As the storage medium, pressurized water with a temperature lift from 130 °C to 210 °C is chosen.

The auxiliary electricity demand is provided by the grid.

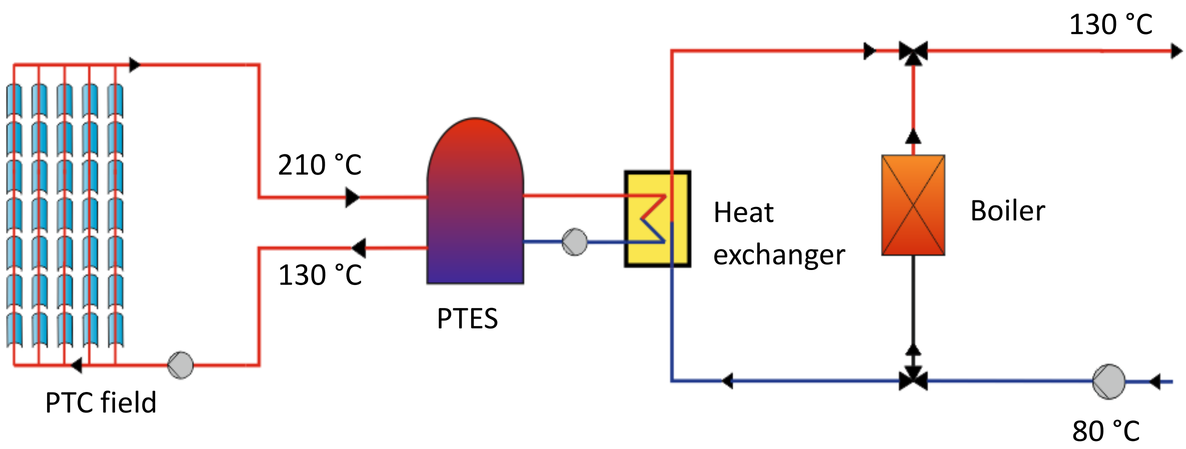

Figure 3-1: PTC field with PTES

This system is fully simulated with the software greenius.
The PTC is simulated as described by equations 2.9-2.11. The storage is not simulated as a thermocline storage, but rather through charging and discharging of heat on the current stored energy. The thermal losses are proportional to the storage content and are calculated with an exponential loss function. The heat exchanger is assumed with an efficiency of one. Hence, it doesn't reduce the generated heat while exchanging it to the consumer cycle.
At heat-up, the PTC field and the piping system are simulated with a homogeneous temperature. In greenius, the collector field is completely heated up when the system reaches the arithmetic mean temperature. The needed heat for the start-up process correlates to the heating capacity of the individual components of the system. The cooldown of the system is calculated with a homogenous temperature as well.

In the optimization process of the system, the PTES capacity and the parabolic trough collector field size are varied. This system will further be referred to as PTC_PTES system.

3.3.2 CPC collector field with TES and heat pump

In this system, the CPC collector is chosen as the solar thermal collector. Figure 3-2 shows the scheme of the complete system. CPC collectors with water as HTF can generate heat of up to 95 °C. A higher temperature would lead to the vaporization of the water. To provide heat at 130 °C, a heat pump is integrated.
The CPC field generates heat during the day. A sensible thermal energy storage is integrated, in which excess heat from the CPC collector field can be stored. Thus, increasing the capacity factor. The heat pump uses the generated heat from the CPC collector field as a heat source. It evaporates the water on the consumer side, therefore supplying the steam at 130 °C. The heat pump is a compression heat pump, working as explained in chapter 2.5. In one scenario, the electricity for the heat pump is completely supplied by the grid, and in a second scenario with a combination of the grid with a PV field with BESS.

With the semiempirical approach (equation (2.28)) described in chapter 2.5, Jesper et al. suggest a COP for the temperature lift of 35 K of about 4.2 (cf. Jesper et al. 2021, 23–24). However, in the study, no specific pinch temperatures are considered. In addition, the return flow temperature of the heat source and the incoming temperature of the heat sink are not taken into consideration. Therefore, an EBSILON Professional simulation was carried out for the heat pump to gain more information about the COP and the mentioned temperatures.

With the COP of 4.2 and a pinch temperature of 5 K for the heat exchangers, the EBSILON simulation results in the temperatures shown in Figure 3-2. For further simulations, a COP of 4.2 and the latter temperatures are used.

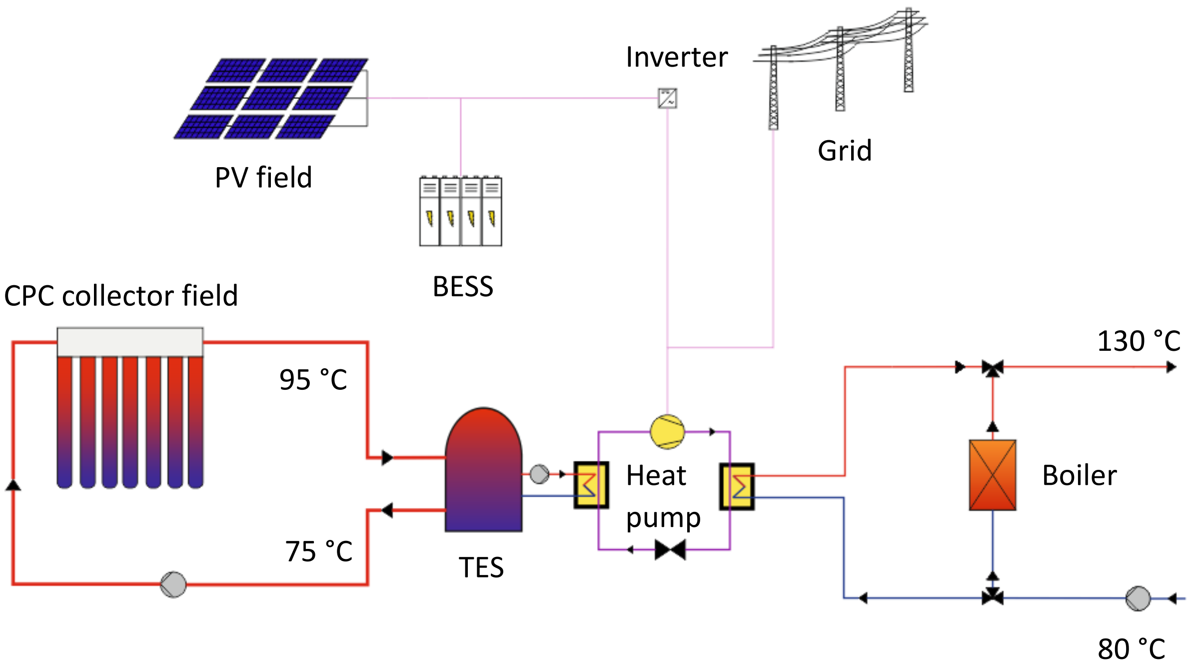

Figure 3-2: CPC collector field with TES and heat pump

The CPC collector field is calculated with greenius, as described in chapter 2.3. The heat-up of the CPC collector system is simulated with a homogeneous temperature until 85 °C is reached. The needed heat for the start-up process correlates to the heating capacity of the pipes and collector of the system

The combined system of the heat pump, TES and CPC collector field is simulated in an Excel tool.

The heat output of the CPC collector field is transferred into the Excel tool. With the heat output information of the CPC collector field, the heat pump is simulated with the equations explained in chapter 2.3. In addition, the heat pump is only operated at nominal power to increase the efficiency. The heat pump has to start, when not operated for twelve hours. The startup takes 32.5 minutes because the condenser is assumed with a 2 K/min heat-up limit. The refrigerant has to be increased from 70 °C to 135 °C. During the startup, no heat can be supplied. (cf. Oehler et al. 2022, p. 5)

The TES is calculated in the same way in Excel as in greenius. The auxiliary electricity demand for the CPC collector field and TES is simulated in the Excel tool and is always covered by the grid.

The Excel tool can only calculate with the electricity provided by the grid. To integrate a PV system, the calculated electricity demand of the heat pump can be set as a load curve for a PV field simulation in greenius. The simulation of the PV system in greenius is described in subchapter 3.8. The PV system is simulated for various BESS capacities and PV field sizes. The LCOE for the corresponding capacity factor is calculated. Using the LCOE and the capacity factor of the PV field, with the remaining electricity supplied from the grid, the total electricity cost for the heat pump can be calculated. The minimum electricity costs are transferred in the Excel tool.

The optimization is made for the TES capacity and CPC collector field size. This system will further be referred to as CPC_HP_TES or CPC_HP_TES_PV system, depending on if a PV field is integrated.

3.3.3 PV field with BESS and electric heater

In this system, the PV collector is researched as a competitor to the thermal collectors. Figure 3-3 shows the complete system.
Multiple PV modules are connected to one string. Several strings are connected to one inverter. The complete PV system is made up of parallel connected inverters. With sufficient irradiation over the day, the PV collector field generates electricity. The direct current (DC) of the PV field is inverted to an alternating current (AC) by the inverter. An electric heater is integrated to convert the electricity into heat. The electric heater heats and subsequently boils the water on the consumer site from 80 °C to 130 °C.

In times of overproduction, electricity is used to charge a BESS. The BESS is discharged when the PV field doesn’t generate enough power to supply the demand.

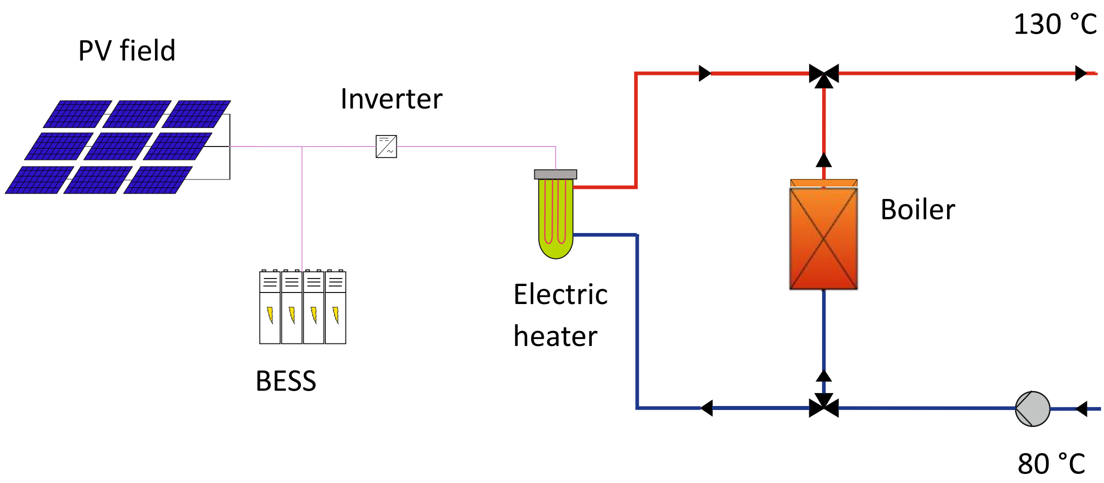

Figure 3-3: PV field with BESS and electric heater

The PV field, the inverter, and the BESS are simulated by greenius. The PV field in greenius is calculated as described in chapter 2.4. For the inverter, an efficiency load curve is implemented. The BESS is simulated with a steady efficiency, describing the relation of stored energy to utilized energy.

Because the electric heater is not implemented in this specific greenius system, the results of the PV field simulation are transferred to Excel and offset against the efficiency of the electric heater. For example, the electricity output is reduced by the efficiency of the electric heater to convert electricity into heat, and the LCOE is increased by the efficiency of the electric heater to convert it into the LCOH.

In the optimization, the BESS capacity and the PV field size is varied. The loading power of the BESS is scaled accordingly to the PV field nominal power. This system will further be referred to as PV_EH_BESS system.

3.3.4 PV field with PTES and electric heater

Compared to the system in chapter 3.3.3, this system differs regarding the storage system. Due to the high investment costs of the BESS, a PTES is used. The system is shown in Figure 3-4.

As well as with the other PV system, the PV field generates a DC current, which is inverted into AC current. The generated electricity is converted into heat with an electric heater. However, the electric heater in this system heats pressurized water from 130 °C to 210 °C. Consequently, a PTES can be used. Identical to the PTC_PTES system, a heat exchanger is integrated, in which

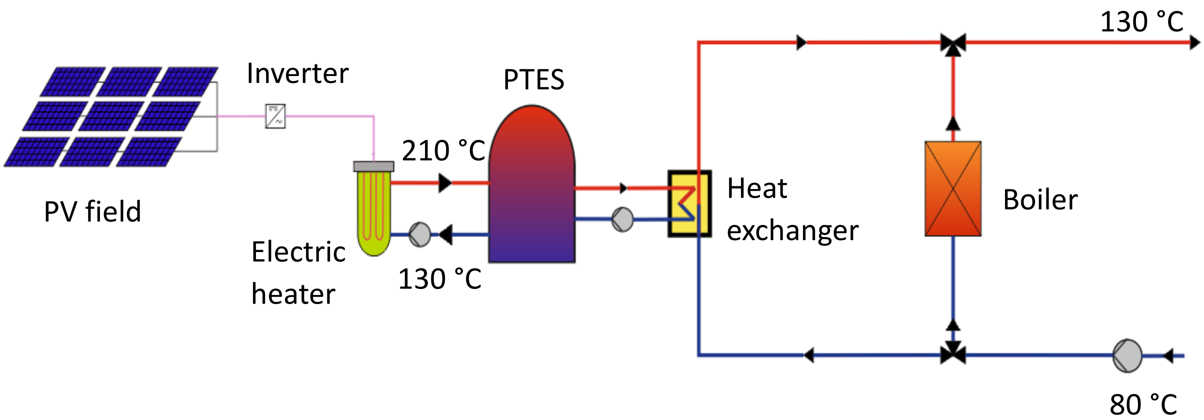

Figure 3-4: PV field with PTES and electric heater

the HTF of the electric heater evaporates the water on the consumer site to 130 °C.

The system is completely simulated with greenius. For the PV field, one representative system with one inverter is designed. The number of systems is scaled up to reach higher nominal powers. The 95 % efficiency of the electric heater is modeled as 5 % losses of the PV field. The PTES is simulated in greenius in the same way as already described in the previous chapters.

The optimization is made for the PTES capacity and PV field size. The power of the electric heater is adjusted to the PV field nominal power so that the whole generated electricity can be converted. This system will further be referred to as PV_EH_PTES system.

4 Results

In this chapter, the results of the simulations are presented. First, the results for each individual system are presented. Then the systems are compared in Würzburg. Subsequently, the results for Würzburg and Almeria are compared. Finally, an ideal calculation regarding the economic competitiveness of the systems is carried out.

4.1 Results for the heat generating systems with scaling of the system sizes

Figure 4-1 shows the results of the PTC_PTES system in Würzburg. The LCOH is plotted over the capacity factor for various storage capacities. With a constant storage capacity, the capacity factor increases with increasing PTC rows. With a constant PTC field, the capacity factor can be increased with a higher storage capacity if dumped heat can be stored.

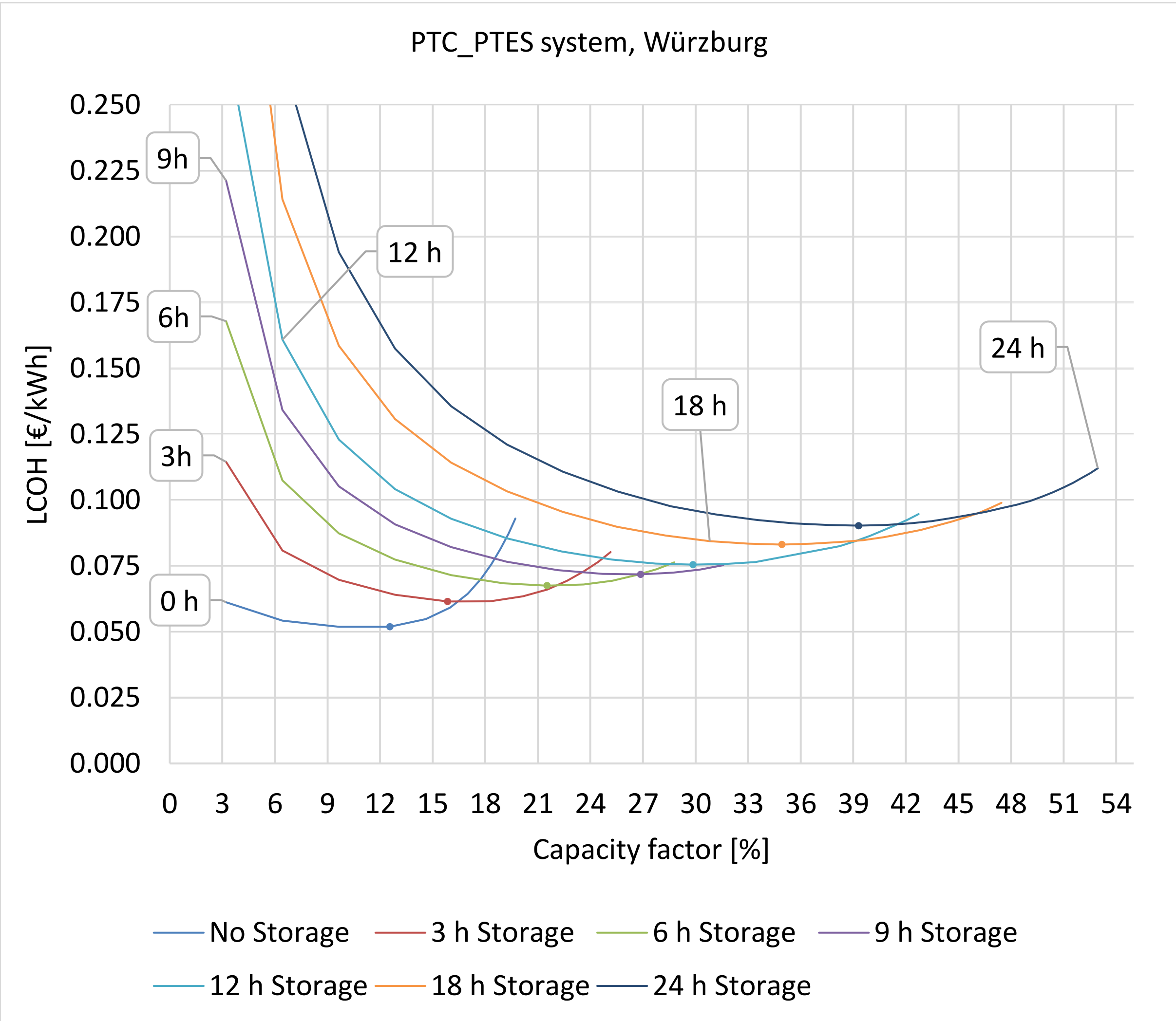

Figure 4-1: LCOH over capacity factor, PTC_PTES in Würzburg

The increase in capacity factor with each additional collector row decreases from the point where heat has to be dumped. Because the row number at which heat has to be dumped differs for each storage capacity, the field size can differ at the same capacity factor for each PTES capacity.

The curves for each storage capacity have a minimum, marked with a point. The LCOH before the minimum decreases for all curves because the system has initial investment costs besides the investment costs of the PTC field. The ratio of $Q_{s,tot}$ to additional investment cost for rows left from the minimum is high enough to decrease the LCOH of the system. Consequently, right from the minimum the mentioned ratio is too low. Thus, the LCOH increases. Without the additional investment costs, the system would have a constant LCOH until the first heat has to be dumped.

Integrating a storage and increasing its capacity increases the initial investment costs. However, energy can be stored. Therefore, more rows can be operated until heat has to be dumped. Therefore, the minimum shifts to higher capacity factors with increasing storage capacity.

For example, the minimum for a system without storage is with four rows reaching a capacity factor of 12.55 % with a LCOH of 0.0519 €/kWh. For a 24-hour storage it is with 14 rows, a capacity factor of 39.31 % and a LCOH of 0.0903 €/kWh.

It can be observed that the LCOH for the minimum storage increases with the integration of a storage. This means that the ratio of annual stored and utilized energy to the investment cost is too low to decrease the overall LCOH.

At some point for each storage capacity, the capacity factor cannot be much further increased by larger collector fields and the gradient of the curve increases. The intersection between the curves of two storage sizes is the point where the higher storage size becomes the economically better system.
If the intersection is right from the LCOH minimum of the higher storage capacity, the system with the higher storage capacity first becomes more economically beneficial after the intersection, and the LCOH minimum of the higher storage size is not the overall LCOH minimum. At which capacity factor the intersection takes place depends on the economic

performance of the additional storage size. In Würzburg, the first intersection point right from the LCOH minimum is at a capacity factor of 16.20 % with a LCOH of 0.0625 €/kWh.

In contrast, Figure A-0-1 shows that in Almeria, this scenario first takes place at a storage capacity increase from 12 hours to 18 hours at a capacity factor above 62 %.

Figure 4-2 shows the results for the CPC_HP_TES system with and without a PV field. The system with a PV field is only calculated for the minima of the latter system. The LCOH is plotted over the capacity factor.

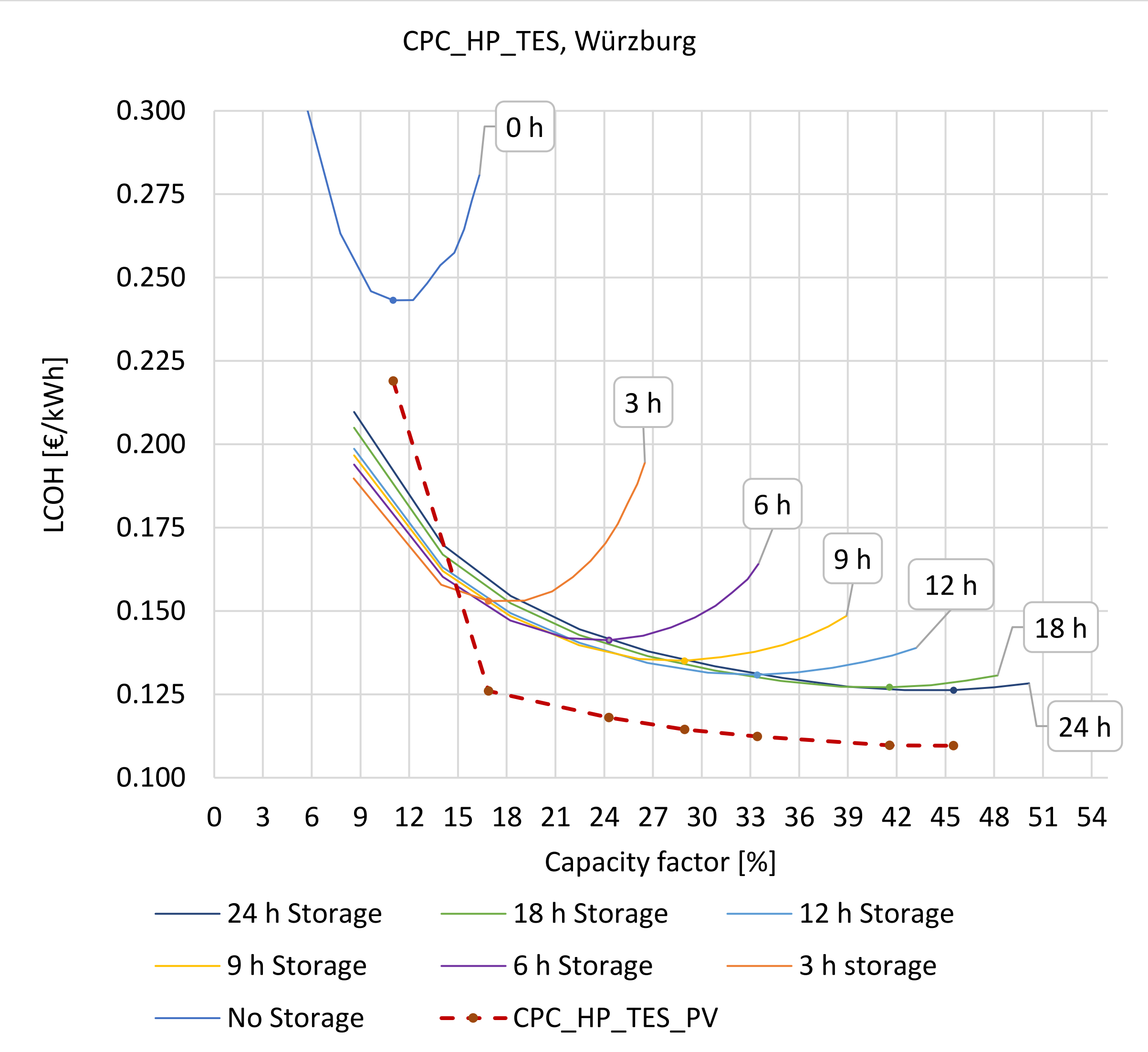

Figure 4-2: LCOH over capacity factor, CPC_HP_TES in Würzburg

The first to notice is the curve without storage. The heat pump only operates at nominal power. Therefore, with no storage, the needed heat from the CPC collector field is always

3.8 MW. When the CPC collector field power doesn’t reach this threshold, the heat is dumped, and when it is reached, all excess heat is dumped. Consequently, the LCOH increases. For the optimal configuration, 56 % of the collector field heat has to be dumped.

The uneven course of the curve also has to do with the threshold because increasing the CPC collector capacity leads to reaching the threshold on more days. However, this does not happen evenly. The integration of a storage removes the threshold. Therefore, more heat from the CPC collector field can be utilized.

For each storage capacity, there is a minimum for the LCOH. As already explained for the PTC_PTES system, left from the minimum the ratio of $Q_{s,tot}$ to investment costs for CPC collectors is high enough to decrease the LCOH, and on the right the ratio is too low, thus increasing the LCOH.

For this system, the LCOH of the minimum of each curve decreases with increasing storage capacity for several reasons. Firstly, the TES is cheaper than the PTES. Secondly, increasing the supplied heat of the CPC collector field through larger storage capacities and larger CPC collector fields leads to greater utilization of the heat pump, while the investment costs are static.

The minima do not change with the integration of a PV field. Thus, in the scope of this thesis only the minima of the CPC_HP_TES are plotted with a PV field. Observably, the overall LCOH decreases with a PV field because the electricity supplied by the PV field is cheaper than from the grid. Table 4-1 lists the data for the optimal PV field for each optimal CPC_HP_TES configuration:

Table 4-1: PV configuration, CPC_HP_TES_PV, Würzburg

TES Capacity [h]	Heat Pump electricity demand [MWh]	PV BESS Capacity [h]	Nominal Power [MW]	LCOE [€/kWh]	Capacity factor [%]
0	1290	0	1.5	0.0945	86.20
3	1945	0	1.7	0.0745	82.10
6	2685	0	2.0	0.0727	71.73
9	3159	0	2.0	0.0702	63.16
12	3617	0	2.0	0.0684	56.59
18	4455	0	2.3	0.0674	53.63
24	4657	0	2.3	0.0653	50.77

The BESS investment costs are too high for it to be economically advantageous. Thus, the most economic configurations are without a storage. For low TES capacities, a high capacity factor can be achieved with the PV field because the heat pump only operates during hours with sufficient irradiation for both the CPC collector field and the PV field. With higher TES capacities, the operating hours of the heat pump at night increase, during which no electricity can be supplied by the PV field. Therefore, the capacity factor decreases. The LCOH decreases as well because more electricity from the PV field can be used, and less has to be dumped due to the higher demand.

The results for Almeria are depicted in Figure A-0-2. The corresponding PV field data are listed in Table A-0-1. Compared to Würzburg, the capacity factor of the PV field for low TES capacities is higher due to higher irradiation levels. For higher TES capacities, the night operating hours are higher, and the capacity factor is lower. It has to be considered that the electricity grid price in Almeria is lower than in Würzburg, which lowers the economically advantageous PV capacity factor.

Figure 4-3 shows the results for the PV_EH_BESS system in Würzburg. The LCOH is plotted over the Capacity factor.

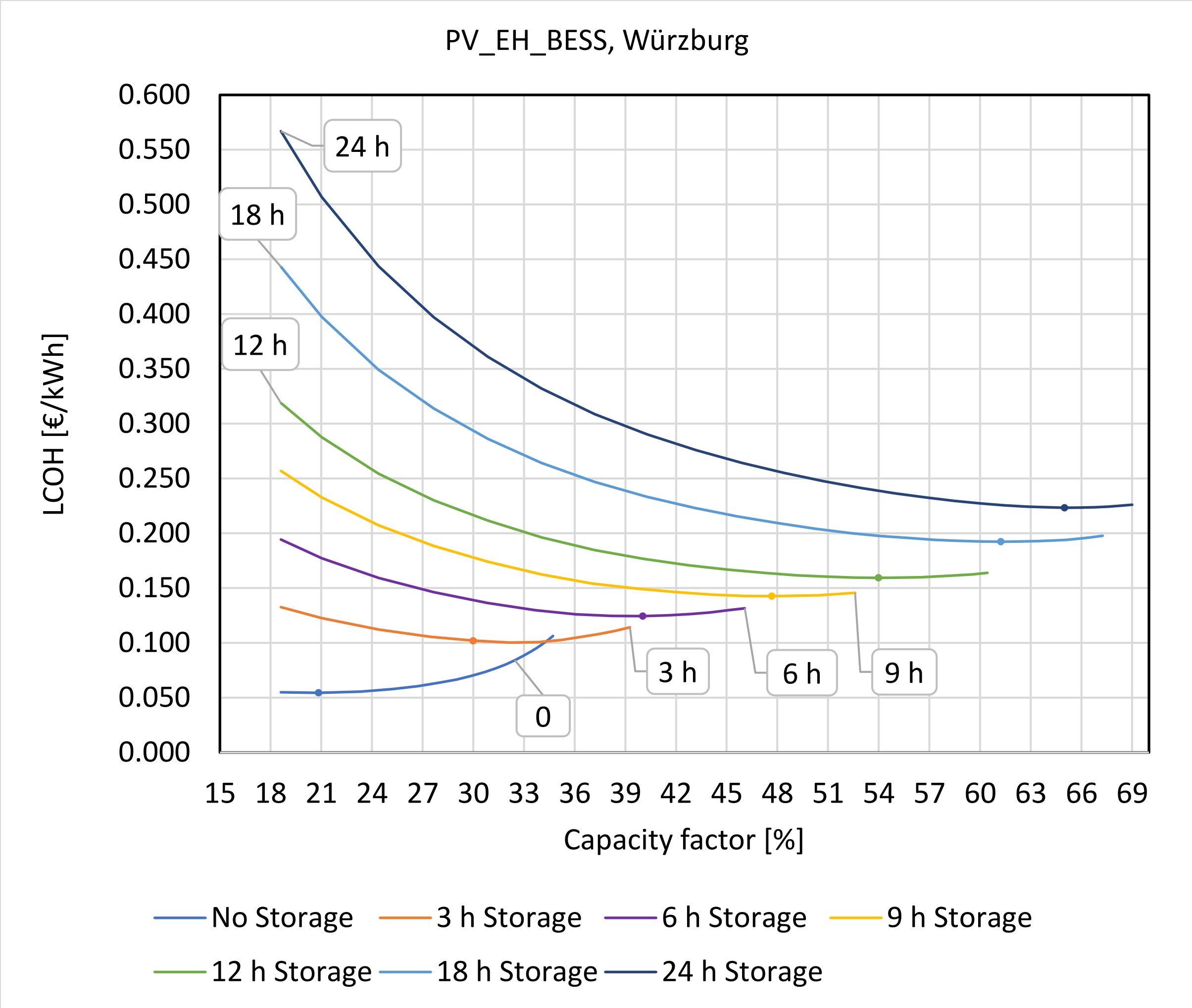

Figure 4-3: LCOH over capacity factor, PV_EH_BESS in Würzburg

The curves for this system have a minimum for each storage capacity. The reason for the minimum is already explained for the PTC system. A noticeable difference for this system is the distance between the curves. Compared to the TES and PTES, the BESS cost is significantly higher. Therefore, increasing the BESS increases the LCOH more significantly.

The results for Almeria are shown in Figure A-0-3. The behavior of the curves is the same as in Würzburg. The difference is the lower LCOH while reaching higher capacity factors

Figure 4-4 shows the results for the PV_EH_BESS system in Würzburg. The LCOH is plotted over the Capacity factor.

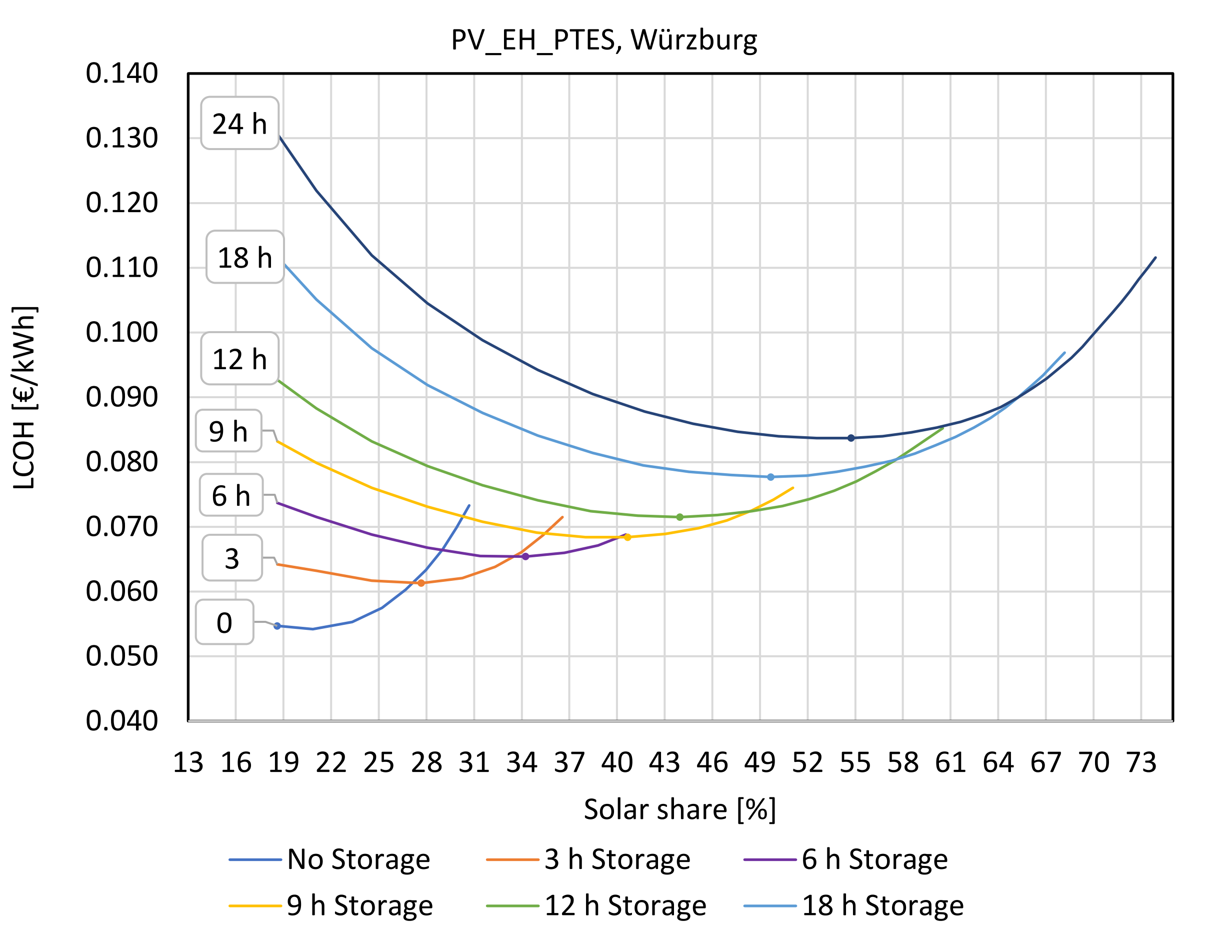

Figure 4-4: LCOH over capacity factor, PV_EH_PTES in Würzburg

The curves for this system have a minimum for each storage capacity as well. With the integration of a storage, this system achieves lower LCOH compared to the BESS system. As opposed to the latter two systems, the PV_EH_PTES system achieves similar results to the PTC_PTES system.

The results for Almeria are shown in Figure A-0-4. The main difference is that in Almeria higher capacity factors are achieved with lower LCOH.

4.2 System comparison in Würzburg

Figure 4-5 shows the LCOH over the capacity factor for all systems. Plotted are the LOCH minima of each storage capacity, whereby the effect of increasing storage capacities can be observed well. The CPC_HP_TES system is plotted with and without a PV field.

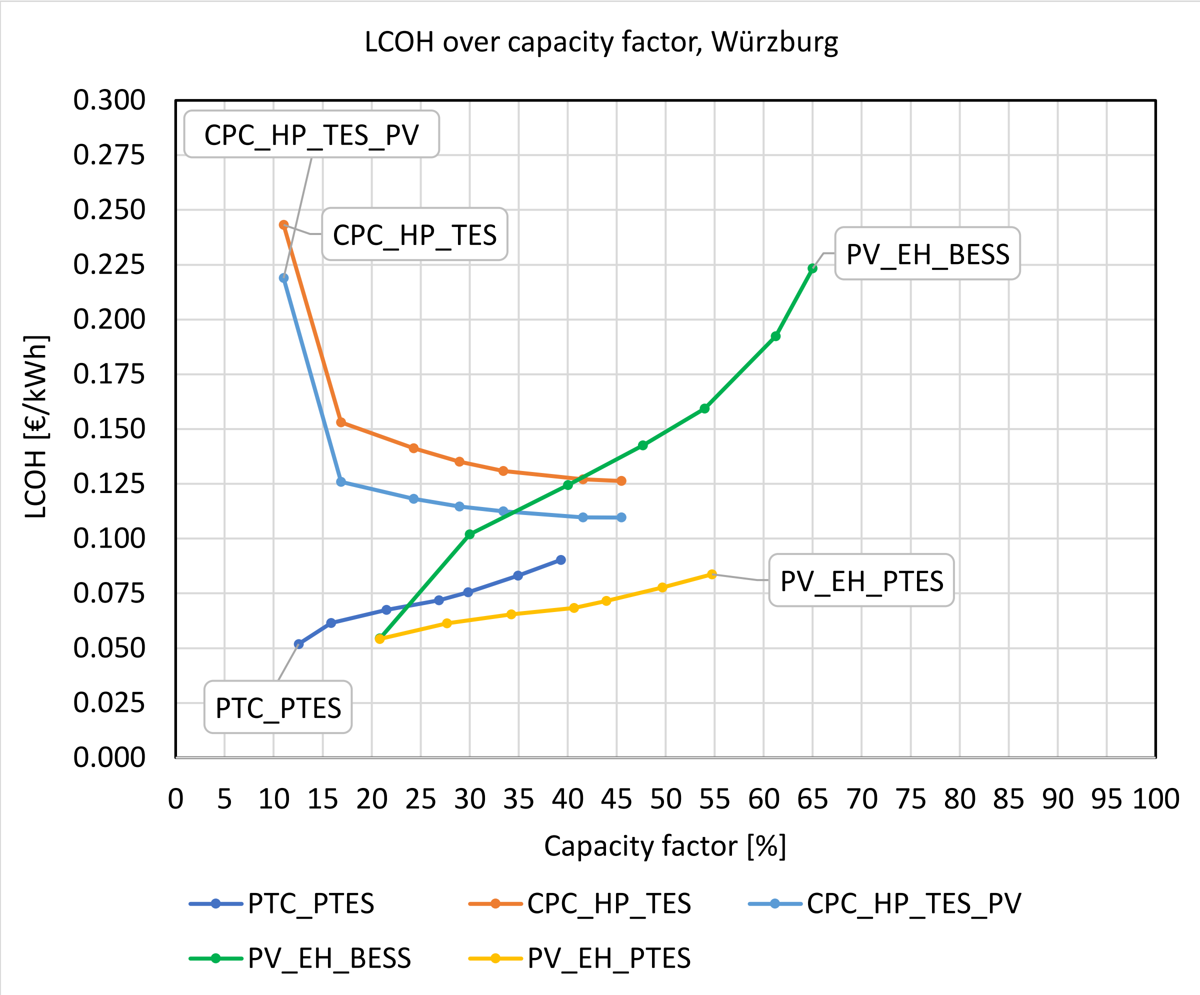

Figure 4-5: System result comparison. Minimum LCOH for every storage capacity over capacity factor, Würzburg

When comparing the systems with no storage capacity, the PTC system achieves the lowest LCOH with 0.0519 €/kWh at a solar share of 12.55 %, and the PV systems have the highest solar share with 20.84 % but a higher LCOH of about 0.0542 €/kWh. The PV systems have a higher capacity factor because, firstly, PV technology converts diffuse and direct irradiation, and secondly, it doesn't have to heat-up to an operating temperature. However, the investment for the PV system is higher than for the PTC system, thus resulting in a higher LCOH despite the higher heat output.

Without a storage, the CPC_HP_TES system has the highest LCOH, because of the high static investment costs while having a low heat output due to the discrete operating strategy for the heat pump. The electricity generated by the PV field of the CPC_HP_TES_PV system is cheaper than the grid electricity, thus lowering the LCOH. However, the LCOH reduction is too insignificant to make the system competitive.

Table 4-2 lists the LCOH minima of the systems with a six-hour storage capacity. It shows that the PV_EH_PTES achieves the lowest LCOH. It also shows that different nominal collector powers lead to different capacity factors. For example, the PV_EH_PTES system has a 12.72 % higher capacity factor with 3000 kW less nominal power.

Table 4-2: Minimum LCOH of each system for a six-hour storage capacity, Würzburg

System	Nominal power collector field	Area [m²]	Investment cost [10^6 €]	$Q_{s,tot}$ [MWh]	LCOH [€/kWh]	Capacity factor [%]
PTC_PTES	12937 kW_{th}	65484	7.67	9476	0.0675	21.52
CPC_HP_TES	10103 kW_{th}	43225	9.17	10645.2	0.1412	24.30
PV_EH_BESS	13000 kW_{AC}	221491	23.31	17536.05	0.1244	40.04
PV_EH_PTES	10000 kW_{AC}	170378	12.67	14996	0.0654	34.24

In Figure 4-5, it can be observed that with increasing storage capacity, the LCOH of both systems with PV and the PTC_PTES system increases. The LCOH increase for the BESS system is higher than for the PTES systems because the BESS is significantly more expensive. In contrast, the CPC_HP_TES system is the only system with decreasing LCOH for the minima, for reasons explained in chapter 4.1.

For all systems, the capacity factor of the optimal configuration increases with the storage capacity because, in every system, a larger collector field can be utilized without dumping energy.

When comparing the PV_EH_BESS and PV_EH_PTES systems, it can be observed that the capacity factor for the minima of the PV_EH_BESS system is higher. This is not because the PV_EH_BESS system generates more heat, but rather because the BESS is more expensive. The economically advantageous ratio of investment to $W_{s,tot}$ of PV modules is shifting to higher values, which means that additional poorly performing PV modules can lower the total LCOH. Consequently, the minimum for the BESS capacities is reached with a larger PV field. For example, Figure 4-4 shows that the PV_EH_PTES system reaches a capacity factor of 65.2 % as well, however with a LCOH of 0.09 €/kWh compared to the PV_EH_BESS system with a LCOH of 0.2233 €/kWh.

The comparison of the PV systems and the PTC systems in Würzburg shows that the PV systems have a generally higher $Q_{s,tot}$ for all storage capacities. While the LCOH for the PV_EH_BESS system increases more than for the PTC_PTES system with increasing storage capacity, the LCOH of PV_EH_PTES scales comparatively. As already mentioned, without a PTES the PTC_PTES system has a lower LCOH. However, with the integration of the PTES, the PV_EH_PTES system has a lower LCOH because the PV modules utilize the storage more due to the higher $Q_{s,tot}$
In conclusion, for Würzburg, the PV_EH_PTES system reaches the highest capacity factors with the lowest LCOH values.

In certain scenarios, when comparing these systems, other key figures besides those already mentioned must be considered. For example, when constructing a power plant, the available land can be limited. Therefore, the land use can become relevant.

Figure 4-6 shows $Q_{s,tot}$ over the installed area of the different systems. The plotted area and heat output are from the LCOH minima configurations of each storage capacity.

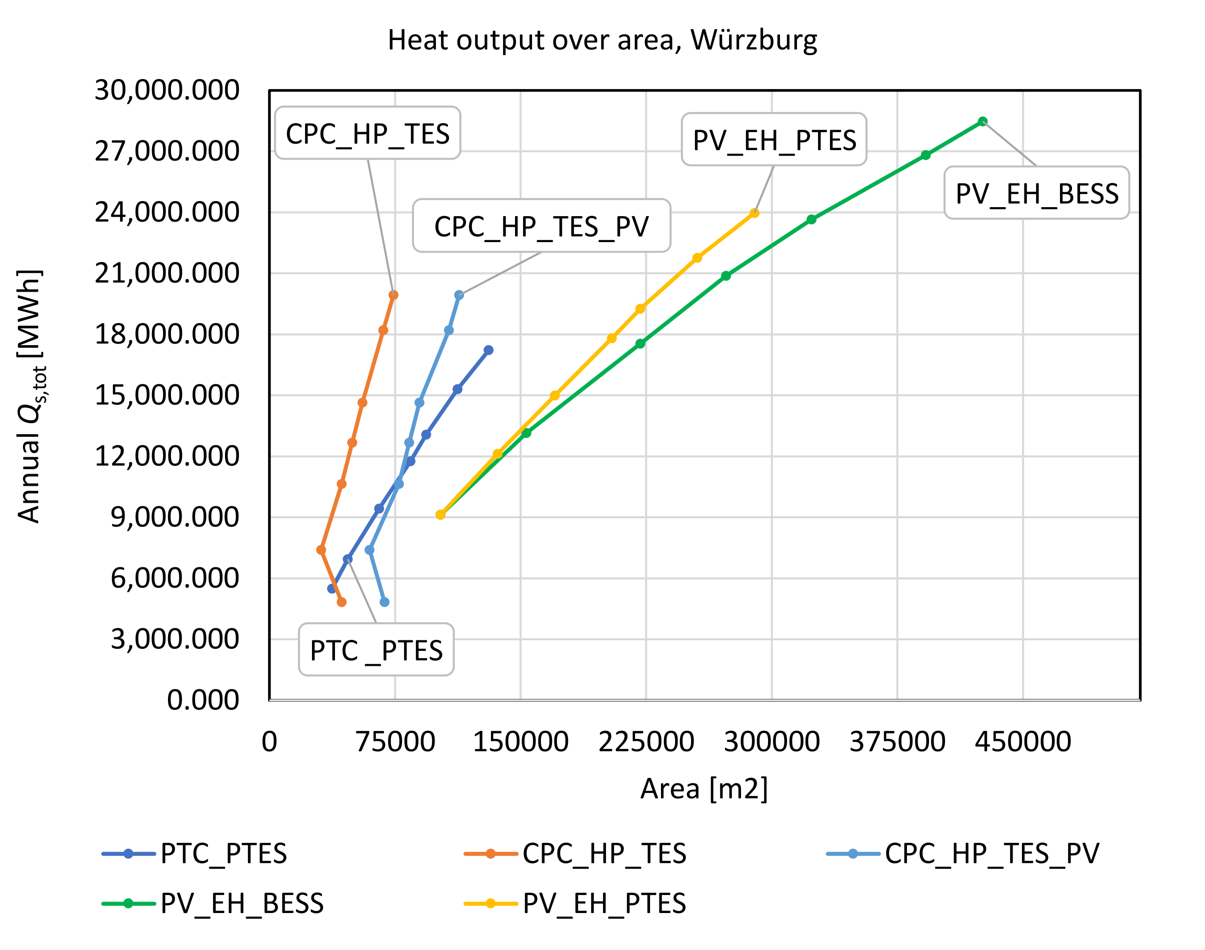

Figure 4-6: $Q_{s,tot}$ over area, Würzburg

The first thing to notice is the size difference between the PV system and the concentrating thermal collector systems. The gradient of the curves represents the specific $Q_{s,tot}$ per area. For the PV curves this gradient, is smaller than for the concentrating thermal collectors, which explains the higher land use of PV modules for equal $Q_{s,tot}$. For example, for $Q_{s,tot}$ of 17811 MWh an area of 203353 m^2 is needed for the PV_EH_PTES system, whereby the PTC_PTES system only needs 130 968 m^2 for nearly the same $Q_{s,tot}$.

The gradient difference between the CPC systems and the PTC system is because the CPC collector field doesn't generate the complete heat. A share of the heat is generated by the heat pump, which does not use additional land.

Between both PV systems, a slight difference is noticeable because the storage efficiency of the PTES is higher than that of the BESS. Consequently, the complete system has a higher efficiency.

The decrease in the CPC collector area, with the integration of a storage, is because the threshold of the heat pump operating point doesn't have to be reached and less heat is dumped. Therefore, a smaller collector field has a higher $Q_{s,tot}$.

The difference between the CPC_HP_TES and the CPC_HP_TES_PV system is the area of the PV field. It must be noted that the grid electricity doesn't have an assigned area consumption. Thus, the CPC variance with a PV field has a higher area consumption.

In conclusion, the area analysis shows the differences in the system sizes. Depending on the available area and type of area, this fact has to be considered. In general, PV fields need the most area. However, PV modules, as well CPC collectors, have the advantage that they can be installed on roofs.

4.3 Location Comparison, Würzburg-Almeria

Figure 4-7 shows the results for Almeria in the same style as for Würzburg.

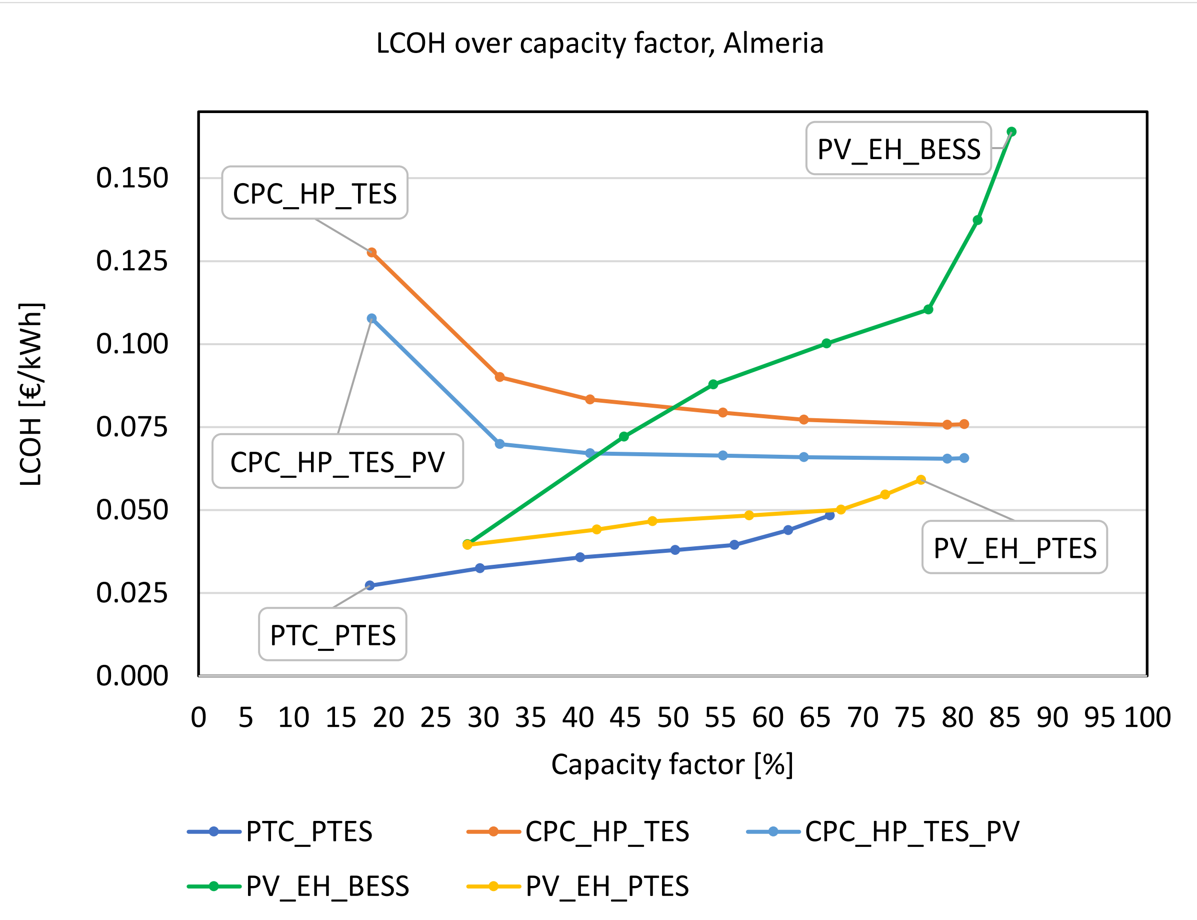

Figure 4-7: System result comparison, minimum LCOH for every storage capacity over capacity factor, Almeria

With no storage capacity, the PTC_PTES system has the lowest LCOH with 0.0272 €/kWh at a capacity factor of 18.073 %. The PV systems, in comparison, have a LCOH of 0.0395 €/kWh at a capacity factor of 28.36 %. The difference between both LCOH's is more significant in Almeria. To some extent because the share of direct irradiation is higher, but also because the investment cost of the PV field is assumed higher for Almeria. The CPC collector systems without a storage cannot compete in Almeria as well.

To show the relationship between the PTC_PTES and PV_EH_PTES system for both locations, Table 4-3 shows the annual $Q_{s,tot}$ of the PV_EH_PTES and PTC_PTES field with no storage. The PTC has a nominal power of 16634 kW_{th}, and the PV_EH_PTES system has a nominal power of 16625 kW_{th}

Table 4-3: Annual $Q_{s,tot}$ for a nominal power of 16625 kW_{th} for PV_EH_PTES and 16634 kW_{th} for PTC_PTES system without a storage

	PV system		PTC system	
	Würzburg	Almeria	Würzburg	Almeria
Annual $Q_{s,tot}$	14516 MWh,	18699 MWh,	8035 MWH	13940 MWh,

Obviously noticeable is the higher $Q_{s,tot}$ in Almeria compared to Würzburg. In Würzburg, the PV system has 6481 MWh more $Q_{s,tot}$, in contrast, in Almeria only 4759 MWh. Relatively, the PV system has 80.66 % more $Q_{s,tot}$ in Würzburg, but only 34.14 % more $Q_{s,tot}$ in Almeria.

In Almeria, with the integration and upscaling of a storage In Almeria, the LCOH of the PTC_PTES system remains lower than that of the PV_EH_PTES system. However, the capacity factor reached with the PV systems is still higher because the diffuse irradiation can be converted. A comparison of Figure A-0-4 and Figure A-0-1 shows that the PTC_PTES system achieves a lower LCOH up to the capacity factor of about 89 %. The PTC_PTES system approaches its capacity factor limit, while the PV_EH_PTES system does not. The PV_EH_BESS system in Almeria performs relatively the same as in Würzburg. The BESS investment costs are too high to compete with a PTES. The CPC_HP_TES_PV system cannot compete in Almeria either.

Noticeable for the CPC_HP_TES system is the small increase in capacity factor with the increase from an 18-hour storage to a 24-hour storage. For a CPC collector field with 7000

collectors, the interval between sufficient hours of irradiation is up to 18 hours in 95 % of cases, 3.3 % between 18 and 24 hours and 1.7 % over 24 hours. Therefore, the 24-hour storage can only benefit 5 % more timespans without radiation than the 18-hour storage. As a result, the CPC collector field performs just slightly better with a 24-hour storage than with an 18-hour storage and the optima of the collector field is nearly the same.
For example, a CPC collector field with 7000 collectors (20207 kW) with an 18-hour storage achieves a capacity factor of up to 78.92 % and with a 24-hour storage 80.74 %.

In conclusion, it can be stated that in Almeria, the PTC_PTES system achieves the lowest LCOH until a capacity factor of about 89 %.

To also see the space requirements in Almeria, Figure 4-8 plots the annual $Q_{s,tot}$ over the land use for Almeria.

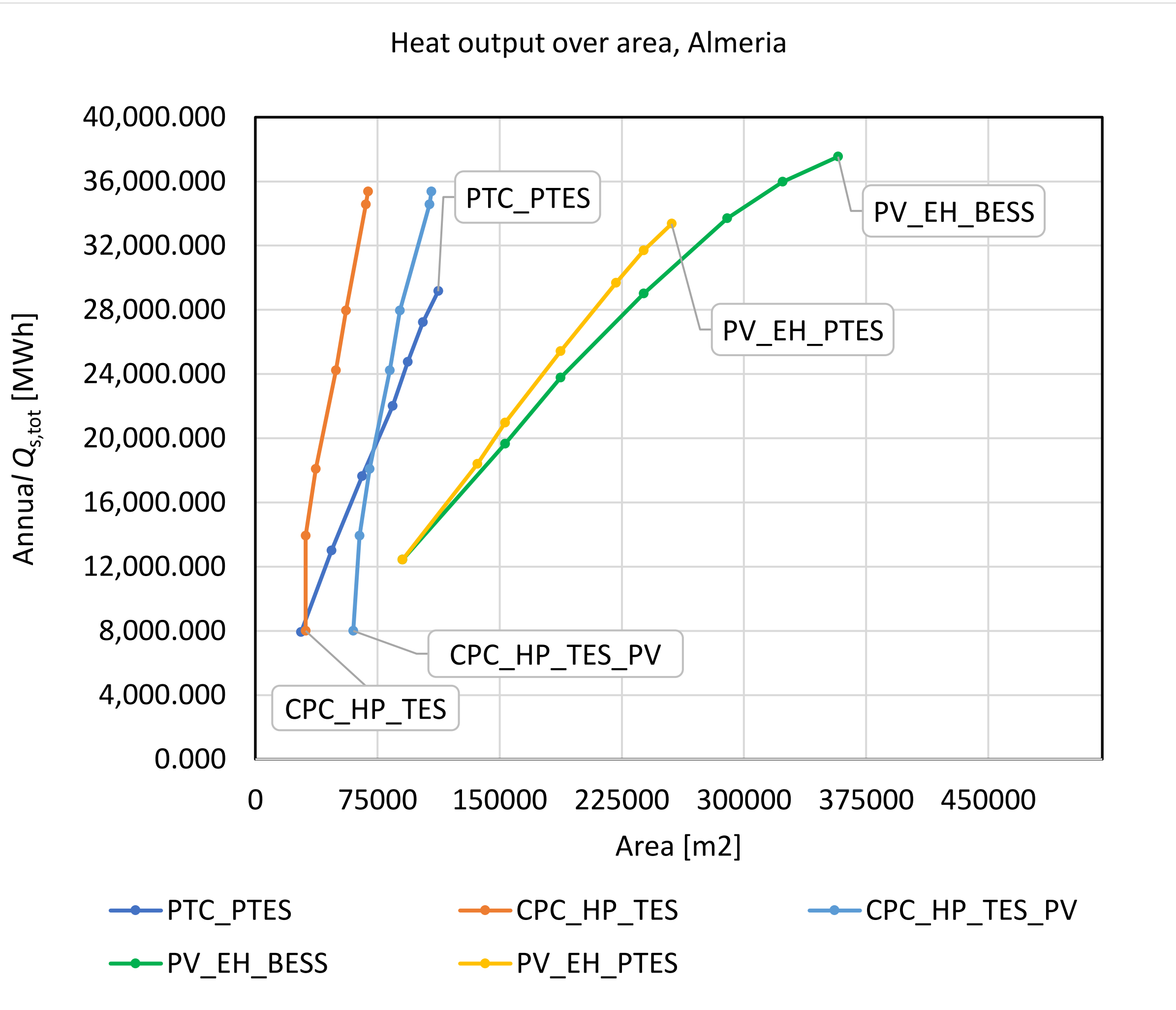

Figure 4-8: Hat output over area, Almeria

The behavior of the curves in relation to one another is the same as in Würzburg. The difference is that in general, the set of curves has a higher $Q_{s,tot}$ and less area consumption. For example, to generate annual 12000 MWh, about 63000 m^2 of the PTC system is needed, while in Würzburg, 84000 m^2 is needed.

For a comparison of both locations, Figure 4-9 plots the LCOH over the capacity factor for Würzburg and Almeria. The results for Almeria are plotted in dashed lines. For a better overview, only the CPC_HP_TES_PV system is plotted.

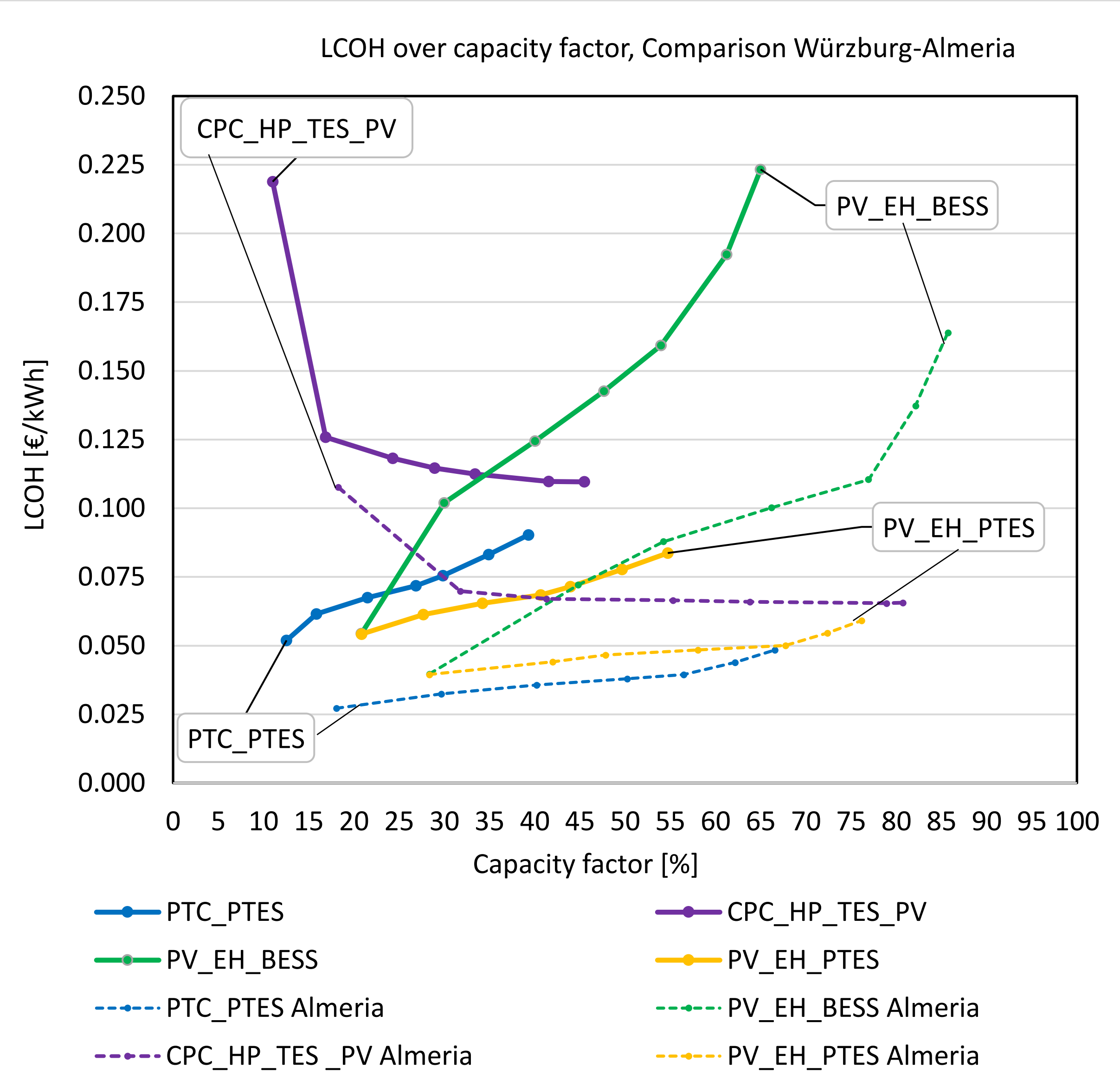

Figure 4-9: System result comparison, minimum LCOH for every storage capacity over capacity factor, Würzburg-Almeria

It can be observed that the dashed curves are shifted to the lower right of the diagram. This gives a good visual confirmation that, in general, the solar technologies perform better in Almeria. It can also be observed that the curves for Almeria have a lower gradient and make higher capacity factor jumps between the storage capacities. Therefore, the storages in Almeria are more utilized.

In conclusion, as the higher radiation levels let one suspect, the solar technologies perform better in Almeria. The PTC_PTES system performs better in Almeria due to the higher direct irradiation. However, in both locations, the PV systems can reach the highest capacity factors.

In the following, the results of this work are compared to results from other literature to see if they are similar or significantly different.

Saini et al. present a study comparing the performance of a PTC field with PTES at 140 °C with a heat pump. One calculated scenario has a constant heat demand of 500 kW steam at 140 °C. The feed water has 110 °C. The heat pump uses wastewater at 40 °C as a heat source. Therefore, the temperature lift is 100 K, and the COP is set to 2.5. The heat pump investment costs are varied from 500-1500 €/kW, and the electricity price from 0.07-0.15 €/kWh. The PTC investment costs are assumed at 350 €/m^2. The system uses a PTES with water as a medium to store energy. The HTF of the PTC is pressurized water. The steam is generated in a separate steam circuit. The results for LOCH over capacity factor are shown for Seville-Spain (DNI 1848 kWh/m^2) and Czech-Prague (DNI 708 kWh/m^2). (cf. Saini et al. 2023, pp. 2–9)

In Spain, the LCOH of the PTC is about 0.03 €/kWh at a capacity factor of 20 % and 0.05 €/kWh at a capacity factor of 45 %. In this thesis, the costs for the PTC in Almeria are 0.0273 €/kWh at a capacity factor of 20 % and 0.037 €/kWh at a capacity factor of 45 %. For low capacity factors, the results in this thesis are about 10 % lower. This could be reasoned with the lower investment (300 €/m^2) cost of the PTC in this thesis. At higher capacity factors, the LCOH differs more strongly. For example, at a capacity factor of 45 %, the LCOH in this thesis is 26 % lower. In the study of Saini et. al. no specific investment costs of the storage are listed. However, the temperature lift in the storage is calculated with 20 K, compared to the 80 K in this thesis. Therefore, the storage might be more expensive, which would explain the LCOH difference at a higher capacity factor. The study and this thesis have in common that the LCOH increase with the integration of a storage. (cf. Saini et al. 2023, p. 12)

For Germany, no explicit calculations are made. However, in another calculation, the LCOH is plotted over the DNI for a capacity factor of 5 %, 25 % and 50 %. At a DNI of 1100 kWh/m^2 and a capacity factor of 5 %, the LOCH is 0.06 €/kWh. For a capacity factor of 25 %, the LCOH is 0.09 €/kWh. A capacity factor of 50 % cannot be achieved with the latter DNI. (cf. Saini et al. 2023, p. 13)
In Germany, in this thesis, the annual DNI is 1135 kWh/m^2. At a capacity factor of 5 %, the LCOH is about 0.057 €/kWh, and at a capacity factor of 25 % the LCOH is about 0.072 €/kWh. Again, at a lower capacity factor, the LCOH only differs in the third decimal place and at a higher capacity factor in the second decimal number, which could be caused by a more expensive storage.

The results for the heat pump are plotted from a range of 0.05 €/kWh to 0.130 €/kWh. The heat pump in this system does not rely on a solar thermal heat source and has lower COP. Thus, it cannot be reasonably compared to the CPC_HP_TES system. However, in Germany, for higher capacity factors than 33 % and for all capacity factors in Spain, the LCOH of this thesis is in the latter range.

Krüger et. al. plots the LCOH over the mean collector temperature for PTC. The calculations are made for a collector field size of 10000 m^2 and a DNI of 1014 kWh/m^2. With an investment cost of 300 €/m^2, the LCOH results in 0.041 €/kWh. (cf. Krüger et al. 2021b, pp. 2–13)
In this thesis, for a field size of about 10000 m^2, the LCOH is 0.061 €/kWh. Although the DNI in this thesis is higher, the LCOH is higher as well. The difference might be caused because of the initial investment cost of the heat exchanger, different land costs and a discount rate of 5% instead of 3 %

In another report, Krüger presented a PV field in combination with an electric heater. The location is Potsdam, but no irradiation data are given. The lowest investment cost for the PV field with the inverter is estimated at 858 €/kW_{AC}, in contrast to 667 €/kW_{AC} in this thesis. The results are for a field size of 9400 m^2. In the report, the PV system achieves a LCOH of 0.54 €/kWh. In this thesis, with an area of 10200 m^2, a LCOH of 0.0598 €/kWh is achieved. The difference could be the result of a discount rate of 5 % instead of 3 % and different land costs. (cf. Krüger 2021, pp. 7–8)
In conclusion, the results of this thesis are similar to the literature for smaller collector field sizes. Differences result from variations in the cost assumption, such as the investment cost.

For higher capacities presented by Saini et al. the LCOH differ more significantly, which could be caused by different storage costs and design. For the CPC_HP_TES system, no comparable literature was found. However, the achieved LCOH lies within the range of the solar independent heat pump system presented by Saini et al.

4.4 Economic competitiveness

For the heat plant owner, the LCOH and capacity factor of the system might not be the only data of interest. The system configuration with the most profit is interesting from an economic standpoint. Another configuration of interest might be the highest achievable capacity factor while not making losses. The latter can be interesting if a company wants a certain image or can advertise a product that is more environmentally friendly without having extra costs. In some cases, it might be even more profitable to pay more energy costs to generate more profit with an environmentally friendly product. However, in the following diagrams, the latter case is not further discussed due to the individuality of the case.

In the following discussion, it is assumed that the solar systems have to compete with an installed boiler with an efficiency of 90 %. The cost per kWh_{th} is calculated with the gas price divided by the boiler efficiency, a surcharge of 19 % for network fees, a surcharge of 7 % for taxes and a surcharge of 0.006 €/kWh for CO_2 taxes (Azteq 2023). This is assumed for Almeria and Würzburg.

Figure 4-10 shows the saved cost per year over the capacity factor in Würzburg. The gas price is assumed with 11 ct/kWh and 5 ct/kWh, as it was in October 2022 and March 2023, respectively (Bundesnetzagentur 2022). The heat generating costs of the boiler, with the assumptions of this chapter, result in 0.1616 €/kWh and 0.07874 €/kWh.
The curves are calculated with the optimal LCOH for the corresponding capacity factor. The optimal LOCH for each capacity factor of the presented systems in Würzburg is plotted in Figure A-0-5.

The CPC_HP_TES system is only plotted for the gas price of 0.11 €/kWh because the system doesn’t achieve a LCOH of 0.07874 €/kWh.

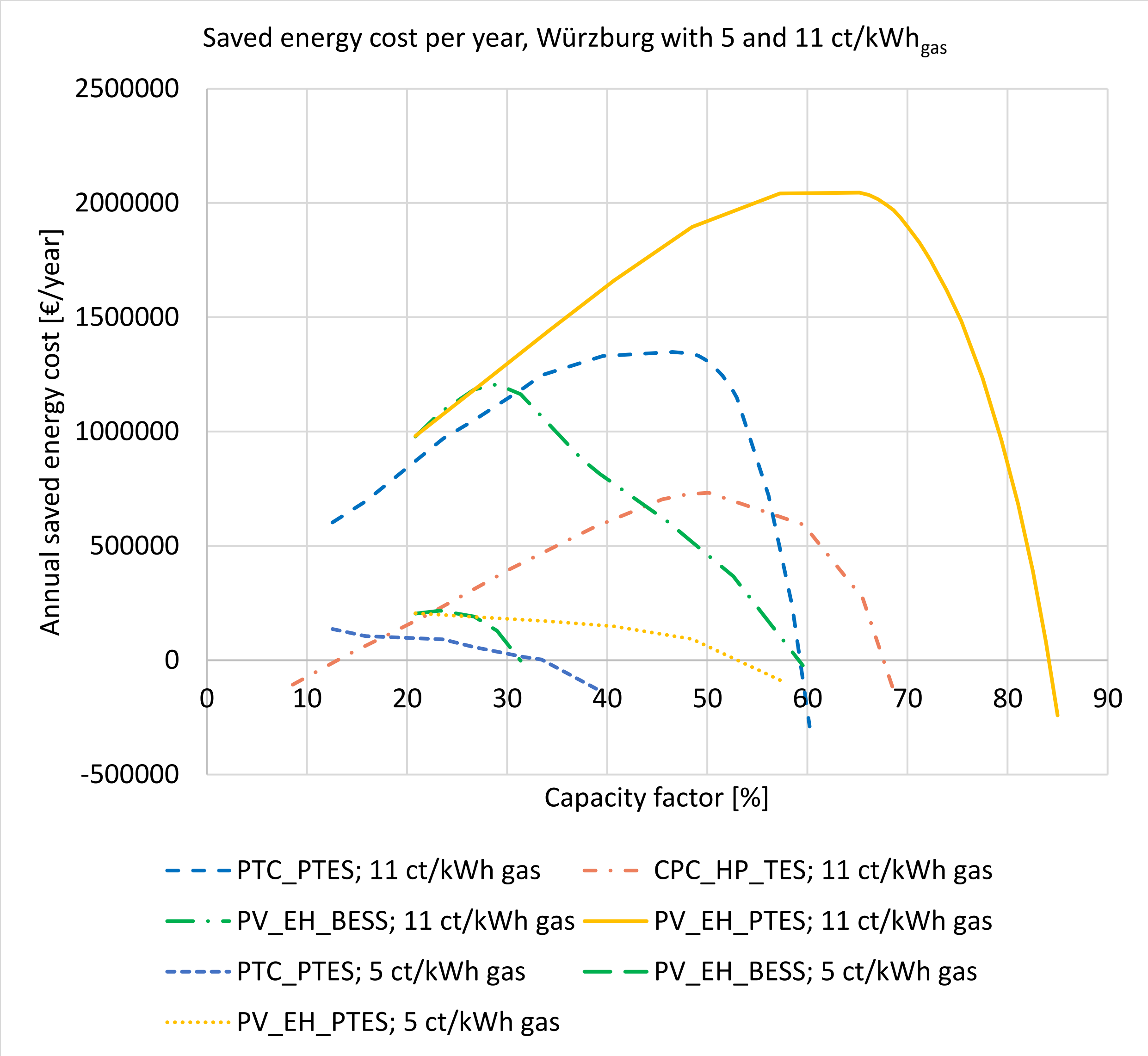

Figure 4-10: Saved heat cost per year. Würzburg with heat generation costs of the boiler of 0.07874 €/kWh (5 ct/kWh$_{gas}$) and 0.1616 €/kWh (11 ct/kWh$_{gas}$)

The positive values represent profit, and the negative values represent additional energy costs per year. The results are plotted until the systems reach a LCOH of 0.1616 €/kWh and 0.07874 €/kWh.

The CPC_HP_TES_PV system is the only one with negative costs at low capacity factors for a gas price of 0.11 €/kWh because of the unique trend of the LCOH curve for the CPC_HP_TES_PV system. At a capacity factor of about 13 %, the system reaches an LCOH of 0.1616 €/kWh and becomes profitable.

The curves all have a maximum saved energy cost per year. The behavior of the systems toward each other is explained in 4.1-4.3.

Table 4-4 lists the maxima for gas prices of 0.05 €/kWh and 0.11 €/kWh in Würzburg.

Table 4-4: Economic competitiveness of the solar systems against a gas boiler, Würzburg

	Annual saved cost [€]		Capacity factor [%]	
	0.05 €/kWh$_{gas}$	0.11 €/kWh$_{gas}$	0.05 €/kWh$_{gas}$	0.11 €/kWh$_{gas}$
PTC_PTES	136539	1345580	12.55	47.46
CPC_HP_TES	-	732593	-	50.15
PV_EH_BESS	216937	1207015	23.32	29.00
PV_EH_PTES	216937	2045454	23.32	65.20

For a gas price of 0.11 €/kWh the PV_EH_PTES system reaches the highest saved cost with 2,045,454 € at a capacity factor of 47.46 %. It also reaches the highest capacity factor with 85 % at a LCOH of 0.1616 €/kWh.

Noticeable is the early decrease for the PV_EH_BESS system. This is because of the LCOH increase with the integration of a BESS. The system reaches its highest profit without a BESS, which is accurate for both gas prices.

The difference at the start of the curves of both photovoltaic systems is due to different resolution in that area. Both systems have the same LCOH until the integration of a storage.

With a gas price of 0.05 €/kWh the PV_EH_PTES and PV_EH_BESS systems perform the best without a storage, respectively. They reach saved costs of 216937 € at a capacity factor of 23.32 %.

Comparing both gas price scenarios for the PV_EH_PTES system shows that over the timespan of this thesis, the maximum annual saved cost per year decrease by 89.4 %, and the corresponding capacity factor decreases from 65.2% to 23.32 %.

Figure 4-11 shows the results for the same calculations in Almeria. The gas price is assumed with 0.13 €/kWh and 0.05 €/kWh, as it was in June 2022 and March 2023. (GlobalPetrolPrices.com 2022; Müller 2022). The cost of heat provided by the boiler with the assumptions of this chapter result in 0.1899 €/kWh and 0.07874 €/kWh. The optimal LOCH for each capacity factor of the presented systems in Almeria is plotted in Figure A-0-6.

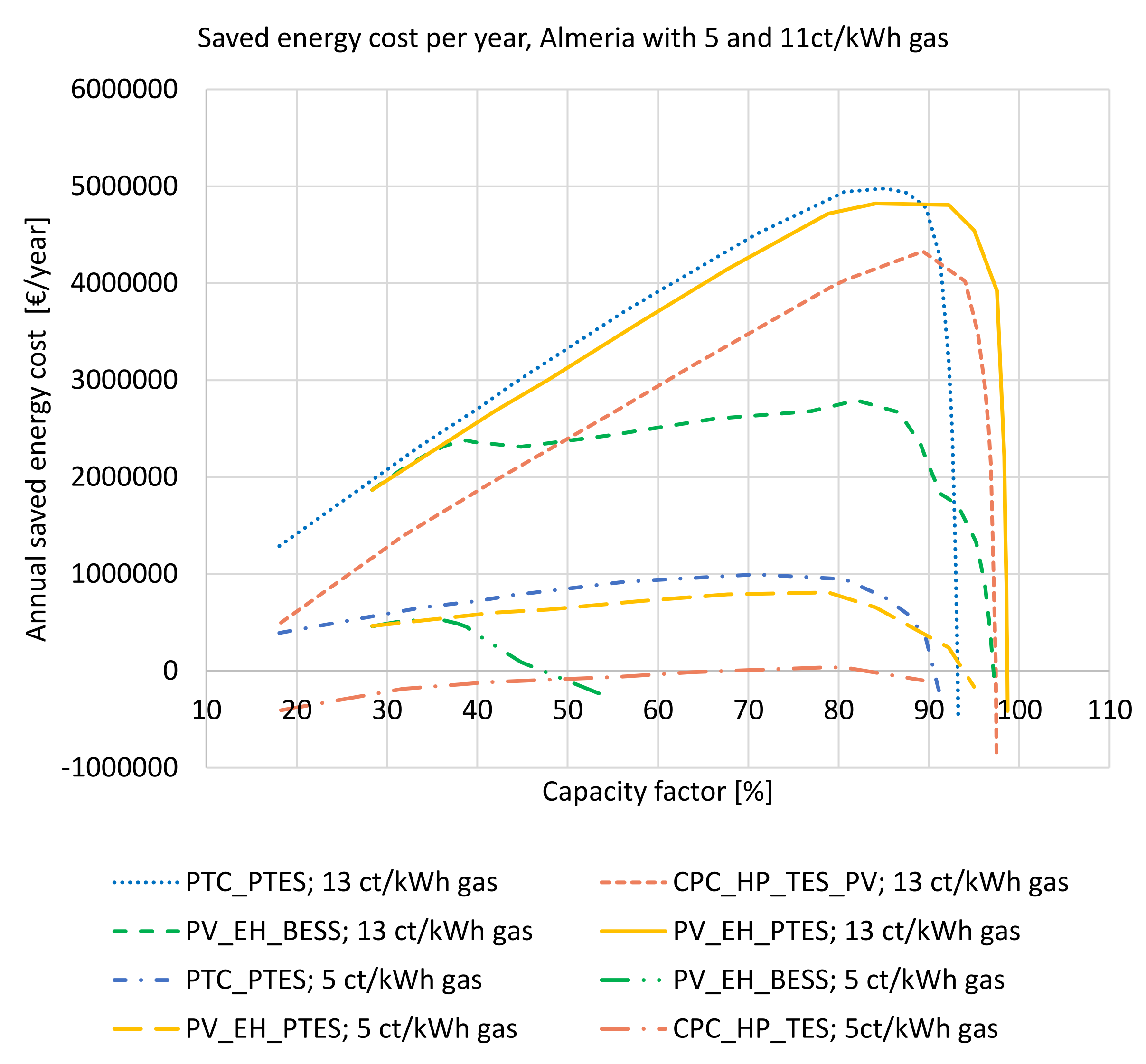

Figure 4-11: Saved heat cost per year. Almeria with heat generation costs of the boiler of 0.07874 €/kWh (5 ct/kWh$_{gas}$) and 0.1899 €/kWh (13 ct/kWh$_{gas}$)

In Almeria, with the assumed gas prices, all systems have positive values.

In contrast to Würzburg, the highest saved cost can be achieved with the PTC_PTES system. However, the highest capacity factor without generating losses can be achieved with the PV_EH_PTES system. Different from Würzburg is that with the PV_EH_BESS system at a gas price of 0.13 €/kWh, the BESS has an economic benefit. Thus, the maximum is at a higher capacity factor.

Table 4-5 lists the maxima for gas prices of 0.05 €/kWh and 0.13 €/kWh in Almeria.

Table 4-5: Economic competitiveness of the solar systems against a gas boiler, Almeria

	Annual saved cost [€]		Capacity factor [%]	
	0.05 €/kWh_{gas}	0.13 €/kWh_{gas}	0.05 €/kWh_{gas}	0.13 €/kWh_{gas}
PTC_PTES	994521	4977787	70.87	85.18
CPC_HP_TES	32661	4328584	80.74	89.31
PV_EH_BESS	216937	1207015	23.32	29.00
PV_EH_PTES	809287	4822584	78.83	84.1

Significant in Almeria is that for a gas price of 0.13 €/kWh, the maximum is shortly before a steep drop op. With the high gas price, the systems generate profit up to high capacity factors and are only capped because of the technical conditions. The steep drop of is because there cannot be generated much more heat. The field size and investment rise without generating additional heat, therefore increasing the LCOH without capacity factor gain.

Comparing both gas price scenarios for the PTC_PTES system shows that over the timespan of this thesis, the maximum annual saved cost per year decrease by 80.02 %, and the corresponding capacity factor decreases from 85.18 % to 70.87 %.

Comparing Almeria and Würzburg shows that the systems in Almeria achieve higher capacity factors with higher saved costs for the scenarios of 2022 and 2023. With a gas price of 0.05 €/kWh in Almeria, the maximum achievable saved costs are 358 % higher with a capacity factor of 70.87 % instead of 23.32 %.

In conclusion, the results for these boundary conditions show that depending on the gas price and the location, solar technologies can compete with fossil-fueled technologies. However, the economic performance depends on the fluctuating gas price development. The calculations for 2022 and 2023 are only about six months apart, but the results differ by up to 90 %. It must be noted that the absolute values differ for other boundary conditions and cannot be transferred to other applications.

The volatile development of energy prices makes a future deduction of the competitiveness of solar technologies challenging.

5 Sensitivity analysis

In this chapter, a cost sensitivity is first carried out for each system. The main investment costs of each system are varied to analyze the impact on the complete system. Then, scenarios with the variation of the most sensitive parameters are shown. Subsequently, the sensibility of the PTC_PTES model, regarding the heat-up, is analyzed. Finally, the influence of the time step length on the PTC_PTES system is analyzed.

5.1 Cost sensitivity

In this chapter, the sensitivity regarding the investment costs of the technologies is analyzed. This analysis is only made for Würzburg, as the procedure would be the same for Almeria. As a mean storage size, nine hours is chosen. For the nine-hour storage size, the minimum LCOH configuration is analyzed. The costs are varied, with 20 % less and 20 % more.

For the PTC_PTES system, the cost of the PTC field and the PTES are varied. The original LCOH is 0.0718 €/kWh. Figure 5-1 plots the LCOH over the investment change.

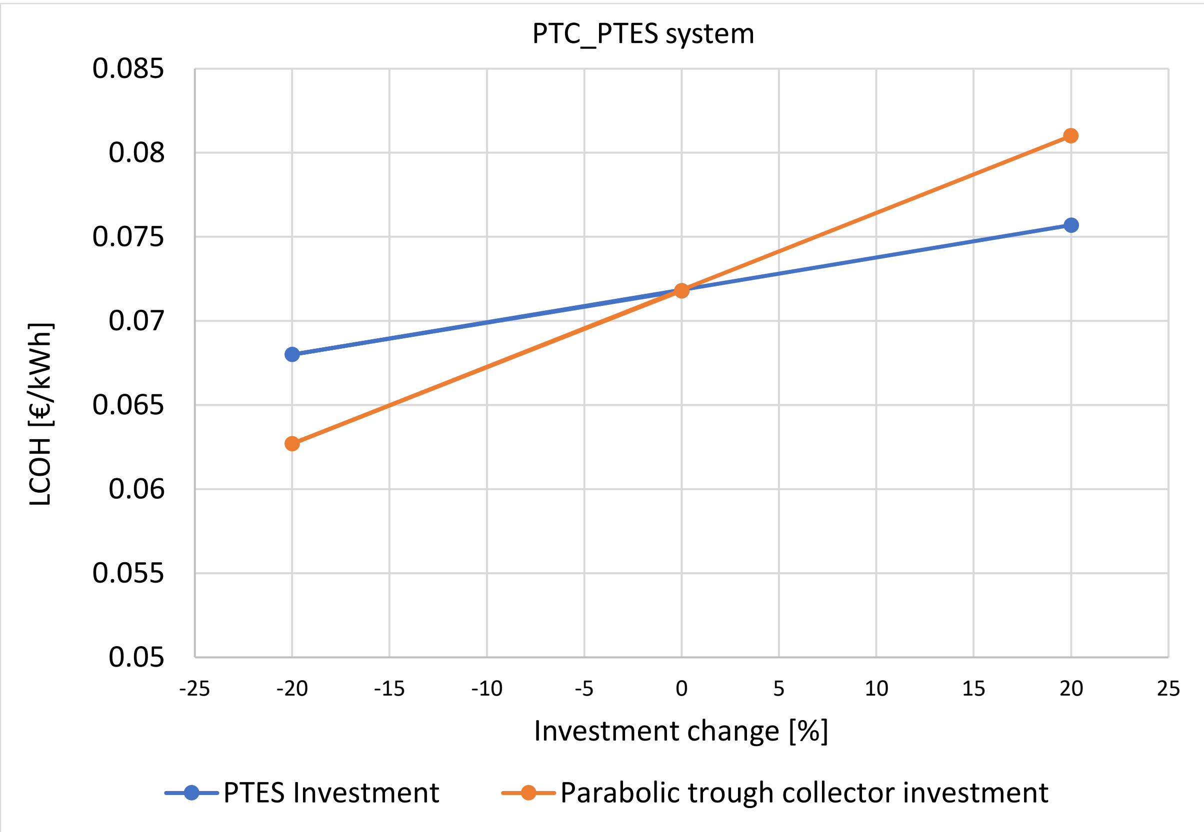

Figure 5-1: Cost sensitivity, PTC_PTES

The gradient of the graph indicates the sensitivity regarding the cost parameter.

The parabolic trough collector investment has the greatest impact. Changing the investment by 20 % leads to a change of 0.0091 €/kWh, which resembles a change of 12.67 % of the system's LCOH. The LCOH change for the PTES is 0.0038 €/kWh, 5.29 % of the complete system

For the CPC_HP_TES system, the cost of the CPC collector field, the TES, the heat pump and the electricity costs are varied. The original LCOH is 0.1351 €/kWh.

Figure 5-2 plots the LCOH over the investment change.

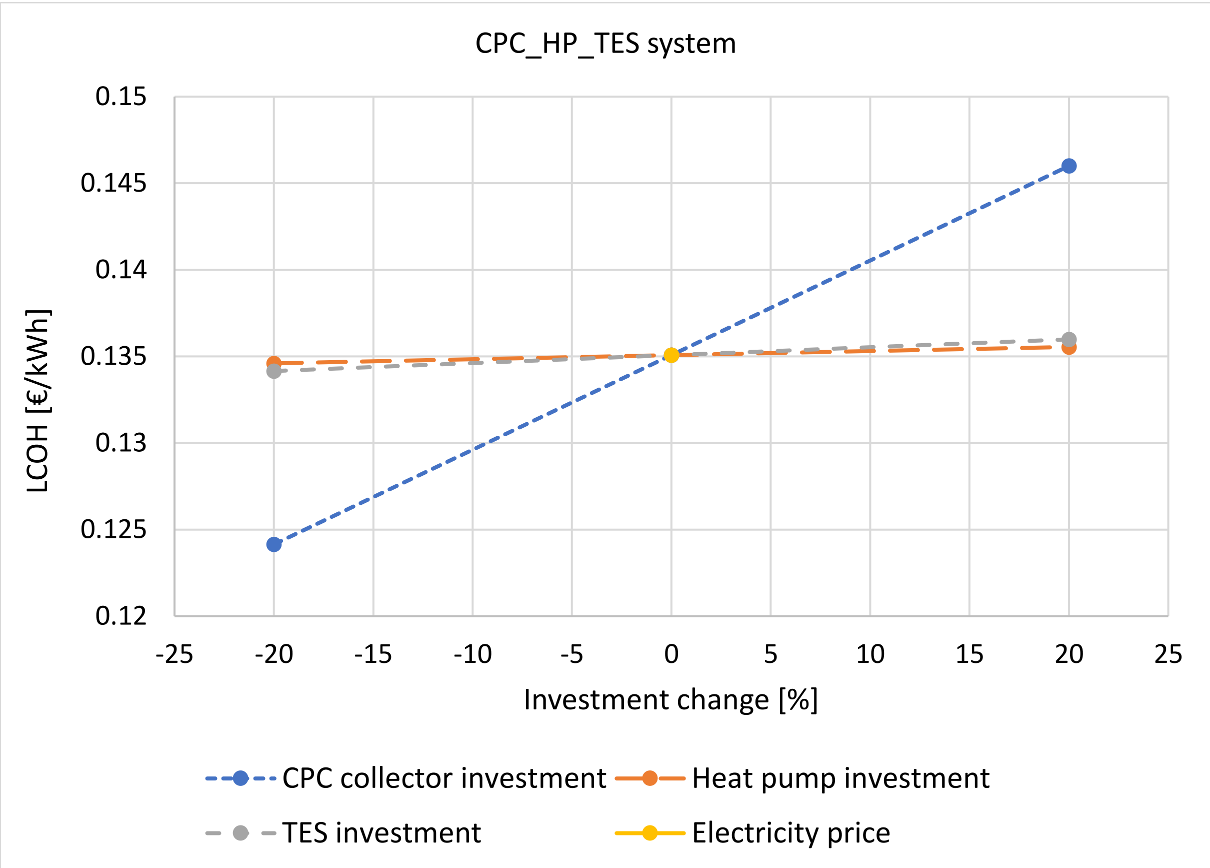

Figure 5-2: Cost sensitivity, CPC_HP_TES

For the CPC_HP system, the cost of the collector is the most sensitive investment parameter. However, varying the electricity costs impacts the system a little more.

The LCOH changes because of the TES and heat pump investment is comparatively low. The heat pump does not scale with the size of the collector field. Thus, the proportion of the complete cost sinks with increasing collector field costs. The TES does not have high investment costs. Therefore, a 20 % change does not have a huge impact on the whole system.

Table 5-1 lists the absolute and relative change of the LCOH for the changed parameters of the CPC_HP_TES system.

Table 5-1: Cost sensitivity, cost change of 20 %, CPC_HP_TES

	CPC collector investment	TES investment	Heat pump investment	Electricity costs
LCOH change [€/kWh]	0.01093 (8.09 %)	0.0009148 (0.7 %)	0.0004733 (0.4 %)	0.01174 (8.69 %)

For the PV_EH_BESS system, the cost of the PV field, the BESS and the Electric heater are varied. The original LCOH is 0.1426 €/kWh.
Figure 5-3 plots the LCOH over the investment change for the PV_EH_BESS system.

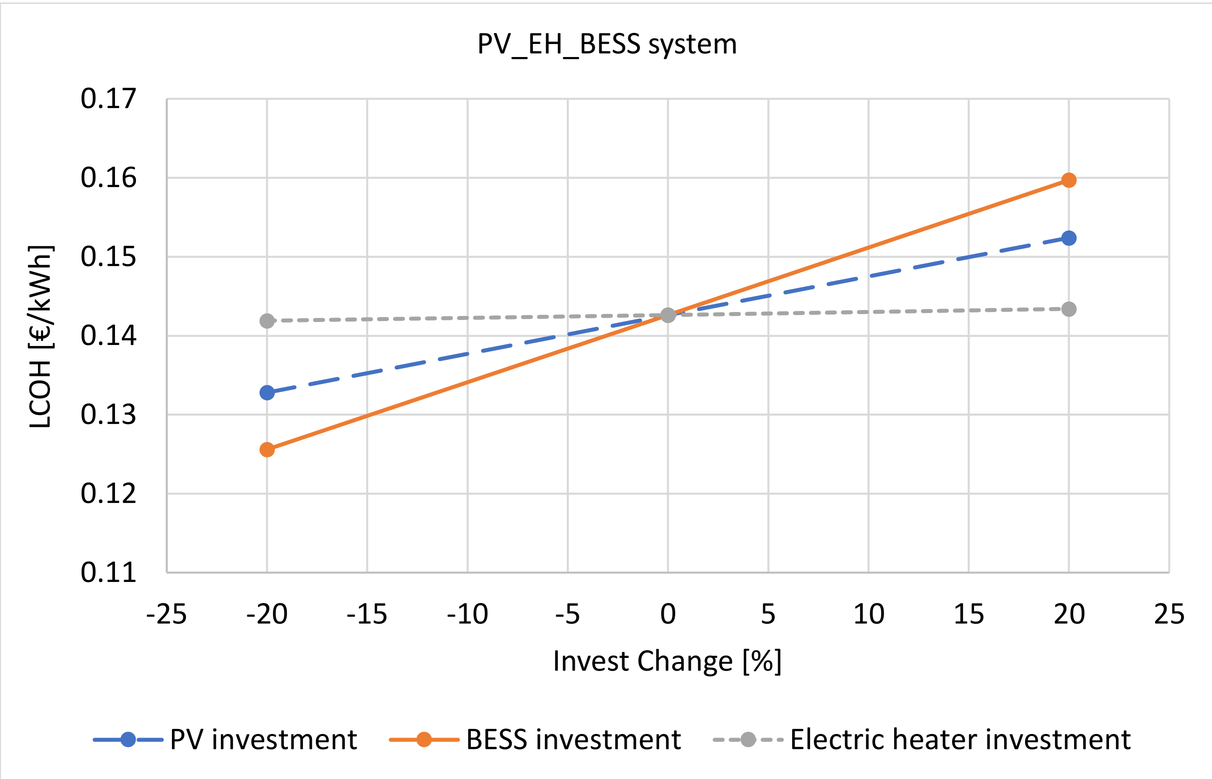

Figure 5-3: Cost sensitivity, CPC_HP_TES

Table 5-2 lists the absolute and relative change of the LCOH for the changed parameters of the PV_EH_BESS system. The BESS investment is the most sensitive parameter. The absolute value in Table 5-2 shows that the investments of the BESS are high compared to those of the

TES/PTES. The electric heater investment hardly affects the system because it doesn't scale with the PV field size.

Table 5-2: Cost sensitivity, cost change of 20 %, PV_EH_BESS

	PV investment	BESS investment	Electric heater investment
LCOH change [€/kWh]	0.0093 (6.86 %)	0.0162 (11.96 %)	0.0007 (0.52 %)

For the PV_EH_PTES system, the cost of the PV field, the PTES and the Electric heater are varied. The original LCOH is 0.0684 €/kWh.

Figure 5-4 plots the LCOH over the investment change.

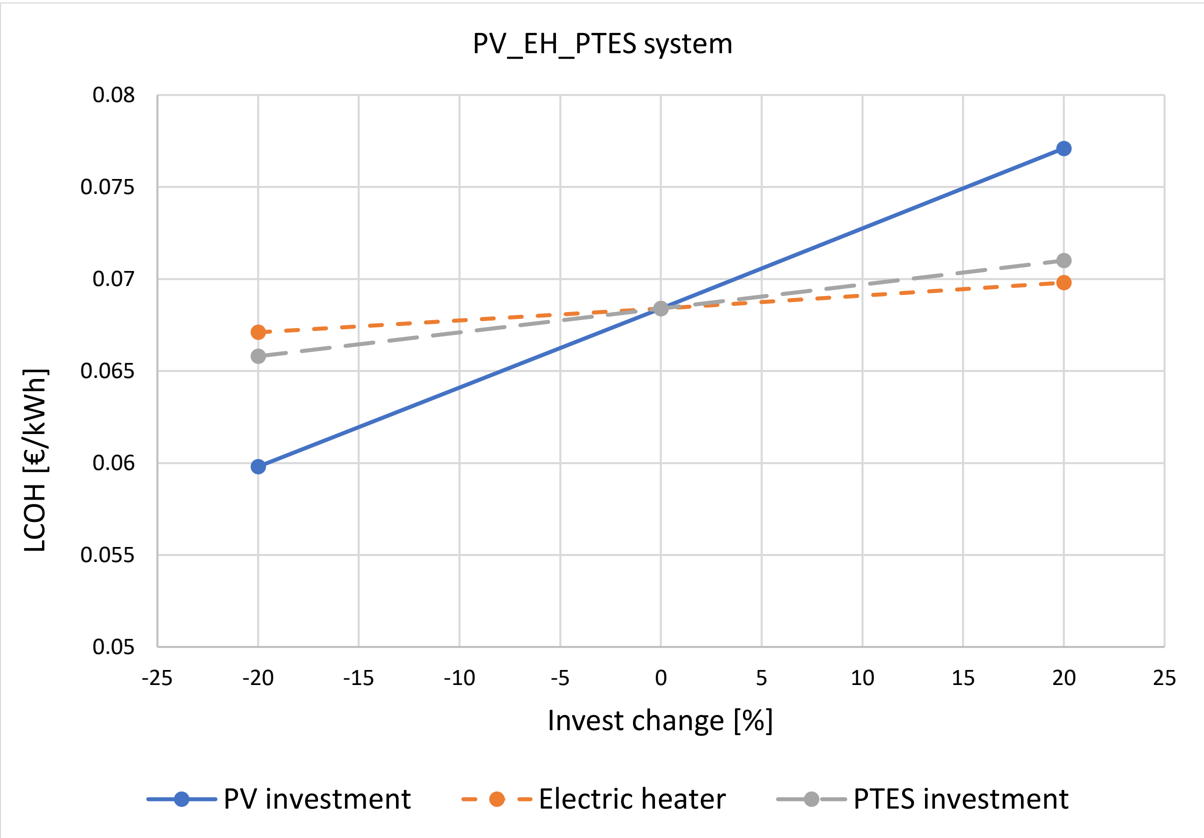

Figure 5-4: Cost sensitivity, PV_EH_PTES

The PV investment presents the most significant impact. Again, this shows the difference between the BESS and PTES. The electric heater has more impact on the PV_EH_PTES system because the nominal power scales with the PV field. Table 5-3 shows the LCOH change caused by the investment change of 20%.

Table 5-3: Cost sensitivity, cost change of 20 %, PV_EH_PTES

	PV investment	PTES investment	Electric heater investment
LCOH change [€/kWh]	0.0086 (12.57 %)	0.0013 (1.9 %)	0.0026 (3.8 %)

In conclusion, with a 20 % investment change for the described boundary conditions, the following specific investment costs are the most sensitive:

- PTC_PTES: PTC investment,
- CPC_HP_TES: CPC collector investment,
- PV_EH_BESS: BESS investment and
- PV_EH_PTES: PV field investment.

Based on the calculated sensitivities, the same systems are calculated with different investment costs. Only the most sensitive parameter is varied so as not to deviate too much from the original boundary conditions.

In Würzburg, only the relation between PV_EH_PTES and PTC_PTES system is analyzed because the other systems have too high LCOH values to become competitive with an investment change of 20 %.

Figure 5-5 shows PTC_PTES & PV_EH_PTES systems with a ±20 % change of the most sensitive investment cost. The upper curve represents the values for a + 20 % change, and accordingly, the lower curve represents the values for a -20 % change. The LCOH is plotted for the same capacity factors as in Figure 4-5, to stay comparable.

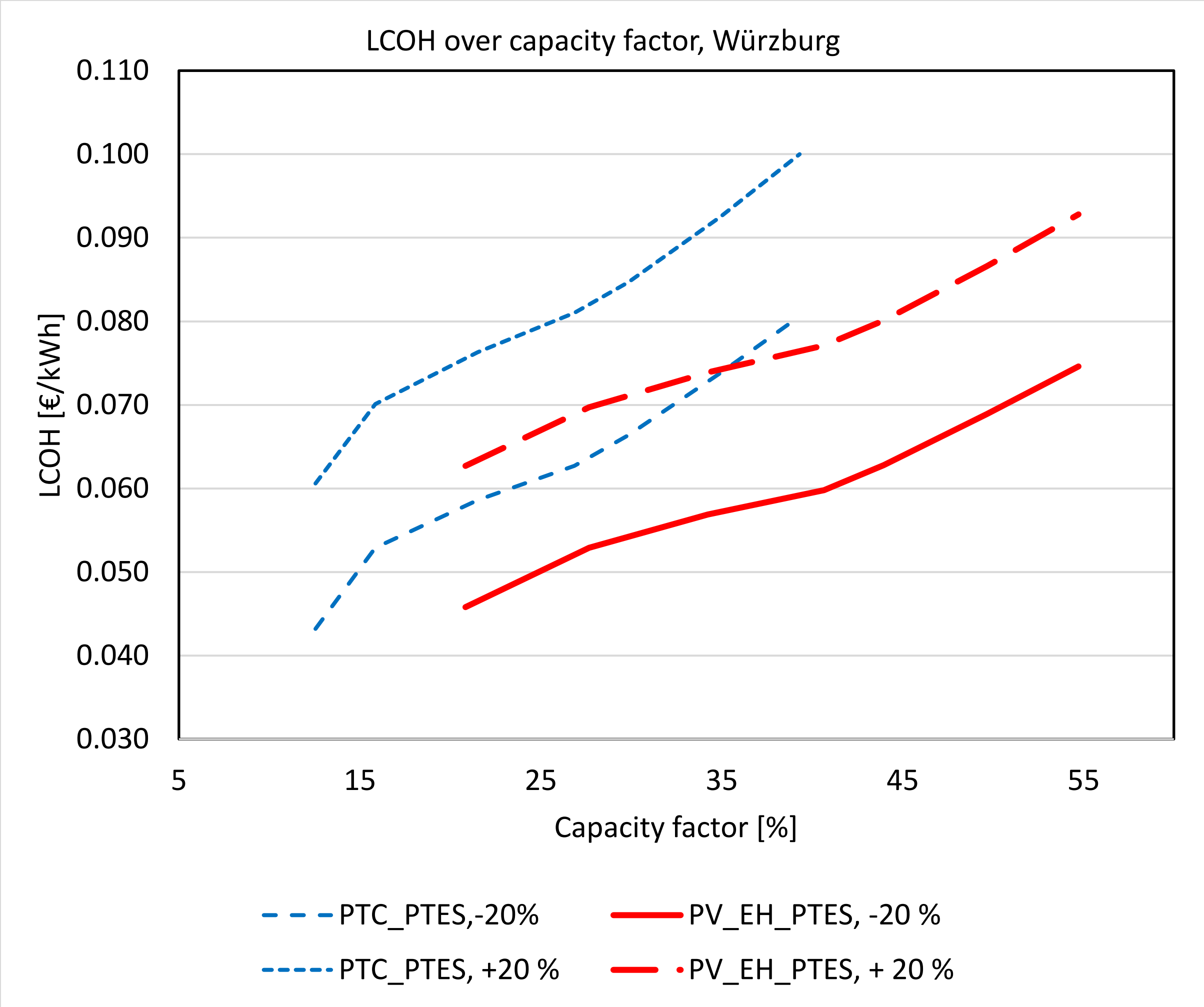

Figure 5-5: Sensitivity analysis in Würzburg with ±20 % investment cost change for the most sensitive investment cost parameter

One scenario could be that PV field prices rise due to high demand, and the PTC cost sink due to more know-how and mass manufacturing. Comparing the -20 % curve of the PTC_PTES system and the +20 % curve of the PV_EH_PTES shows that in such a scenario, the PTC_PTES system has a lower LCOH up until a capacity factor of about 35 %. Still, with these cost variations, the PV_EH_PTES system achieves lower LCOH at high capacity factors.

Comparing the +20 % of the PTC_PTES system and the -20 % PV_EH_PTES shows that in such a scenario the PV_EH_PTES system would have the lowest LCOH for all capacity factors.

The LCOH values from the -20 % investment costs are also interesting. The lowest LCOH for the PTC_PTES system is 0.0432 €/kWh with a capacity factor of 12.55 %. The lowest LCOH for the PV_EH_PTES system is 0.0458 €/kWh with a capacity factor of 20.84 %. These LCOH are lower than the gas price of March 2023. Thus, the systems would have an economic benefit as opposed to the systems with no cost reduction.

The same analysis is made for Almeria. However, in Almeria, the CPC_HP_TES_PV system is considered with a -20 % cost variation, as the LCOH in Almeria is closer to the other systems. Figure 5-5 shows the systems with a ±20 % change of the most sensitive investment cost.

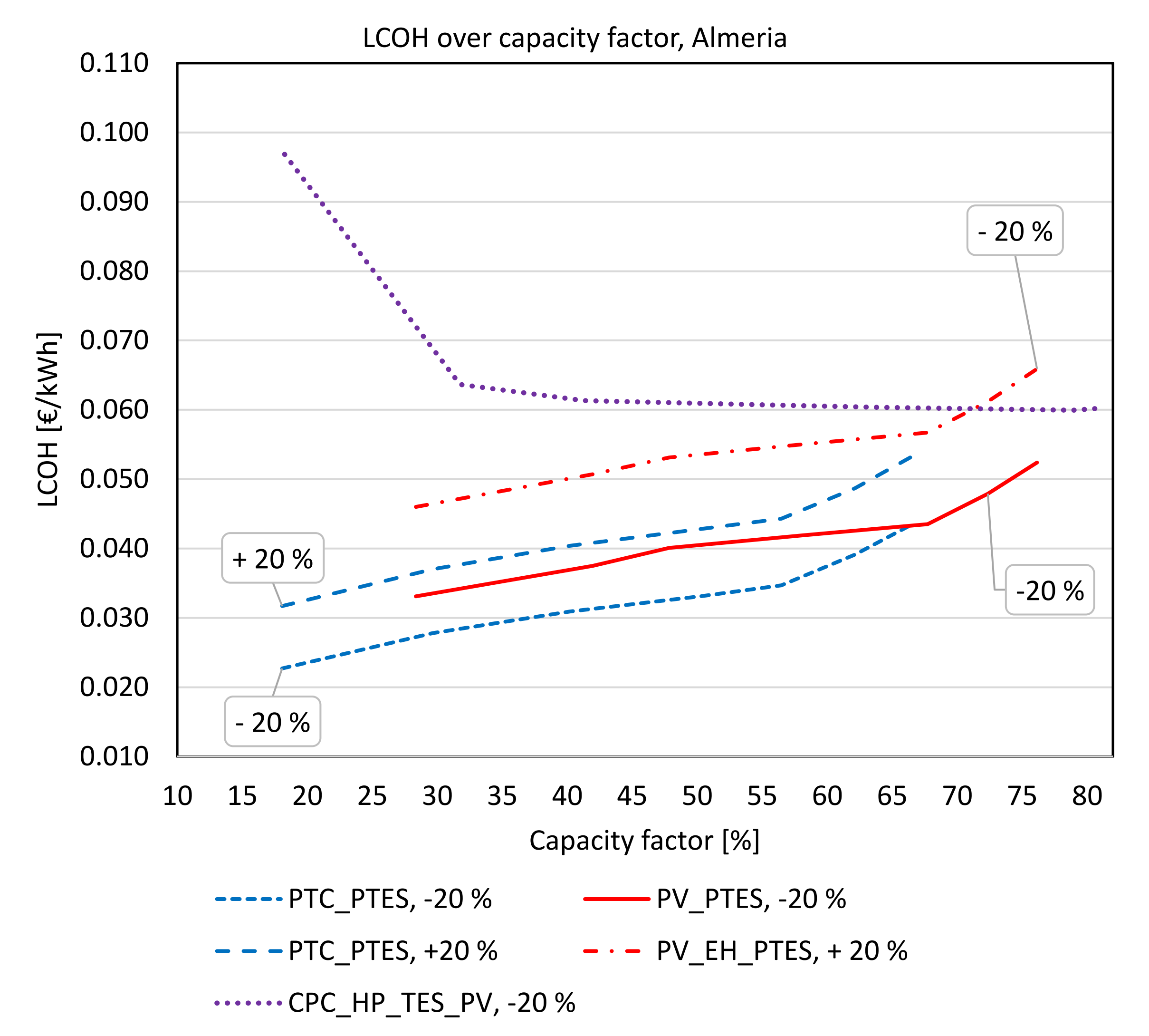

Figure 5-6: Sensitivity analysis in Almeria with ± 20 % investment cost change for the most sensitive investment cost parameter

In Almeria, the PTC_PTES system achieves lower LCOH than the PV_EH_PTES system.
If the PV_EH_PTES system has 20 % lower PV field cost and the PTC_PTES system has 20 % higher PTC cost, the PV_EH_PTES system would achieve lower LCOH for all capacity factors.

The CPC_HP_TES_PV system with the 20 % lower CPC collector cost achieves lower LCOH than the PV_EH_PTES system with a cost increase above a capacity factor 70 %. However, also with these cost changes, the CPC_HP_TES_PV system cannot achieve the lowest LCOH.

With the -20 % cost variation, the PTC_PTES would achieve a capacity factor of about 85 % at a LCOH of 0.05 €/kWh. The PV_EH_PTES system would achieve a capacity factor at about 74 %.

Based on Figure 5-5 and Figure 5-6 one can say that with a 20 % cost variation, the PTC_PTES and PV_EH_PTES system both have scenarios where one has lower LCOH than the other. The PV_EH_BESS and the CPC systems cannot achieve the lowest LCOH with these cost variations.

5.2 Heat-up factor

For the PTC_PTES system, the heat-up in greenius is simulated with a constant temperature for the collector field, and piping. However, the collector, the HTF and the piping have a different specific heating capacity. The system's mean temperature has to reach 170 °C for the system to generate heat.

Therefore, this calculation is simplified. For example, temperature gradients within the system while heating up are not considered or additional boundary conditions such as hold times or temperature gradient limitations. (cf. Hirsch et al. 2012, p. 1) The study of Hirsch et. al. explains and researches aspects of the heat-up.

To further investigate these impacts, a factor δ is introduced to analyze to which extent the heat-up has an effect on the system. Hirsch et al. researched a factor of 1.3, 1.5 and 1.7. However, mentions that these factors are dependent on the individual power plant. The default factor for the ideal system in this thesis is one. The factor 1.3 is for good irradiation conditions, the factor 1.5 is for mean irradiation conditions and 1.7 is for bad irradiation conditions. (cf. Hirsch et al. 2012, p. 6) A brief calculation showed that the given values resemble realistic parameters for the relevant system. Due to the extent of this thesis, one factor is used for the whole year. To further improve the results of this sensibility research, a factor for each day could be determined. The parameter δ is multiplied onto the needed heat for the heat-up process.

Figure 5-7 shows the LCOH over the capacity factor for the PTC_PTES system with the different scaling factors for Würzburg.

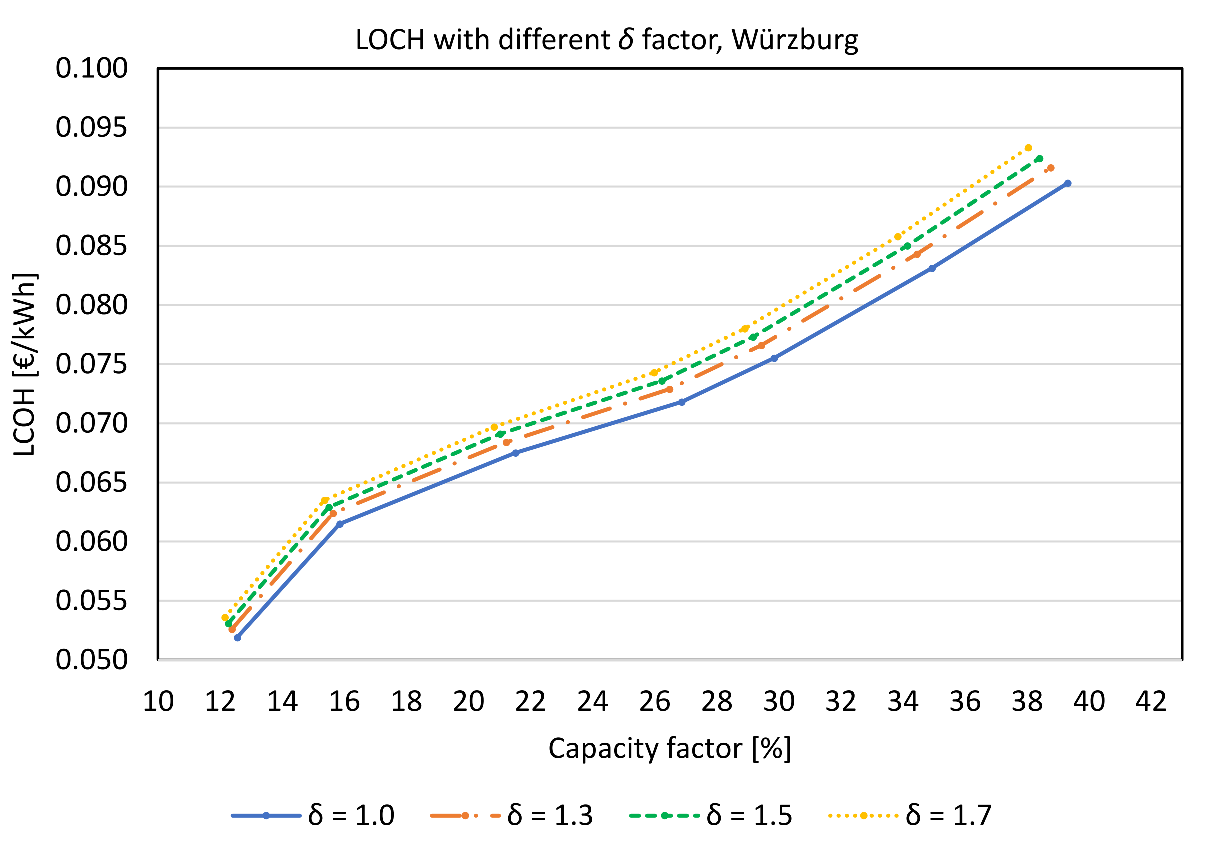

Figure 5-7: Heat-up with scaling factor δ

The Graph shows that, as one expects, the introduction of the factor leads to a loss of $Q_{s,tot}$, thus increasing the LCOH.

Table 5-4 shows the hours with irradiation for the 11th of December of the reference year. The simulation is made for six rows and has no storage. The heat output $Q_{out,PTC}$ and the mean HTF temperature T F mean are tabled for δ=1 and δ=1.7.

Table 5-4: Influence of δ factor

		δ=1		δ=1.7	
Time	DNI [W/m^2]	$Q_{out,PTC}$ [MW]	$T_{F,mean}$ [°C]	$Q_{out,PTC}$[MW]	$T_{F,mean}$ [°C]
9:00	0	0	20	0	20
10:00	328	0	115.13	0	76.83
11:00	373	0.39	170	0	128.44
12:00	101	0	167.68	0	129.65
13:00	518	0.41	170	0	150.36
14:00	212	0.358	170	0	166.36
15:00	0	0	156.04	0	152.8

The irradiation of the day is comparatively low. However, at δ=1 the system generates heat. With the integration of the δ factor of 1.7, the collector does not reach the operating temperature, and thus doesn't generate heat.

Table 5-5 lists the relative reduction of $Q_{s,tot}$, caused by the δ factor. The results of each δ factor are averaged for all capacity factors.

Table 5-5: Relative additional heat losses with heat-up scaling factor δ

	$Q_{s,tot}$ loss	
δ	Würzburg	Almeria
1.3	1.43 %	0.84 %
1.5	2.35 %	1.45 %
1.7	3.31 %	1.99 %

The reduced heat scales proportionally with δ. The losses for Würzburg are higher than for Almeria. The reason is that the heat-up energy is proportionally less in Almeria than in Würzburg. For example, the heat-up heat for a system with no storage and 12 rows is 3 % of $Q_{s,tot}$ in Almeria and 5 % in Würzburg.

To sum it up, the overall calculations and the sample day show, that the ideal system does generate more heat than with the δ factor. Therefore, such a factor can make the simulation of the heat-up more realistic.

5.3 Time step influence

The time step of the weather data in this thesis is in an hour step resolution. Accordingly, the simulations of this thesis are calculated with 60-minute timesteps.

The solar radiation in the weather data is averaged to hourly values. With hourly weather values, the weather data over an hour are averaged into one value. Therefore, short time shading due to clouds is averaged out. For thermal collectors, the short-term shadowing could have negative effects, for example, regarding the heat-up of the system. In order to evaluate the influence of the timestep, for example, for the latter situation, two timestep lengths, ten minutes and 60 minutes, are compared.

Because no matching ten-minute time step weather data for Würzburg or Almeria for the 60-minute time step data are available, this analysis was performed using weather data for Jülich, Germany. The ten-minute timestep data are provided by the DLR (DLR 2022b). To calculate the 60-minute timestep data, the ten-minute timestep data are averaged to 60-minute timestep data. Therefore, the annual sum of the solar radiation is identical.

The comparison is made for the PTC_PTES system. The storage capacity is varied up to 24 hours, and the lowest LCOH of each storage capacity is depicted.

In Figure 5-8 the LCOH with the corresponding capacity factor is portrayed. The minimum for each storage capacity is plotted. The graphs for the ten-minute and 60-minute time steps are shown.

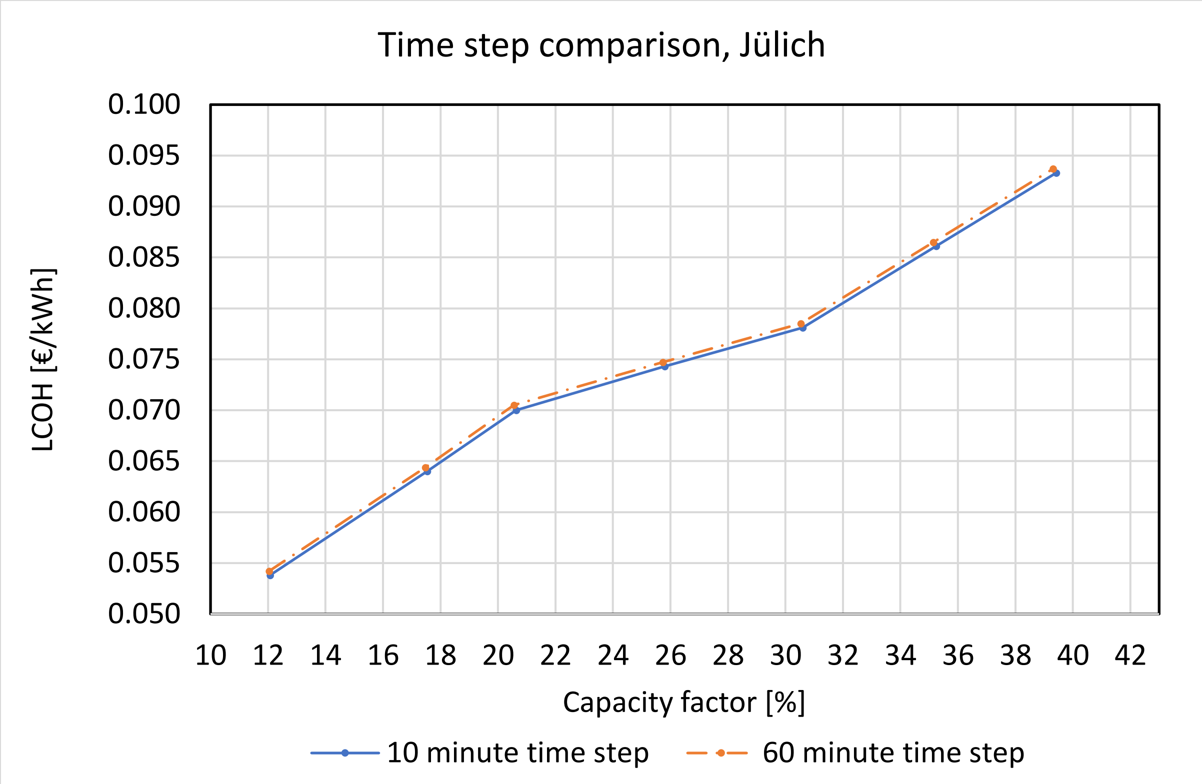

Figure 5-8: Results of the time step comparison

The graphs are visibly close together and show the same behavior. The LCOH for the 60-minute time is 1 % higher for every storage capacity.

In Table 5-6 the values of the 12th of July are listed. The DNI and $T_{F,mean}$ are listed. The DNI value of the 60-min time step is the average value of the last hour. For example, the value 75 W/m^2 in the 60-minute time step is the averaged value from 5:10-6:00. The table shows that in reality, the sun rises at 5:20, and thus no radiation is available from 5:00-5:20. The difference for the 60-minute time step is that the complete time span is simulated with an averaged, thus lower, DNI of 75 W/m^2, therefore simulating as if there is radiation from 5:00-5:20. The resulting effect, can be observed on T F mean. Both temperatures are similar at 5:00 and only differ by 0.36 °C. The next comparison of the temperatures can be made at 6:00. The difference now is 6.16 °C. Thus, the system faster heats up with a higher DNI over a short time rather than an averaged DNI over a longer time.

Table 5-6: Heat-up hour. 10 min vs 60 min time step

	DNI [W/m²]		$T_{F,mean}$ [°C]	
	10 min. time step	60 min. time step	10 min. time step	60 min. time step
05:00	0	0	77.56	77.2
05:10	0		76.86	
05:20	1		76.19	
05:30	41		77.02	
05:40	130		82.27	
05:50	128		88.52	
06:00	152	75	97.39	91.23
	Average 5:10-6:00: 75.3			

Two hours are listed to see the behavior at operating hours. Table 5-7 shows two hours of the summer day, the 11th July. In both hours, the system is at operating temperature. To rule out rounding inaccuracies, two hours are chosen in which the DNI is once rounded up and down.

Table 5-7: Heat output behavior. 10 min vs 60 min time step

	DNI[W/m²]		$\dot{Q}_{out,PTC}$ [MW]		$T_{F,mean}$ [°C]	
	10 min. time step	60 min. time step	10 min. time step	60 min. time step	10 min. time step	60 min. time step
12:10	396		7.078		170	
12:20	4		0		168.51	
12:30	740		13.179		170	
12:40	382		6.769		170	
12:50	770		13.992		170	
13:00	731		13.282		170	170
Average	503.83333	504	9.05	9.043	-	-
13:10	225		3.864		170	
13:20	386		6.893		170	
13:30	389		6.982		170	
13:40	3		0		168.45	
13:50	133		1.916		170	
14:00	0		0		168.13	170
Average	189.33333	189	3.27583	3.228	-	-

Firstly, the short time shadowing is captured in the 10-minute time step. This leads to short times without heat output and a cool down of the collector field. However, it can be observed that the heat output of the solar field Q out for both hours is higher for the 10-minute time step. Therefore, the averaging of the DNI has the same effect at operating temperature as it does at heat-up.

These results can be justified by the calculation of the PTC collector. As described in chapter 2.3, the equation for the efficiency of parabolic trough collectors depends on the DNI. A higher DNI results in a higher efficiency.
Thus, the interpretation based on the equation is that the DNI for both time steps is identical but is converted with a higher efficiency for the 10-minute time step data.

Another effect is that with the 10-minute time step, more heat has to be dumped. Figure 5-9 shows a sketch of the heat demand, the averaged 60 min value, and the 10-min value.

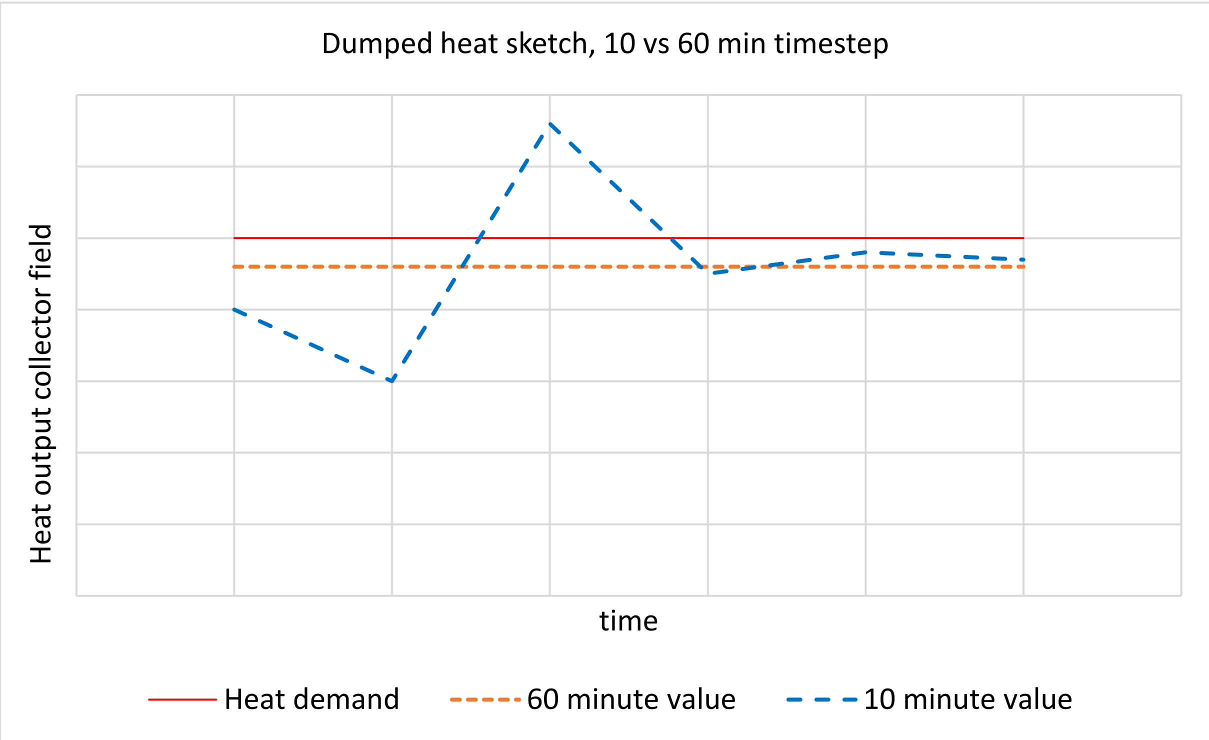

Figure 5-9: Sketch of dumped heat with 10- and 60-minute time step

The figure shows that the generated heat with the 10-minute time step exceeds the heat demand for a short time. The averaged value for the 60-minute timestep is constantly below the heat demand. Thus, the same heat is generated, but with the 10-minute time step, heat has to be dumped. For example, a system with four PTC rows and no storage dumps 114 MWh annually with the 10-minute time step and 104 MWh with a 60-minute time step.
However, for the 10-minute timestep, the additional generated heat outweighs the additional dumped heat at the minimum LCOH, and the minimum LCOH decreases.

6 Summary and conclusion

During the current climate crisis, we are facing problems such as extreme weather conditions and health issues due to rising CO_2 levels. There are several approaches to reduce CO_2 emissions and help solve the climate crisis. One approach is the generation of energy with renewable technologies. In the German industrial sector, renewable technologies supply negligible process heat.

To estimate the potential of renewable technologies in this sector, the techno-economic performance of solar-powered heat generation systems on an industrial scale at a temperature level of 130 °C is evaluated in this thesis.

At first, a literature and market research are carried out to identify suitable industries.

The two most suitable industries are the food, beverages, and tobacco and the paper, pulp, and printing industry. A specific example is the pasteurization and sterilization in the dairy industry, which has a constant heat demand, leading to higher utilization of solar technologies. Based on this research, the boundary conditions for an example industry are defined. The heat demand is assumed as constant at 5 MW over the whole year. The heat is supplied as saturated steam at 130 °C, and the return temperature is 80 °C. In order to calculate the effect of different solar radiation, the simulations are carried out for Würzburg in Germany and Almeria in Spain.

Four systems are modeled and simulated. The heat generating systems are mainly compared with regard to the levelized cost of heat (LCOH) and capacity factor. For the simulations, the software greenius, Excel and EBSIOLN Professional are used.

The first system (PTC_PTES) has a parabolic trough collector (PTC) as the collector type. A pressurized thermal energy storage system (PTES), with water as the storage medium, is integrated to increase the solar capacity factor. The PTC field heats pressurized water to 210 °C because this allows the cheapest storage solution to be achieved. The pressurized water transfers the heat in a heat exchanger to evaporate the water on the consumer side.

The second system (CPC_HP_TES) has a compound parabolic concentrator CPC collector as the collector type. However, in this system, the collector field heats water up to 95 °C. A pressureless thermal energy storage system (TES) stores the latter water. To generate steam at 130 °C, a heat pump is integrated. The heat pump uses the generated heat of the CPC collector field as a heat source. The heat pump is modeled as a compression heat pump and

can only operate at nominal power. The electricity is either completely supplied by the grid or by a combination of the grid and a photovoltaic field (CPC_HP_TES_PV).
The third system has a photovoltaic (PV) field as an energy generating technology. The generated electricity is transformed into heat with an electric heater. The electric heater evaporates the water from the consumer side. A battery energy storage system (BESS) is integrated to store electricity generated by the PV field.
The fourth system uses a PV field as well. Again, an electric heater is used to transform the electric energy into heat energy. However, in this system, the electric heater heats pressurized water up to 210 °C. Thereby, a PTES can be integrated to store heat energy. Just like in the first system, the pressurized water transfers the heat in a heat exchanger to evaporate the water on the consumer side.

In Würzburg, the lowest achievable LCOH with the PTC_PTES system is 0.0519 €/kWh at a capacity factor of 12.55 %. Although the PTC_PTES system achieves the overall lowest LCOH, the PV_EH_PTES system achieves lower LCOH at higher capacity factors. The CPC_HP_TES system has comparatively high LCOH, due to high investment cost. The LCOH decreases with the integration of a PV field (CPC_HP_TES_PV). However, the LOCH does not decrease significantly enough to make the system competitive with the PV_EH_PTES system. The PV_EH_BESS system cannot compete with the PV_EH_PTES system due to the higher storage costs. With the integration of a storage, the LCOH of the PTC_PTES, PV_EH_PTES and PV_EH_BESS system increases. Only the LCOH of the CPC_HP_TES decreases with the integration of a TES.

In Almeria, the achieved LCOH is lower, and capacity factors are higher for all systems. In contrast to Würzburg, the PTC_PTES system achieves lower LCOH than the PV_EH_PTES system, up to a capacity factor of up to 90 %. The lowest achievable LCOH of the PV_EH_PTES system in Almeria is 0.0272 €/kWh at a capacity factor of 18.07 %. In Almeria, the CPC_HP_TES and PV_EH_BESS cannot achieve the lowest LCOH for all capacity factors as well.

The cost sensitivity analysis showed that the most sensible investment costs are:

- PTC_PTES: PTC investment,
- CPC_HP_TES: CPC collector investment,
- PV_EH_BESS: BESS investment and

- PV_EH_PTES: PV field investment.

If these costs are varied by 20 %, the PTC_PTES and PV_EH_PTES system can both be the most economically beneficial system in Almeria or Würzburg.

Finally, the systems are compared to an installed gas boiler economically. The comparison is made for both locations and with the gas prices of the second half of 2022 (11 ct/kWh in Würzburg/ 13 ct/kWH in Almeria) and the beginning of 2023 (both 5 ct/kWh).
For both scenarios, all systems, except the CPC_HP_TES system in Würzburg with a gas price of 5ct/kWh, can save energy costs. As the systems reach higher LOCH and capacity factors in Almeria, they achieve higher saved energy costs as well. In Würzburg, the PV_EH_PTES system achieves the highest economic benefit and the PTC_PTES system in Almeria.
However, despite the short time between both scenarios, due to the volatile gas price, the annual saved energy costs differ by up to 90 % between the calculations for the scenario at the beginning of this thesis and the end.

The results of this study cannot be transferred to all other applications. The boundary conditions and assumptions strongly impact the results of the calculations. Should these results be used for other applications, this circumstance must be considered.

For subsequent studies, should the prices change, these calculations could be updated and carried out again. To cover more industries, the behavior with different load curves can be analyzed. Another improvement in follow-up studies can be the improvement of the heat pump system. If sufficient data for the startup-, shutdown- and part load behavior are available, the model can be updated and improved.

In conclusion, the presented systems in the calculated scenarios can compete with fossil-fueled technologies up to certain capacity factors. Although they perform better and are already used in Spain, these calculations show that they can be economically beneficial in Germany as well and, depending on the future gas situation, become more relevant in the future.

A Appendix

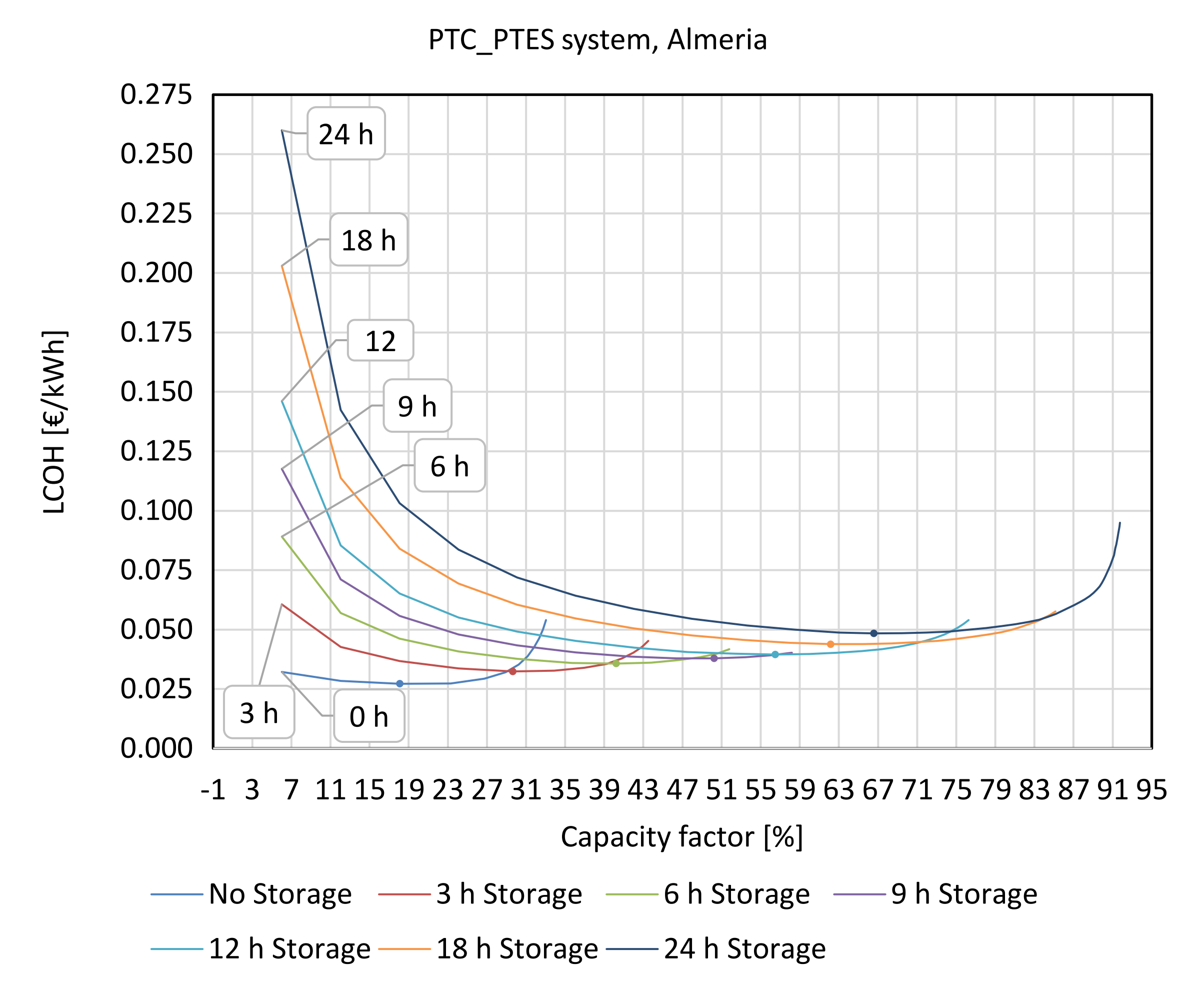

Figure A-0-1: LCOH over capacity factor, PTC_PTES, Almeria

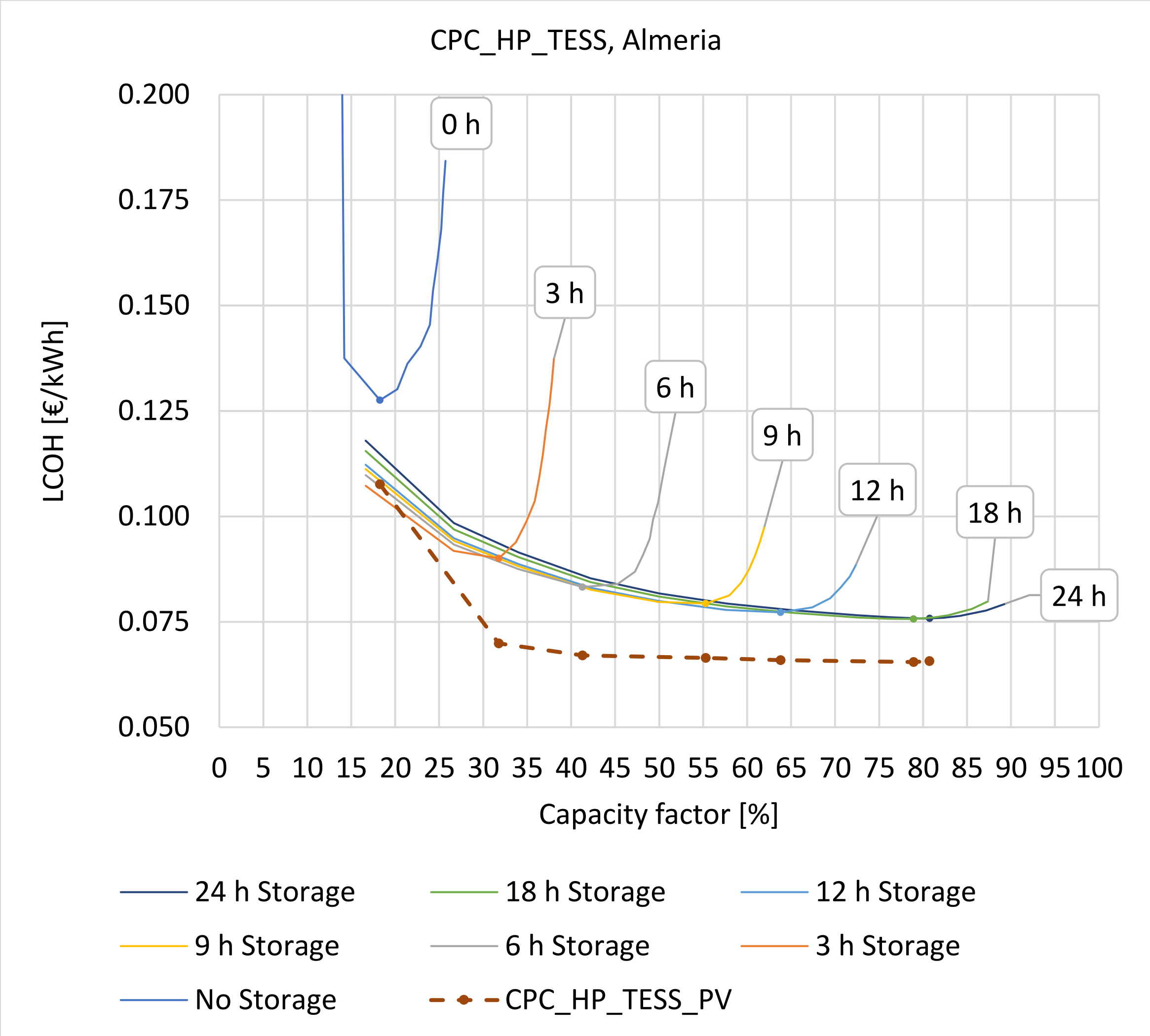

Figure A-0-2: LCOH over capacity factor, CPC_HP_TESS, Almeria

Table A-0-1 PV results, CPC_HP_TES_PV, Almeria

TES Capacity [h]	Heat Pump electricity demand [MWh]	PV BESS Capacity [h]	Number PV systems	LCOE [€/kWh]	Capacity factor [%]
0	2122	0	15	0.0595	93.13
3	3549	0	17	0.0451	83.16
6	4464	0	17	0.0438	68.19
9	5840	0	17	0.0419	54.50
12	6715	0	17	0.0416	47.75
18	8283	0	20	0.0431	43.98
24	8470	0	20	0.0426	43.31

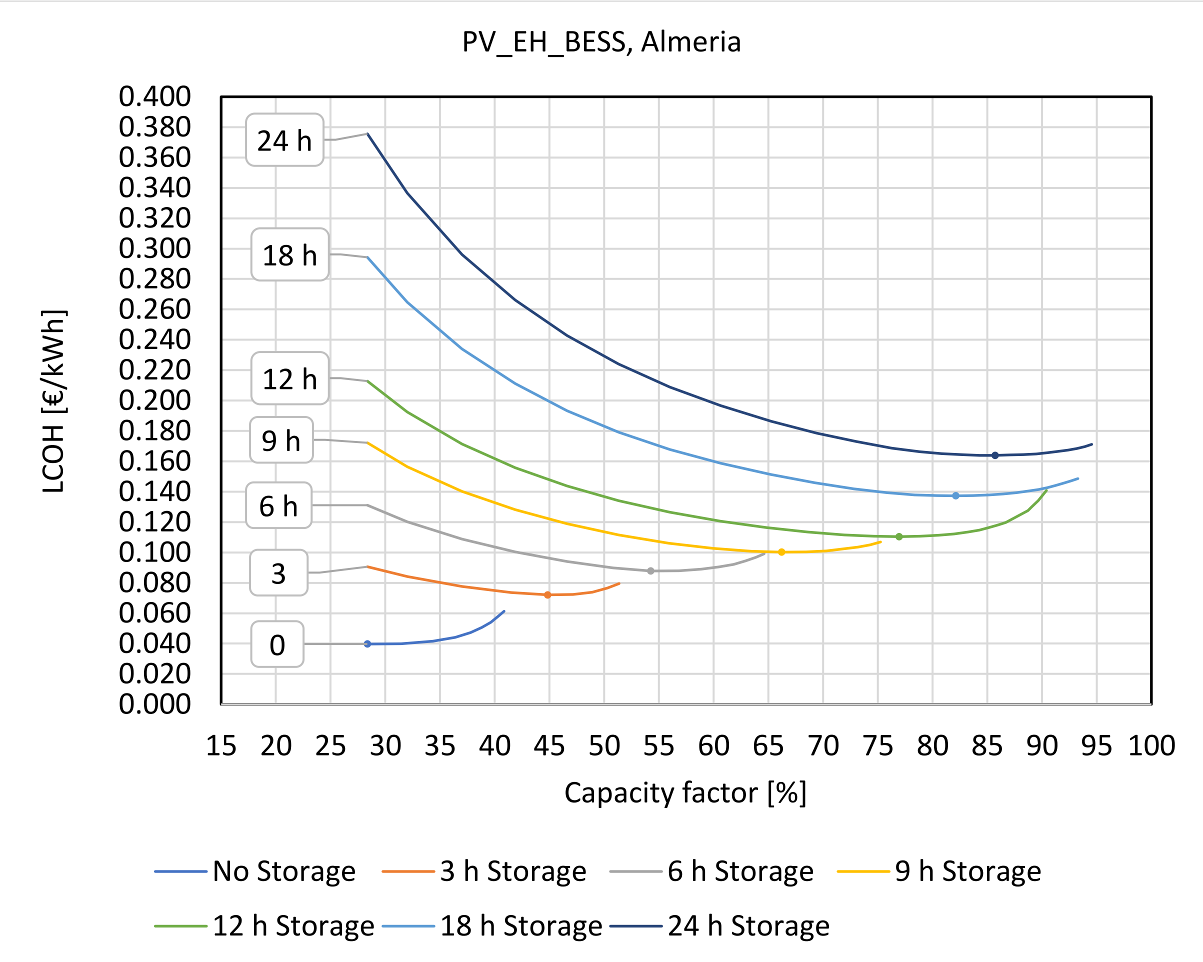

Figure A-0-3: LCOH over capacity factor, PV_EH_BESS, Almeria

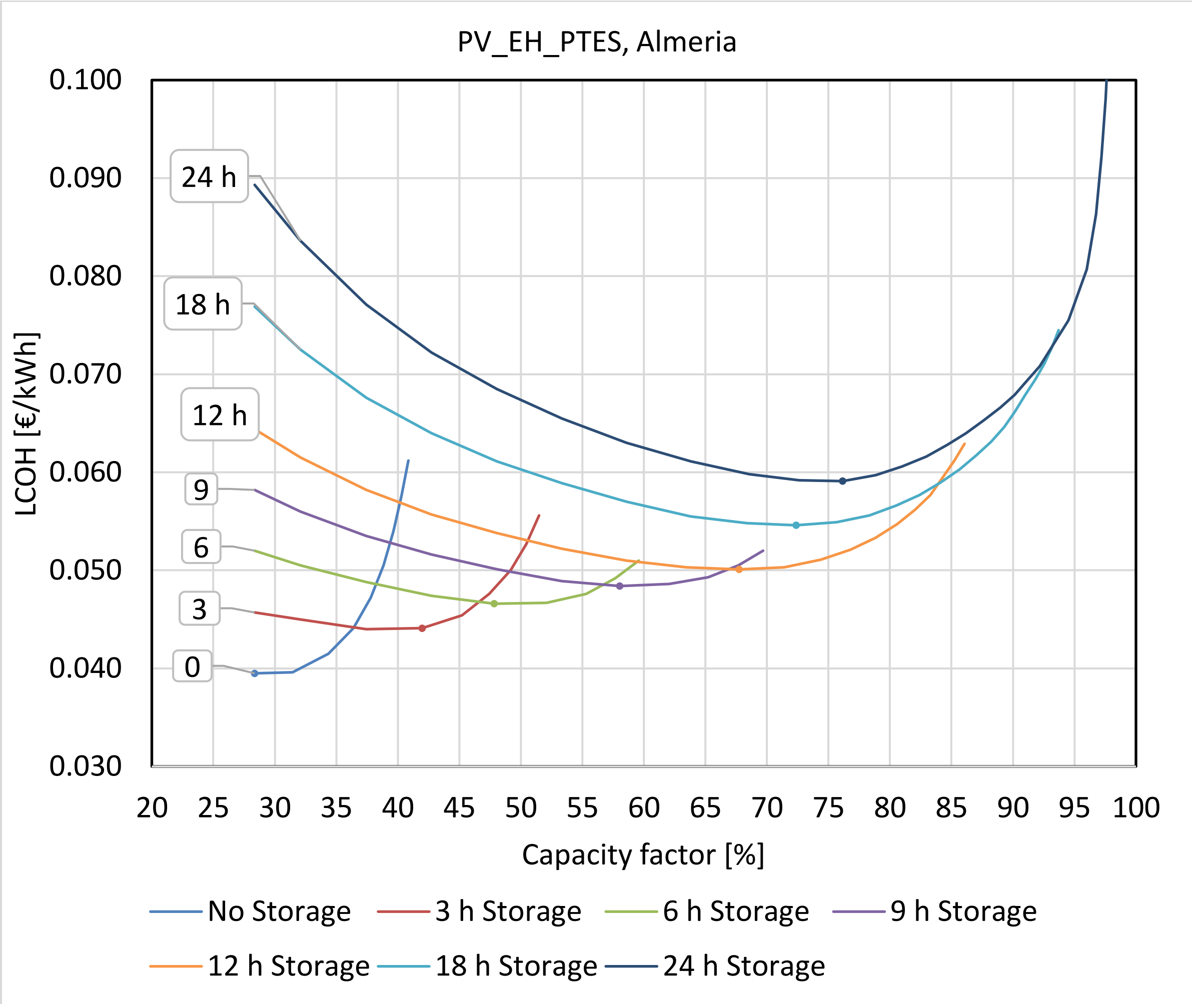

Figure A-0-4: LCOH over capacity factor, PV_EH_PTSS, Almeria

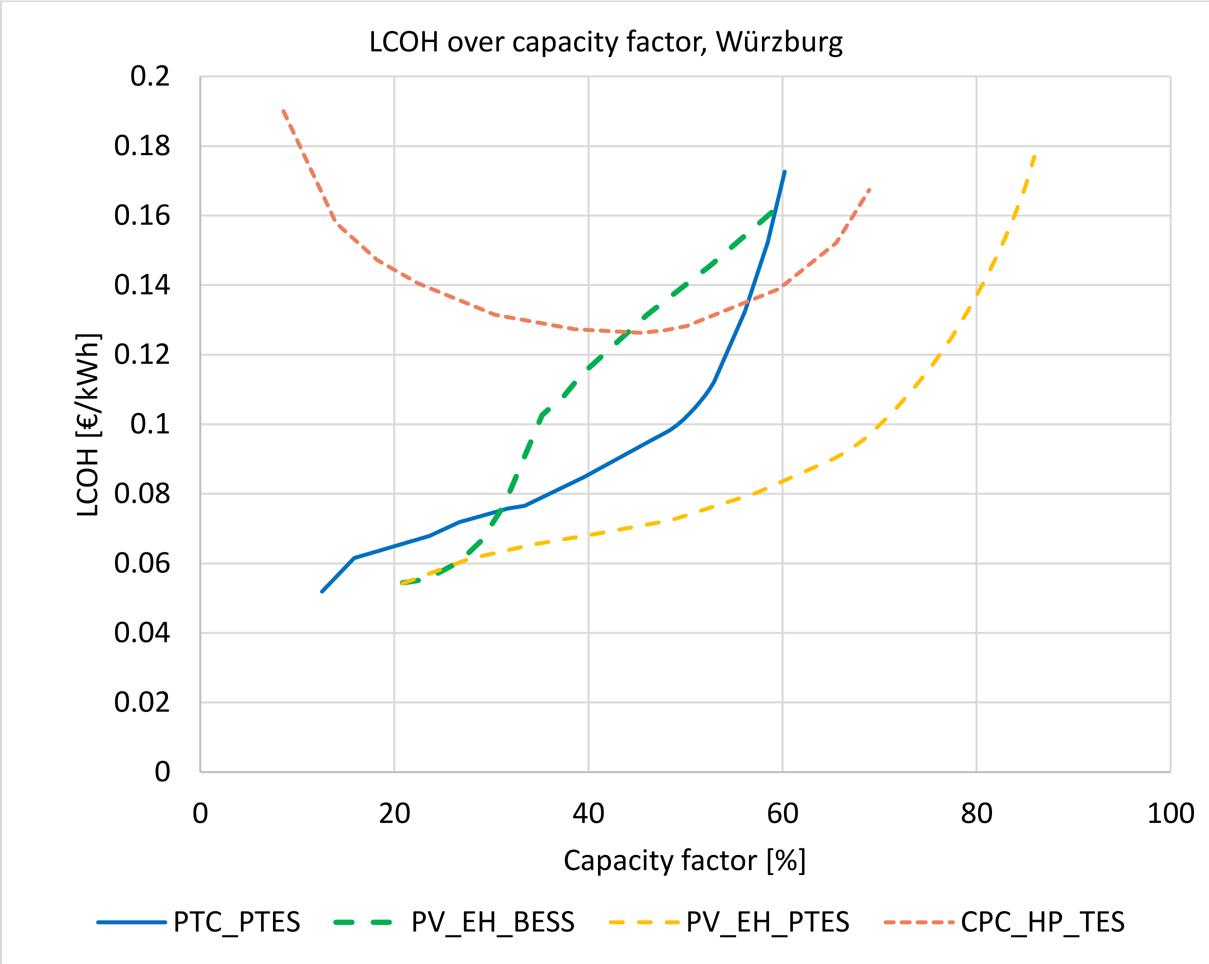

Figure A-0-5: Minimal LCOH over capacity factor in Würzburg.

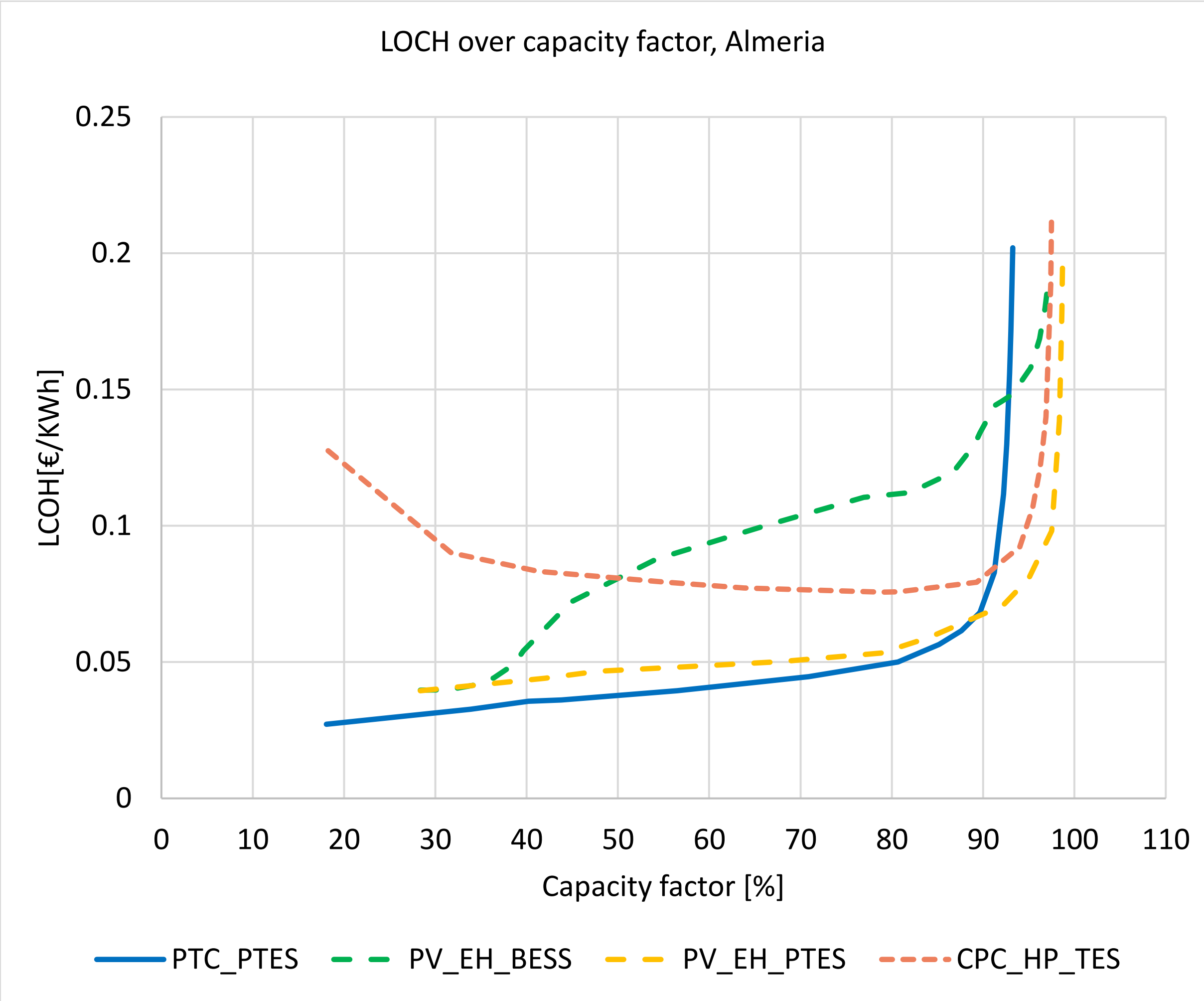

Figure A-0-6: Minimal LCOH over capacity factor in Almeria.

7 Bibliography

Appunn, K. (2022): Renewables supplied 46% of net public power in Germany in 2021. Edited by CLEAN ENERGY WIRE. Available online at https://www.cleanenergywire.org/news/renewables-supplied-46-net-public-power-germany-2021, checked on 3/13/2023.

Arpagaus, C. (2017): Hochtemperatur Wärmepumpen. Literaturstudie zum Stand der Technik, der Forschung, des Anwendungspotenzials und der Kältemittel. NTB Interstaatliche Hochschule für Technik Buchs.

Arpagaus, C.; Fréé, B.; Uhlmann, M.; Schiffmann, Jü.; Bertsch, SS. (2018): High temperature heat pumps: Market overview, state of the art, research status, refrigerants, and application potentials. In *Energy (2018)*. DOI: 10.1016/j.energy.2018.03.166.

Azteq (2023): Gas prices and heat generation costs of a boiler. Personal conversation, 2023.

Bielsa, D. (2022): Sensible heat storage. Available online at https://www.norvento.com/en/blog/sensible-heat-storage/, checked on 3/14/2023.

Blümm, F. (2022): Strompreisentwicklung Deutschland 2022: Warum steigen die Stromkosten? Available online at https://www.tech-for-future.de/strompreisentwicklung/#Industrie_Gewerbe_Strompreise_fuer_energieintensive_Unternehmen, checked on 2/6/2023.

Bundesnetzagentur (2022): Gaspreise. Available online at https://www.bundesnetzagentur.de/DE/Gasversorgung/aktuelle_gasversorgung/_svg/Gaspreise/Gaspreise.html, checked on 2/6/2023.

Celsius (2020): Thermal Energy Storage. Available online at https://celsiuscity.eu/thermal-energy-storage/, checked on 2/6/2023.

Danish Energy Agency (2016): Technology Data. Generation of Electricity and District heating. Edited by Danish Energy Agency and Energinet. Energistyrelsen.

Dersch, J.; Schonmaker, L. (2021): Integration of PV with CSP and Thermal Storages in Solar Power Plants. Investigations about Synergies by close Coupling. Final report of the research project: IntegSolar. Cologne, Germany.

Dersch, J.; Schonmaker, L.; Inigo Labairu, J.; Mhaske, S.; Pfundmaier, L.; Schelcht, M.; Zimmermann, F. (2021): Integration of PV with CSP and Thermal Storages in Solar Power Plants. Investigations about Synergies by close Coupling. Final report of the research project “IntegSolar” No. 03EE5011. Cologne, Germany.

Djunisic, S. (2022): Engie starts building 30-MW CSP plant for Heineken Spain. Available online at https://renewablesnow.com/news/engie-starts-building-30-mw-csp-plant-for-heineken-spain-800014/, checked on 3/9/2022.

DLR (2022a): greenius. Version 2022. Available online at http://freegreenius.dlr.de, checked on 2/23/2023.

DLR (2022b): Internal information, Köln.

Dohmann, Joachim (2016): Thermodynamik der Kälteanlagen und Wärmepumpen. Grundlagen und Anwendungen der Kältetechnik. Berlin, Heidelberg: Springer Vieweg (Lehrbuch). Available online at http://www.springer.com/.

Energy storage (2023): Sensible Heat Storage for Low Temperatures (up to 150 °C). Available online at https://iea-es.org/fact-sheet_sensible-water/, checked on 3/4/2023.

Eurostat (2021): Agricultural land prices by region. Available online at https://ec.europa.eu/eurostat/databrowser/view/apri_lprc/default/table?lang=en, checked on 2/6/2023.

French, T. (2020): What is Microsoft Excel and What Does It Do? Available online at https://www.lifewire.com/what-is-microsoft-excel-3573533, checked on 3/9/2023.

GlobalPetrolPrices.com (2022): Spain fuel prices, electricity prices, natural gas prices. Available online at https://www.globalpetrolprices.com/Spain/, checked on 2/6/2023.

Hirsch, Tobias; Fabian Feldhoff, Jan; Schenk, Heiko (2012): Start-Up Modeling for Annual CSP Yield Calculations. In *Journal of Solar Energy Engineering* 134 (3), Article 031004. DOI: 10.1115/1.4006268.

Iñigo-Labairu, Javier; Dersch, Jürgen; Schomaker, Luca (2022): Integration of CSP and PV Power Plants: Investigations about Synergies by Close Coupling. In *Energies* 15 (19), p. 7103. DOI: 10.3390/en15197103.

IRENA (2022): Renewable Power Generation Costs in 2021. Edited by International Renewable Energy Agency. Abu Dhabi.

Jesper, Mateo; Schlosser, Florian; Pag, Felix; Walmsley, Timothy Gordon; Schmitt, Bastian; Vajen, Klaus (2021): Large-scale heat pumps: Uptake and performance modelling of market-available devices. In *Renewable and Sustainable Energy Reviews* 137, p. 110646. DOI: 10.1016/j.rser.2020.110646.

Kalogirou, Soteris (2003): The potential of solar industrial process heat applications. In *Applied Energy* 76 (4), pp. 337–361. DOI: 10.1016/S0306-2619(02)00176-9.

Kraemer, S. (2022): Paper Shows How Dispatchable CSP Can Solve the EU Gas Crisis. Edited by SolarPACES. Available online at https://www.solarpaces.org/paper-shows-how-dispatchable-csp-can-solve-eu-gas-crisis/, checked on 3/13/2023.

Krüger, D. (2021): Concentrating collector for Central Europe. Edited by 24th Cologne Solar Colloquium. DLR Institute of Solar Research.

Krüger, D.; Epp, B.; Hirsch, T., Stengler, J. (2021a): Status in Solar Heat from Concentrating Solar Systems. German Aerospace Center, Institute of Solar Research. Cologne, Germany.

Krüger, D.; Fischer; S.; Nitz, P.; Inigo Labairu, J. (Eds.) (2021b): Chancen für den Einsatz konzentrierender Kollektoren in Mitteleuropa. 31. Symposium Solarthermie und innovative Wärmesysteme 2021. Pforzheim: Conexio.

List solar (2022): Heineken begins building and construction of its second CSP plant in Spain. Available online at https://list.solar/news/heineken-begins/, checked on 3/9/2023.

MasterClass (2021): How to Reduce Carbon Emissions: 6 Ways to Reduce Emissions. Available online at https://www.masterclass.com/articles/how-to-reduce-carbon-emissions, checked on 3/9/2023.

Mathiesen, B. (2015): Heat Roadmap Europe 2015 Final Heating & Cooling Demand in Germany.

Müller, C. (2022): Gaspreisdeckel: Ist die „iberische Lösung“ ein Modell für Deutschland? Available online at https://www.wiwo.de/unternehmen/energie/spanien-alsvorreiter-gaspreisdeckel-ist-die-iberische-loesung-ein-modell-fuer-deutschland/28709538.html, checked on 3/7/2023.

NREL (2022): 2022 Annual Technology Baseline. Edited by National Renewable Energy Laboratory (NREL). Available online at https://data.openei.org/submissions/5716, checked on 3/21/2023.

Oehler, J.; Phong Tran, A.; Stathopoulos, P. (2022): Simulation of a safe start-up maneuver for a brayton heat pump. Edited by German Aerospace Center (DLR), Institute of Low-Carbon Industrial Processes, Cottbus, Brandenburg, Germany.

Pavlovic, Tomislav (2020): The Sun and Photovoltaic Technologies. Cham: Springer International Publishing AG (Green Energy and Technology Ser). Available online at https://ebookcentral.proquest.com/lib/kxp/detail.action?docID=5968960.

Proplanta (2019): Landwirtschaftliche Grundstückspreise. Available online at Ackerlandpreise - Bodenpreise (Euro/ha) 2019 | Übersichtskarte | agrar-aktuell.de, checked on 1/25/2023.

Quaschning, Volker (2015): Regenerative Energiesysteme. Technologie - Berechnung - Simulation. 9., aktualisierte und erweiterte Auflage. München: Hanser. Available online at http://files.hanser.de/hanser/docs/20141216_214121682321-93_978-3-446-44267-2_Leseprobe.pdf.

Saini, Puneet; Ghasemi, Mohammad; Arpagaus, Cordin; Bless, Frédéric; Bertsch, Stefan; Zhang, Xingxing (2023): Techno-economic comparative analysis of solar thermal collectors and high-temperature heat pumps for industrial steam generation. In *Energy Conversion and Management* 277, p. 116623. DOI: 10.1016/j.enconman.2022.116623.

Schmitt, B.; Pag, F.; Wimmer, L.; Best, I.; Ritter, D.; Vajen, K. (2015): Leitfaden zur Nutzung solarer Prozesswärme in der Ernährungsindustrie. Aufbereitung branchenspezifischer Informationen zu Prozess- und Anlagentechnik, Integrationsmöglichkeiten und Nutzungspotentialen solarer Prozesswärme. Edited by Uni-Kassel.

Solarlite CSP Technology GmbH (2023): Cost assumptions for solar plants. Personal conversation, 2023.

STEAG Energy Services (Ed.) (2022): EBSILON®Professional. Das Planungswerkzeug für den Kraftwerksprozess. Available online at https://systemtechnologies.iqony.energy/uploads/pics/Broschuere_EBSILON_Das_Planungswerkzeug_fuer_den_Kraftwerksprozess_de_03.pdf, checked on 2/23/2023.

Stieglitz, Robert; Heinzel, Volker (2012): Thermische Solarenergie. Grundlagen, Technologie, Anwendungen. Berlin, Heidelberg: Springer Vieweg (Lehrbuch).

Washim Akram, M.; Hasanuzzaman, Md. (2022): Fundamentals of thermal energy and solar system integration. DOI: 10.1016/B978-0-12-823959-9.00003-9.

Wildi-Tremblay, Philippe; Gosselin, Louis (2007): Minimizing shell-and-tube heat exchanger cost with genetic algorithms and considering maintenance. In *Int. J. Energy Res.* 31 (9), pp. 867–885. DOI: 10.1002/er.1272.

Wolf, S. (2017): Integration von Wärmepumpen in industrielle Produktionssysteme. Potenziale und Instrumente zur Potenzialerschließung. Institut für Energiewirtschaft und Rationelle Energieanwendung, Universität Stuttgart.